Winter 12-15-2017

Comparison of the Bi-Directional Performance of Micro-Channel Sieve and Thin-Film TIME Peripheral Nerve Interfaces

Robert Coker
Washington University in St. Louis

WASHINGTON UNIVERSITY IN ST. LOUIS

Division of Engineering & Applied Science
Department of Biomedical Engineering

Dissertation Examination Committee:
Daniel Moran, Chair
Dennis Barbour
Shantanu Chakrabartty
Wilson (Zack) Ray
Matthew Wood

Comparison of the Bi-Directional Performance of Micro-Channel Sieve and Thin-Film TIME Peripheral Nerve Interfaces

by
Robert Coker

A dissertation presented to
The Graduate School
of Washington University in
partial fulfillment of the
requirements for the degree
of Doctor of Philosophy

December 2017
St. Louis, Missouri

Table of Contents

List of Figures

List of Tables

Acknowledgments

A project like this is never performed in a vacuum. I would like to thank a number of individuals and institutions who made this work possible.

The bulk of this work was performed under a National Institute of Health (NIH) T32 training grant with additional support to complete the project from the Defense Advanced Research Projects Agency (DARPA). Their funding made this work possible. My committee (Dennis Barbour, Wilson (Zack) Ray, Matthew Wood, and Shantanu Chakrabartty) was helpful in reviewing and interpreting the significance of results as well as pointing me to useful reference papers. Wilson (Zack) Ray provided training in basic animal surgical techniques and the opportunity to implant micro-channel devices to test biological feasibility and neural regeneration characteristics.

Earlier in the project, I explored creating simplified micro-channel devices with only a few metalized channels. Nathan Reed of the Washington University Nano Research Facility was tremendously helpful in working out the details of the fabrication process. Erik Henriksen provided expertise and usage of low temperature micro-soldering on those early devices.

Ashley Coker added her graphic design skills in many of the figures of this dissertation. Without her help, the information being conveyed would neither have been as clear nor as attractive. Additionally, she along with the rest of my family put up with her dad being very busy for a number of years while chasing his dream of obtaining a PhD.

Erik Zellmer contributed to this research in a number of ways. He trained me in the use of Comsol and NEURON and provided NEURON axon models, two of the three main tools used in the computational modeling. He continued to provide his technical expertise in the use of these

tools a few, critical times throughout the project. He edited my draft papers (chapters 3 and 4), making them far clearer and precise than my drafts. His enthusiasm for this project was evident and he was an encouragement throughout it.

Finally, special thanks to Daniel Moran for encouraging my pursuit of a PhD, advice along the way of how to navigate an academic institution, providing and letting me be part of a lab environment which enabled and supported my work without being overbearing, for brainstorming sessions where we came up with this project, for insight and perspective along the way when I was too close to be able to see, and beyond all that, for being a friend. I couldn't have had a better mentor.

Robert Coker

Washington University in St. Louis

December 2017

Dedicated to

Charles Austin Coker

and

Margaret Olivia Brock Huntsman.

ABSTRACT OF THE DISSERTATION

Comparison of the Bi-Directional Performance of Micro-Channel Sieve

and Thin-Film TIME Peripheral Nerve Interfaces

by

Robert Coker

Doctor of Philosophy in Engineering & Applied Science

Department of Biomedical Engineering

Washington University in St. Louis, 2017

Professor Daniel Moran, Chair

Sophisticated motorized prosthetic limbs contain multiple degrees of freedom of motion as well as embedded pressure and angle transducers to provide sensory feedback in amputees. Although several central neural recording and stimulation modalities exist for both controlling these motions and providing sensory feedback from a prosthetic limb, directly interfacing the peripheral nerves which originally innervated the limb has many advantages. A difficulty with this bi-directional approach is that electrically stimulating axons to provide haptic feedback creates stimulation artifacts at neighboring recording sites within the nerve that are several orders of magnitude larger than the electroneurogram used for control. In this dissertation, a novel micro-channel sieve electrode is designed, optimized and tested that can provide true bi-directional and concurrent electrical stimulation to sensory axons while simultaneously recording high-fidelity electroneurograms from motor axons in the same peripheral nerve. This research, through computational modeling, compares the concurrent bi-directional performance of both the novel micro-channel sieve electrode designed in this dissertation and the gold standard

intrafascicular electrode (tfTIME) used in current clinical research studies in human amputees. The novel micro-channel sieve electrode was found to significantly outperform the tfTIME electrode by increasing recording levels and decreasing stimulation artifact yielding a signal to artifact ratio greater than 50 dB compared to -56.4 dB for the tfTIME. The novel micro-channel sieve electrode developed in this dissertation could provide the first concurrentl, bi-directional peripheral nerve interface for clinical applications.

Chapter 1: Introduction

1.1 Scope

There are roughly 1.6 million Americans who have had a limb amputated and nearly 200,000 new cases every year. Around half of these amputations are due to trauma and are good candidates for a prosthetic limb because they are otherwise generally healthy (Ziegler-Graham et al. 2008). In addition to the electromechanical difficulties of matching the capabilities of a human limb, there is the question of how to control and receive feedback from it. Further, it is important to do both of these simultaneously so that the patient can receive proprioceptive and tactile feedback from the limb while moving it.

The research herein focuses on means to interface the peripheral nervous system in a concurrent, bi-directional way as a critical component of a motorized prosthetic limb system. Other modalities for control and feedback (e.g, brain computer interfaces) are thoroughly explicated in Chapters 3 and 4. Further, there are non-trivial problems (also explicated in Chapters 3 and 4) with stimulating peripheral nerve fibers to generate sensation while concurrently trying to record from adjacent fibers in order to determine the patient's intent for the device to move. In brief, stimulating axons in the vicinity of a given stimulation electrode on the device creates a stimulation artifact at neighboring recording electrodes that disrupt the ability to record or measure the patient's intended control of the device. This is the central problem addressed by this research.

To more tightly specify the scope, this research does not cover the design of prosthetic limbs nor does it address, except in the most cursory fashion, algorithms for decoding neural intention or how to stimulate neural activity to generate a desired percept. Instead, it is limited to comparing, by computational modeling techniques, the bi-directional performance of two peripheral neural interface (PNI) device classes: the thin-film Transverse Intrafascicular Multichannel Electrode (tfTIME) and the Micro-channel Sieve Electrode. The tfTIME is the current dominant player, but the Micro-channel Sieve Electrode has certain properties that give it a compelling advantage for use in this application. Additionally, this research seeks to optimize the design of Micro-channel Sieve Electrodes by considering design parameters for unipolar, bipolar and tripolar stimulation paradigms. Finally, a critical aspect of the computational modeling was verified by testing the electrical performance of larger scale devices.

1.2 Specific Aims

Aim 1: Design and build computational models of peripheral nerve/electrode interfaces to determine the stimulation artifact. Computational models are constructed for both tfTIME and micro-channel device types. The stimulation current required to activate surrounding neurons is determined as is the corresponding stimulation artifact.

Aim 2: Design and build computational models of peripheral nerve/electrode interfaces to determine expected recording level across motor neuron recruitment. Using a stochastic model of motor unit recruitment, the multi-axon electroneurogram (ENG) is predicted for both tfTIME and micro-channel device types.

Aim 3: Design and optimize the micro-channel electrode for a bi-directional interface. Using the models from Aims 1 and 2, the bi-directional performance of the micro-channel electrode design is optimized by varying the dimensions (length and channel area) of micro-channels, stimulation paradigm (monopolar, bipolar and tripolar), and contact location for multi-polar stimulation, in order to maximize the ratio of ENG voltage levels to stimulation artifact.

Aim 4: Validate micro-channel electrostatic model. Construct a large-scale model of adjacent micro-channels to confirm the validity of the electrostatic modeling intrinsic to the prior aims.

1.3 Organization

The organization of this dissertation is:

- Chapter 1 – Introduces the research and Specific Aims.
- Chapter 2 – Provides background material that is not elsewhere in the dissertation.
- Chapter 3 – Incorporates the journal article, *Micro-Channel Sieve electrode for Bi-Directional peripheral nerve interface. Part A: Recording*, with formatting changes to meet dissertation guidelines. Aim 2 is addressed by this chapter.
- Chapter 4 – Incorporates the journal article, *Micro-Channel Sieve electrode for Bi-Directional peripheral nerve interface. Part B: Stimulation and Bi-Directional Performance*, with formatting changes to meet dissertation guidelines. Aims 1 and 3 are addressed by this chapter.
- Chapter 5 – Demonstrates the validity of the electrostatic model of micro-channel devices through laboratory testing. Aim 4 is addressed by this chapter
- Chapter 6 – Outlines future direction for this work.

Dr. Erik Zellmer is a co-author of chapters 3 and 4. Dr. Zellmer provided initial training and technical assistance in the mechanics of using the COMSOL and NEURON software packages for the computational models, provided the NEURON axon model library files used herein, modified (re-meshed) the multi-polar models of Chapter 4 to have better numeric properties, edited drafts, and provided a few of the comparison figures of the papers.

1.4 References

Ziegler-Graham, Kathryn, Ellen J. MacKenzie, Patti L. Ephraim, Thomas G. Travison, and Ron Brookmeyer. 2008. "Estimating the Prevalence of Limb Loss in the United States: 2005 to 2050." *Archives of Physical Medicine and Rehabilitation* 89 (3):422–29. https://doi.org/10.1016/j.apmr.2007.11.005.

Chapter 2 : Background

This chapter presents background material useful for understanding the rest of the dissertation. Two primary areas are dwelt upon. The first is the characteristics of a motor neuron pool – the collection of all alpha motor neurons that innervate a given muscle. This is touched upon in Chapter 3, but is addressed more fully below. The second shows a derivation of the equation used in the Finite Element Modeling to predict the voltage and currents throughout the computational models discussed in the remainder of the dissertation. Additional background material is provided in the Introduction and Methods sections of Chapters 3 and 4 and is not repeated here.

2.1 Motor Neuron Pools

A single motor neuron (MN) innervates a number of muscle fibers within a single muscle. Each muscle fiber is only innervated by one MN. The MN with its associated muscle fibers is called a motor unit (Heckman and Enoka 2012). The collection of all MNs that innervate a given muscle are the motor neuron pool for that muscle. The general principle that muscle force is increased by a combination of increasing the fraction of MNs in the pool that are active (recruitment) and increasing the firing rate of the already active MNs was already known when Burke and Henneman wrote classic papers on the topic in the 1950s and 60s (Henneman 1957; Henneman, Somjen, and Carpenter 1965b, 1965a).

In 1957, Henneman used a preparation in which he electrically stimulated cat dorsal roots to elicit stretch reflex induced motor neuron firings. While taking recordings from a small filament of the associated ventral root extracellularly, he noticed that the first action potentials were small.

As he increased the stimulation, multiple axons began to fire with successively larger action potentials (Henneman 1957). He followed up this work by stretching the muscle to trigger the stretch reflex instead of using electrical stimulation (Henneman, Somjen, and Carpenter 1965b) and using a variety of other reflexes to confirm that the results he saw were not particular to the stretch reflex (Henneman, Somjen, and Carpenter 1965a). The association between smaller axons having smaller action potentials, smaller somas and slower conduction velocities was an assumption of Henneman, but was verified by Clamann (Clamann and Henneman 1976). The implication of these experiments is that smaller neurons with smaller axons have a lower threshold to begin firing (referred to as the activation threshold) with additional neurons being recruited in size order. This is called "the size principle" and is fundamentally intact today as the order by which MNs are recruited.

Using intracellular techniques in the gastrocnemius motor neuron pool of decerebrate cats, Burke measured a variety of properties of the neurons including the 'tonic' threshold or threshold to fire steadily. He also investigated the properties of the muscle fibers associated with the MN he was stimulating and divided them into 3 groups (S, F*, and F) based on their twitch times (S for slow vs F for fast) and tension levels (F* for lower tension, F for higher), noting that all S fibers could be made to fire tonically, but not all F* and even fewer F ones could. Further, he showed interrelation of factors like excitatory post-synaptic potentials (EPSP) as a function of input resistance and how that related to neuron size and activation threshold (Burke 1968). Following Burke's pattern of differentiating between muscle fiber types, Kernell looked at activation threshold in MNs which drove S, FR (Fast, Fatigue Resistant) and FF (Fast, Fatigable) muscle units. He found that the size principle did work within S motor units, but that FR motor units had roughly half the activation threshold of similarly sized FF units (Kernell and Monster

1981). Zajac's research confirmed that the size principle works within S motor units, but not F. However, his results also showed that the weakest motor unit fired first and the most fatigable fired last (Zajac and Faden 1985). Additional intracellular work by Gustafsson and Pinter showed that input conductance of the cell, its membrane time constant and after-hyperpolarization (AHP) duration were better predictors of rheobase (or tonic activation threshold) (Gustafsson and Pinter 1984). Differentiating between fiber types, using intracellular techniques, or both, has shown that the size principle is basically true, but reality is somewhat more complicated.

An additional complexity is the type of movement being performed. For example, it is sometimes argued that ballistic movements - those where a limb is moved very fast for a short duration - utilize selective activation. In this case, the central nervous system is asserted to selectively activate only those muscles fibers that contracted quickly to create a quick movement. Bawa, however, recently reviewed a number of studies showing that this is generally not the case. He further argues that in an intact biological system, there will be noise on the inputs to the neurons that could result in the size order not being perfectly followed, particularly in the case of aging, fatigue or pain (Bawa, Jones, and Stein 2014). Another potential source of confusion regarding the size principle not being followed is that not all the muscle units in a given muscle are activated by a specific motion. Riek found that different portions of the extensor digitorum communis (EDC) were activated depending on whether the middle or ring finger was extended. Thus, there were sub-pools within the overall EDC motor neuron pool. For a given movement, the neurons within that sub-pool were activated in size order, even though some small MNs within the EDC motor neuron pool would not have been activated since they were not part of that "task group" (Riek and Bawa 1992).

Milner-Brown studied the firing rate aspect in more detail in the human first dorsal interosseus (FDI) muscle finding an average initial firing rate of 8.4 spikes/sec with an increase of 1.4 spikes/sec per every additional 100g of force, noticing also that the firing rate reached a plateau when doing a slow force ramping profile, but that fast ramps elicited a burst of activity at movement start (Milner-Brown, Stein, and Yemm 1973). More recently, Duchateau, in looking at ballistic contractions similar to a very fast ramp, found a much greater initial firing rate (higher than 100 spikes/sec) than in ramped contractions where the range was 20 - 50 spikes/sec (Duchateau and Baudry 2014). In addition, Enoka and Fuglevand point out that ballistic movements can have double firing of axons (or doublets) in the early phase of force generation (Enoka and Fuglevand 2001). The complexity of this process was brought out in a recent review by Heckman and Enoka, showing that the firing patterns are different depending on whether the contraction is concentric (a shortening contraction), isometric, or eccentric (a lengthening contraction) and further whether the force trajectory is very fast (ballistic), steady or ramped (Heckman and Enoka 2012).

Regardless of the complexities, the bulk of muscle force does come from increasing the firing rate. Only 10 - 15% of total muscle force would be achieved if all MNs fired at their minimum discharge rate. Further, a motor neuron pool has many low threshold MNs driving small muscle units, while a very few high threshold MNs drive big ones. Thus, as excitatory drive increases, the amount of force added due to recruitment is nearly constant because the product of the decreasing number of new active neurons is compensated for by greater force per neuron. Yet, at every stage, the bulk of the increased force is due to increased firing rate of already active MNs (Harrison 1983).

Computational modeling has provided insight into operation of the motor neuron pool. In a seminal work from 1993, Fuglevand developed a model of motor neuron recruitment, associated muscle force generation and electromyogram (EMG) output as a means of investigating the details of the recruitment and firing rate processes. Since the correlation of force and EMG output are measurable, various strategies for recruitment could be tested across a broader range of intended force levels (also called the excitation level) than could be in an animal preparation. Additionally, all neurons in a pool could be modeled where only a few can be measured in a single animal. One result that came from this paper is that new neurons continue to be recruited until the excitatory drive is high - roughly 70% of maximum voluntary contraction (MVC) (Fuglevand, Winter, and Patla 1993). In a subsequent review, Fuglevand notes that the force level at which all MNs have begun to fire varies depending on muscle type and can vary from 50% to 85% (Enoka and Fuglevand 2001). Fuglevand's model has been used frequently by others to answer questions as varied as whether it is truly important to have large muscle units activated last or if having a wide range of innervation numbers is adequate (Dideriksen and Farina 2014), whether synchronization in MNs firing causes greater force output (Yao, Fuglevand, and Enoka 2000), proper technique for measuring muscle twitch characteristics (Taylor, Steege, and Enoka 2002), and how to achieve steadiness of muscle force output (Taylor, Christou, and Enoka 2003; Moritz et al. 2005).

2.2 Finite Element Modeling of Volume Conduction

Finite Element Modeling (FEM) is a means to numerically solve partial differential equations (PDEs) with boundary conditions. The derivation of the PDE of interest begins with Maxwell's 4th Equation:

$$\nabla \times H = J + \frac{\partial D}{\partial t}$$

where H is the magnetic field intensity, J is the current density and D is the electric flux density. Biological tissue, generally, is not polarizable, i.e. is not a storage element. Further, the cases under consideration involve the electric field, and thus electric flux, being relatively constant (quasi-stationary). For our case, then, the displacement current ($\partial D/\partial t$) can be ignored and the equation can be simplified to Ampere's original equation which did not include the displacement current:

$$\nabla \times H = J$$

Taking the divergence of both sides, while using the fact that the divergence of the curl of a vector field is always 0, yields:

$$\nabla \cdot (\nabla \times H) = \nabla \cdot J = 0$$

One can divide the current density into a stimulation current component (J_s) and a tissue transmission componenent (J_t) as:

$$J = J_s + J_t$$

resulting in the stimulation current density and tissue current density being equal and opposite. That is, for an arbitrary volume containing an electrode, the tissue current leaving the volume is equal to the stimulation current entering the volume.

The tissue component obeys Ohms law:

$$J_t = \sigma E$$

where is the tissue conductivity and is anisotropic and E is the electric field intensity, related to the electric potential (Φ) by:

$$\mathrm{E} = -\nabla\Phi$$

Consolidating:

$$\nabla \cdot J_s = \sigma \nabla \cdot \nabla\Phi$$

$$\nabla \cdot J_s = \sigma \left[\frac{\partial^2\Phi}{\partial x^2} + \frac{\partial^2\Phi}{\partial y^2} + \frac{\partial^2\Phi}{\partial z^2}\right]$$

which is the equation to be solved numerically with J_s defined as current densities on electrode surfaces and tissue conductivity defined anisotropically for neural tissue.

2.3 References

Bawa, Parveen NS, Kelvin E. Jones, and Richard B. Stein. 2014. “Assessment of Size Ordered Recruitment.” *Frontiers in Human Neuroscience* 8 (532):1–3.

Burke, R E. 1968. “Firing Patterns of Gastrocnemius Motor Units in the Decerebrate Cat.” *Journal of Physiology* 196 (3):631–54.

Clamann, H Peter, and Elwood Henneman. 1976. “Electrical Measurement of Axon Diameter and Its Use in Relating Motoneuron Size to Critical Firing Level.” *Journal of Neurophysiology* 39 (4):844–51.

Dideriksen, Jakob L, and Dario Farina. 2014. “Motor Unit Recruitment by Size Does Not Provide Functional Advantages for Motor Unit Performance.” *Journal of Neurophysiology* 8 (234):1–3.

Duchateau, Jacques, and Stephane Baudry. 2014. “Maximal Discharge Rate of Motor Units Determines the Maximal Rate of Force Development during Ballistic Contractions in Human.” *Frontiers in Human Neuroscience* 8 (234):1–3.

Enoka, Roger M., and Andrew J. Fuglevand. 2001. “Motor Unit Physiology: Some Unresolved Issues.” *Muscle & Nerve* 24 (1):4–17. https://doi.org/10.1002/1097-4598(200101)24:1<4::AID-MUS13>3.0.CO;2-F.

Fuglevand, Andrew J., David A Winter, and Aftab E Patla. 1993. “Models of Recruitment and Rate Coding Organization in Motor-Unit Pools.” *Journal of Neurophysiology* 70 (6):2470–88.

Gustafsson, B, and M. J. Pinter. 1984. “An Investigation of Threshold Properties among Cat Spinal Alpha-Motoneurones.” *Journal De Physiologie* 357 (April):453–83.

Harrison, PJ. 1983. “The Relationship between the Distribution of Motor Unit Mechanical Properties and the Forces Due to Recruitment and to Rate Coding for the Generation of Muscle Force.” *Brain Research* 264:311–15.

Heckman, CJ, and Roger M. Enoka. 2012. “Motor Unit.” *Comprehensive Physiology* 2 (October):2629–82.

Henneman, Elwood. 1957. “Relation between Size of Neurons and Their Susceptibility to Discharge.” *Science* 126 (3287):1345–47.

Henneman, Elwood, George Somjen, and David O Carpenter. 1965a. “Excitability and Inhibitability of Motoneurons of Different Sizes.” *Journal of Neurophysiology* 28:599–620.

———. 1965b. “Functional Significance of Cell Size in Spinal Motoneurons.” *Journal of Neurophysiology* 28:560–80.

Kernell, D, and A. W. Monster. 1981. “Threshold Current for Repetitive Impulse Firing in Motoneurones Innervating Muscle Fibres of Different Fatigue Sensitivity in the Cat.” *Brain Research,* no. 229:193–96.

Milner-Brown, HS, RB Stein, and R Yemm. 1973. “Changes in Firing Rate of Human Motor Units during Linearly Changing Voluntary Contractions.” *Journal of Neurophysiology* 230:371–90.

Moritz, Chet T., Benjamin K Barry, Michael A Pascoe, and Roger M. Enoka. 2005. “Discharge Rate Variability Influences the Variation in Force Fluctuations across the Working Range of a Hand Muscle.” *Journal of Neurophysiology* 93:2449–59.

Riek, Stephan, and Parveen NS Bawa. 1992. “Recruitment of Motor Units in Human Forearm Extensors.” *Journal of Neurophysiology* 68:100–108.

Taylor, Anna M, Evangelos Christou, and Roger M. Enoka. 2003. “Multiple Features of Motor-Unit Activity Influence Force Fluctuations during Isometric Contractions.” *Journal of Neurophysiology* 90:1350–61.

Taylor, Anna M, Julie W Steege, and Roger M. Enoka. 2002. “Motor-Unit Synchronization Alters Spike -Triggered Average Force in Simulated Contractions.” *Journal of Neurophysiology* 88:265–76.

Yao, Wanxiang, Andrew J. Fuglevand, and Roger M. Enoka. 2000. “Motor-Unit Synchronization Increases EMG Amplitude and Decreases Force Steadiness of Simulated Contractions.” *Journal of Neurophysiology* 83:441–52.

Zajac, F E, and Joel S. Faden. 1985. “Relationship among Recruitment Order, Axonal Conduction Velocity, and Muscle-Unit Properties of Type-Identified Motor Units in Cat Plantaris Muscle.” *Journal of Neurophysiology* 53 (5):1303–21.

Chapter 3: Recording

3.1 Introduction

In the U. S. there are approximately 1.6 million people who have had a limb amputated with roughly 185,000 new cases every year. 45% of these are due to trauma and are good candidates for a prosthetic limb because they are otherwise generally healthy (Ziegler-Graham *et al*. 2008). One might assume that a large percentage of these trauma-related injuries are due to U. S. Military operations and, thus, will drop as foreign policy changes. However, the total number of major limb and partial amputations (fingers/toes) in military personnel over the 2001 to 2010 time-period was 1621 (Fischer 2010). Therefore, the majority of amputations are civilian related; thus, the number of new cases will only increase with population growth.

Recently, several elegant motorized prosthetic limbs (*e.g.* JPL, DEKA) have been designed that are capable of multiple degrees of freedom in motion control by the subject (Miller *et al*. 2008; Micera *et al*. 2008). There are a variety of recording modalities by which an amputee could gain volitional control over these motorized prosthetics. For instance, a Brain Computer Interface (BCI) could be used to determine motor intentions directly from the subject's central nervous system. Penetrating electrodes can provide high-quality recordings of single neurons and have been used to control prosthetic limbs in multiple dimensions (Taylor, Tillery, and Schwartz 2002; B. Wodlinger *et al*. 2015). However, the brain elicits a foreign body response in which various astrocytes and microglia surround the electrode and encapsulate it causing signal quality to diminish dramatically over time (Bjornsson *et al.* 2006; Williams *et al.* 2007). Other invasive BCI modalities such as electrocorticography have shown to be more durable and can provide a

viable control signal for years (Leuthardt *et al.* 2004; Rouse and Moran 2009). Finally, non-invasive recording modalities such as EEG could be used for BCI of control of a motorized prosthetic; however, the EEG signal's bandwidth and spatial resolution is much lower, making high fidelity control over multiple degrees of freedom challenging (Nicolas-Alonso and Gomez-Gil 2012).

The peripheral nervous system can also be used to control a motorized prosthetic. For instance, electromyogram (EMG) signals from muscles in the proximal stump that are still intact (e.g. biceps and triceps in a distal trans-humeral amputation) can be decoded for prosthetic hand control. While this approach is typically non-invasive since the EMG electrodes are often applied to the skin's surface, it requires a mental translation to flex certain muscles (e.g. triceps) in order to control the hand. Although this translation gets more natural with practice, it is never as natural as the normal signal path (Micera *et al*. 2008). Further, the human hand has a large number of degrees of freedom. It is challenging to have enough unique muscle patterns to adequately handle this richness (Navarro *et al*. 2005). A variant of this technique, Targeted Muscle Reinnervation (TMR), surgically reroutes the nerves that originally innervated the hand into the stump muscles (e.g. pectoralis muscle in chest in a full arm amputation). When the subject activates peripheral nerves to move his former hand, the reinnervated muscle contracts. Using standard EMG electrodes, the stump muscle activity now representing hand function can be decoded and used to control a prosthetic. The subject's phenomenology is that of using the original hand, not the pectoral muscles (Kuiken TA *et al*. 2009). This overcomes the translation problem, but involves invasive surgery.

Finally, a peripheral neural interface (PNI) can be used to record and decode the subject's motor intention using the alpha motor unit axons that originally innervated the lost limb. There are many types of PNIs, but they can be broadly divided into three families: non-penetrating; penetrating; and regenerative. The cuff electrode is the exemplar of a non-penetrating electrode (Naples *et al.* 1988; Veraart, Grill, and Mortimer 1993; Grill and Mortimer 1995). It consists of an insulating cylindrical sheath that wraps around the nerve with 1 or more contacts on the inside face. Since this electrode does not penetrate any part of the nerve, it is the least invasive. However, it also does not provide the ability to detect or selectively stimulate small populations of axons (Navarro *et al.* 2005; Hassler, Boretius, and Stieglitz 2011). To get around this, novel electrodes that reorganize nerve geometry (i.e. FINE electrodes) combined with current steering strategies have been incorporated to make cuff electrodes more selective to specific fascicles (Tyler and Durand 2002; Brian Wodlinger and Durand 2009).

To increase peripheral nerve activation specificity, several types of electrodes that penetrate the epineurium - the sheath that surrounds the nerve – have been designed for prosthetic control. Longitudinal intra-fascicular electrodes (LIFEs) contain multiple contacts and are inserted into a fascicle along the length of the fascicle or longitudinally (Goodall, Lefurge, and Horch 1991). Transverse intra-fascicular multichannel electrodes (TIMEs) also contain multiple contacts are inserted sideways through the fascicle (or multiple fascicles) (Boretius *et al.* 2010). In either case, more than one electrode can be used so that there are contacts in all fascicles of interest (Navarro *et al.* 2005; Hassler, Boretius, and Stieglitz 2011). Slant electrode arrays like the Utah Slant Electrode Array (USEA) could be considered in the category of transverse intra-fascicular electrodes since they also have multiple contacts that are oriented axially across the nerve (Branner, Stein, and Normann 2001).

LIFE electrodes have been used by Micera *et al.* to try to decode motor commands to a prosthetic hand by an amputee. Electrodes were implanted in the medial and ulnar nerves of the subject (Micera *et al.* 2011). Specifically, they used thin-film LIFEs (tfLIFE), which were developed on a micropatterned polyimide substrate (Yoshida, Hennings, and Kammer 2006). Prior to implantation, the substrate filament was folded in half so that each side had four active recording sites. A tungsten needle, linked to the polyimide structure was used to implant the electrode. Thin-file TIMEs (tfTIMEs) have also been constructed and implanted using similar methods (Boretius *et al.* 2010). Micera and colleagues were able to achieve good classification accuracy (85%) between the different hand actions they tested for (various gripping and finger movements) (Micera *et al.* 2011). Dhillon and Horch performed a similar study and was able to discern motor signals (Dhillon and Horch 2005).

The third type of peripheral neural interface is the sieve or regenerative electrode (Marks 1969; Mannard, Stein, and Charles 1974). This type is by far the most invasive since their implantation requires transecting the nerve. However, they represent a likely candidate for being the most selective in decoding hand movement information. The most commonly used regenerative electrode is the sieve electrode, which consists of a many-holed disk (thus, the name sieve) with contacts spaced throughout (Akin *et al.* 1994; Stieglitz *et al.* 1996). To use this type of electrode, the nerve is transected and the electrode implanted between the two ends. The ends are sutured to the device allowing the proximal end of the nerve to regenerate through the sieve electrode and into the distal segment. This design appears to be a natural fit for prosthetic limbs since the nerve has already been severed once. In addition, the incidence of painful neuroma formation is high among amputees (Pet *et al.* 2014) which often require invasive surgery where

the nerve is transected again (Wu and Chiu 1999) allowing an ideal opportunity to implant a sieve electrode.

Early sieve electrodes were constructed by drilling holes through various materials including ceramic, Teflon™, epoxy and parylene (Kovacs, Storment, and Rosen 1992). That was followed by using silicon as a substrate which allowed for a higher quantity of smaller holes (Rosen, Grosser, and Hentz 1990). These early electrodes met with some success with axons growing back through the electrode and successful recordings of axonal activity from the electrode (Edell 1986; Akin *et al.* 1994; Zhao *et al.* 1997). The stiffness of silicon frequently caused compressive axonopathy where the neurons would grow through initially, then as the nerves grew wider or myelination formed, they would be compressed because the silicon hole would not flex. This caused the nerves to deteriorate. As a result, polyimide, a polymer with much greater flexibility, was used as a substrate, resulting in much better neural regeneration than with the silicon (Lago *et al.* 2005; Navarro *et al.* 2005).

In contrast with a flat disk with holes, micro-channel regenerative PNIs provide micro-channels up to several millimeters in length through which axons grow back (Suzuki *et al.* 2006). Initial investigation from a Cambridge team showed amplification of recorded extracellular action potentials within the channel via computational modeling (Fitzgerald *et al.* 2008), demonstrated fabrication techniques (Lacour *et al.*, 2008; Lacour *et al.*, 2010), biological feasibility and characterization (Lacour *et al.* 2009) and performed various *in-vitro* and *in-vivo* signal acquisition experiments confirming the high quality of signals that can be recorded from the device (Lacour *et al.*, 2010; Minev *et al.*, 2012; Fitzgerald *et al.*, 2012). The initial devices were constructed from polyimide with rectangular cross-sections of the micro-channels (Lacour *et al.* 2008), while the computational modeling used round holes less than 100 μm in diameter

(Fitzgerald *et al.* 2008). Biological feasibility showed better regeneration with larger 100 x 100 µm cross-section hole size (Lacour *et al.* 2009).

Subsequent work in peripheral nerve micro-channel interfaces used a similar design with different materials (Srinivasan *et al.*, 2011; Srinivasan *et al.*, 2015) or a simpler construction method of pouring PDMS around an array of micro-wires with the micro-wires removed after the PDMS hardened to create channels with a round cross-section (Kim *et al.*, 2015; Hossain *et al.*, 2015; Gore *et al.*, 2015). In these studies, *in vivo* neural signals were recorded from micro-wires inserted in the end of the channel instead of using the micro-fabrication process of metalizing the micro-channels as done by Lacour *et al*. (2010). These micro-wires, of course, partially occlude the micro-channel. Regeneration was tested across larger channel cross-sections replicating the prior finding that channel cross-sections 100 x 100 µm or larger have better regeneration than smaller channels (Srinivasan *et al.* 2015). Micro-channels were used to investigate the basic science question of how nerves regenerate (Hossain *et al.* 2015), and signals were recorded from awake behaving animals (Gore *et al.* 2015). Kim *et al.*, 2015 emphasizes the micro-channel's geometry minimizing cross-talk between recording electrodes, which indirectly points to the potential for this device type to minimize artifact from an adjacent stimulating electrode - a necessity for having a simultaneous, bi-directional PNI.

In this work, we determine through computational methods the expected electroneurogram (ENG) characteristics of regenerated nerves in biologically relevant micro-channel sizes (square channels with widths of 90 µm to 240 µm and lengths from 2 mm to 9 mm) and compare them to the tfTIME design successfully used to record and stimulate peripheral nerve axons in human subjects (Raspopovic *et al.* 2014). The micro-channel hole sizes are larger than those originally modeled by Fitzgerald and, thus, are more biologically relevant, the need for which was

mentioned in Srinivasan *et al.* 2015. We also model the combined effect of numerous axons firing in patterns typical of a motor neuron pool rather than a single action potential, simulating a full ENG. The expected ENG levels are a critical component in determining the recorded signal-to-artifact ratio of the device used in a bi-directional application. Additionally, the possibility of bipolar recordings within a micro-channel PNI are shown not to be feasible even in a very long channel. However, this does not preclude the bipolar and tripolar reference technique used by Srinivasan (Srinivasan *et al.* 2015) where the reference electrodes are outside the micro-channel.

A companion paper documents the stimulation current necessary for axonal stimulation, the associated stimulation artifact in neighboring micro-channels or electrode sites in the case of the tfTIME, and the optimal micro-channel device design to maximize signal-to-artifact ratio. Together, these papers show the feasibility and optimal design of a micro-channel sieve for a bi-directional neural interface and relative performance increase compared to the tfTIME.

3.2 Methods

An overview of the computational modeling process is briefly outlined here with details of the individual components explained in the subsequent sections.

Electrode site potentials resulting from transmembrane currents elicited as action potentials propagated along mammalian myelinated axons were modelled using NEURON (V. 7.1, Hines and Carnevale 1997), COMSOL multiphysics (V.4.3, COMSOL AB) and MATLAB (R2015b, The MathWorks Inc., Natick, MA, 2012) (Figure 3-1). In myelinated nerve fibers, such as motor fibers, nearly all the extracellular currents are generated from the nodes of Ranvier; thus, only nodal current was modeled. The composite current density (combining sodium and leak currents) through time from each node of Ranvier during an action potential was determined by

neural modeling software (NEURON) using nodal dynamics of myelinated mammalian nodes (CRRSS nodal model) (Chiu *et al.* 1979; Sweeney *et al.* 1989). Neural tissue within the regenerative PNI can be approximated as endoneurium (Jenq and Coggeshall 1985; MacEwan *et al.* 2016; Zellmer, MacEwan, and Moran 2017) which has an anisotropic electrical conductivity with the PNI device itself acting as an electrical insulator. For the TIME electrode, surrounding tissue was also modeled as endoneurium, modelling the electrode centered within a fascicle. Poisson's equation describes the dispersion of axonal current and associated electrical potential throughout the nerve and at the PNIs electrode surface. This equation was solved by a discrete partial differential equation solver (COMSOL) to find the electrical potential at the top of the micro-channel (or at TIME electrode sites) for a unit reference nodal current. To this end, an individual node of Ranvier was modeled as a cylinder with current flowing out the side. This cylinder was moved throughout the modeled endoneurium, showing the effect of a single node of Ranvier on the PNIs recorded voltage for nodes located at various positons within the PNI and in the nerve trunk. The stochastic firing times of differing sizes of axons was determined in MATLAB using the Fuglevand (Fuglevand, Winter, and Patla 1993) model for the firing characteristics of neurons in a motor neuron pool across neural drive (the desired intensity of motion). Additionally, MATLAB was used to generate random placement of axons around the TIME device or within a micro-channel, and combine the effects of the current flows from multiple nodes of Ranvier across multiple axons through time into a simulated recording or ENG. Finally, MATLAB was used to extract basic signal parameters that could be decoded from the ENG to generate control signals for a prosthetic limb.

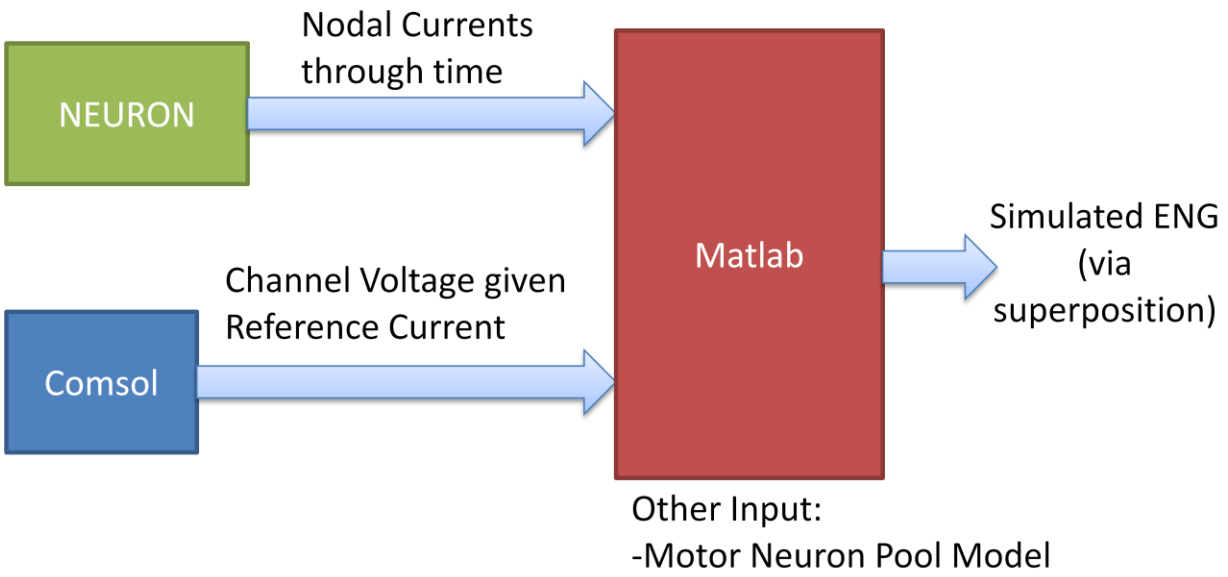

Figure 3-1. Overview of ENG Recording Model. Model axons were randomly placed around/through the device in MATLAB. Firing times were determined from a model of the Motor Neuron Pool. The current at each node of Ranvier at each 1 μs time slice through an action potential (modeled in NEURON using CRRSS model nodal dynamics) was used to scale the electrode potential due to a 1 μA reference current from the Node's location (modeled in COMSOL) in MATLAB. The scaling and summation (via superposition) of the effect of each node of Ranvier of each firing axon during an action potential creates the total ENG signal at that time slice.

3.2.1 Differences between normal and regenerated axons

Since micro-channel PNIs require neural regeneration while tfLIFEs do not, it is important to recognize and capture in the computational model any pertinent differences between regenerated and normal, undamaged axons. Over a century ago, it was recognized that there are morphological differences between normal axons and those that have undergone a trauma such as being crushed or severed (Greenman 1913). After being crushed or severed, axons degenerate both distal to the injury, but also proximally (McQuarrie 1985). Regenerated fibers are initially smaller, but eventually grow back to normal diameter following a crush (Gutmann and Sanders 1943; Hildebrand *et al.* 1985; Fugleholm, Schmalbruch, and Krarup 2000). However, nerve transection results in a permanent reduction in distal axon size and affects the ratio of myelin thickness to axon diameter (Gutmann and Sanders 1943). Conduction velocity also is slower

(Sanders and Whitteridge 1946) than normal axons. Further, internode length (distance between nodes of Ranvier) linearly increases with axon diameter for normal axons, but becomes nearly constant across axon diameters microns in regenerated axons (Hiscoe 1947; Vizoso and Young 1948; Beuche and Friede 1985).

These differences were used throughout the computational modeling described herein. For micro-channel devices, regenerated axon characteristics were used, while the tfLIFE modeling used normal axons. This study used the same morphometric values as (Zellmer, MacEwan, and Moran 2017).

3.2.2 Nodal current time course

In order to estimate the potential on recording electrodes elicited during propagating action potentials in motor axons, a determination had to be made of the magnitude and timing of sources and sinks along individual fibers. Therefore, computational modeling was carried out to determine the current flow over time of axons' nodes of Ranvier during an action potential. Axons with 49 nodes of Ranvier varying in size across a 2 µm - 11 µm diameter range were modeled in NEURON using the CRRSS nodal dynamics model as discussed in (Zellmer, MacEwan, and Moran 2017). To initiate an axon potential, the extracellular voltage of the first 2 nodes was set to -50 mV for the first 200 µsec (150 µsec for 2 - 3 µm fibers). The sum of the sodium and leak current densities, the only currents considered by the CRRSS model, were computed and stored at 1 µsec intervals. The current density was multiplied by the surface area of the node of Ranvier to determine the total nodal current.

3.2.3 Recorded voltage due to a node of Ranvier

To simulate recordings from individual fibers, nodal transmembrane currents were then translated to extracellular potentials. Electrical potential at the PNIs electrode(s) resulting from a unit current originating from an individual node of Ranvier was determined using COMSOL, a finite element model solver, given a reference 1 μA current. The nodes of Ranvier were modeled as cylinders with a current density normal to the side of the cylinder. As it was desired to model axons with diameters in the 2 - 11 μm range, the diameter of the nodes of Ranvier for both normal and regenerated axons across that range is 0.9 to 3.8 μm. The node length is 1 μm regardless of axon size or whether it is regenerated or undisrupted (normal). To reduce computational complexity, a single nodal diameter of 1 μm was typically used in COMSOL with the resulting voltage profile applied regardless of the axon diameter. To confirm the validity of this simplification, test runs were performed on the tfTIME model and two different micro-channel geometries (9 mm long by 240 μm wide and 3 mm long by 90 μm wide) while varying the radius (1, 2 3, and 5 μm) of the node and its proximity to the recording electrodes. The effect on electrical potential at the electrode was negligible. The simulated node of Ranvier was moved throughout the model space (a 1 mm diameter, 16 mm long cylinder) to create a spatial sampling. For both micro-channel and TIME devices, the node was moved axially through the space parallel to the direction of the axons with sparser coverage at greater distances from the recording sites.

3.2.4 Firing Rate of Individual Neurons

The two prior subsections provide sufficient information to simulate recordings from a single motor unit axon. However, in a biological system, motion occurs when many motor neurons fire concurrently, resulting in a complex ENG. Thus, the firing rate of different sized axons needs to

be determined as the neural drive, *u*(t), or desired intensity of motion increases. The collection of all motor neurons (MNs) that innervate a given muscle is the motor neuron pool for that muscle. The general principle that muscle force is increased by a combination of increasing the fraction of MNs in the pool that are active (recruitment) and increasing the firing rate of the already active MNs was known when Burke and Henneman wrote classic papers on the topic in the 1950s and 60s (Henneman, 1957; Henneman *et al.*, 1965a; Henneman *et al.*, 1965b; Burke, 1968). Henneman and Clamann also showed that smaller neurons with smaller axons have a lower threshold to begin firing (referred to as the activation or recruitment threshold) with additional neurons being recruited in size order (Clamann and Henneman 1976). This is called "the size principle" and is fundamentally intact today as the order by which MNs are recruited.

Fuglevand and colleagues created a widely used computational model that simulated the combined processes of recruitment and increased firing rates within a motor neuron pool. In brief, the recruitment threshold for excitation (RTE) was modeled as an exponential distribution where there are many small MNs with low thresholds and fewer large MNs with higher thresholds. When a neuron is first activated, it was modeled to fire at a minimum firing rate (8 spikes per second (sps)) which increased linearly as a function of the desired neural drive until reaching a maximum firing rate or plateau level (42 sps). All MNs were activated at 75% neural drive and had the same slope (change in firing rate / change in neural drive) such that the last neuron to be activated would reach the maximum firing rate at 100% neural drive. The firing rate of each neuron was computed as a function of neural drive and converted to a mean interspike interval (ISI). The computed ISI was used as the mean value to generate normally distributed ISI samples. The variance was chosen ensure a constant coefficient of variation (CV) of 0.2 where CV is defined as the distribution's standard deviation divided by its mean. To generate firing

times for the neuron, these ISI values were sequentially summed (Fuglevand, Winter, and Patla 1993). While later stages of Fuglevand's model are concerned with muscle force generation, our interest is the axonal currents which depend on axon size. Thus, we used the known distribution of rat myelinated axon diameters paired with increasing RTE values in axon size order, i.e. following the size principle, to calculate the extracellular ENG of the motor pool at various levels of neural drive.

3.2.5 Simulated ENG

To simulate the ENG, axons were randomly placed either passing through a micro-channel or passing around a TIME device. The number of axons was chosen based on the axon density reported in Lacour (Lacour *et al.* 2009) for 100 µm x 100 µm square channels which were the largest channels investigated in that paper. For that size, numerous channels had > 20 axons present. There was also a trend upwards as channel size became larger. This was presumably due to much of smaller channels being taken up by connective tissue associated with micro-fascicles. In a similar study, Srinivisan compared regeneration in 50 µm x 100 µm, 100 µm x 100 µm and 150 µm x 100 µm micro-channels showing much better regeneration in the medium and larger channels. In that study, the 100 µm x 100 µm micro-channels were analyzed further, with the number of axons within each channel counted. The plurality of channels had between 11 and 100 axons (40%) with 30% having greater than 100 axons (Srinivasan *et al.* 2015). Taking an average representation from these studies, we treated 0.25 axons per 100 μm^2 as an average value - corresponding to 25 axons in a 100 µm x 100 µm square channel. However, both twice that value and half that value were also tested to assess the sensitivity to axonal density showing a modest linear change.

For a given axon density (axons/micron^2), the number of axons in the channel was computed based on the channel cross-sectional area for a micro-channel or within the radius of interest for a TIME device. Axons were then randomly placed within that cross-section with no special care taken to ensure that axons were not collocated.

ENG recordings were simulated for the various micro-channel geometries and at different radii of interest for the TIME device using neuronal firing times from the Motor Neuron Pool model, the nodal current time course data from NEURON, the location and size of the axons to be simulated, and the computed electrical potential given a reference current from a nodal location. The electrical potential due to a node was interpolated from the bounding reference values (see Recorded voltage due to a node of Ranvier) in each of the 3 spatial dimensions.

3.2.6 Decoding ENG for control signals

Basic control signals that could easily be implemented in real-time processing were computed from the simulated ENG data:

- Mean value of the rectified signal: $\frac{1}{N}\sum_{i=1}^{N}|x(i)|$, where there are N samples of the recorded ENG voltage time course, $x(i)$;
- Variance or average energy of the signal: $\frac{1}{N}\sum_{i=1}^{N}(x(i))^2$;
- Standard deviation of the signal: The square root of the variance computation;
- Average peak value: average of negative peak values determined by MATLAB's built-in findpeaks function with the following parameters:
  Minimum Peak Height (MINPEAKHEIGHT) = 0.2 x the minimum value in the run;
  Minimum Peak Distance (MINPEAKDISTANCE) = 20, corresponding to 20 μs;
- Temporal average of a peak detector circuit: the temporal average ($\frac{1}{N}\sum_{i=1}^{N} peak(i)$) of a modeled peak detector circuit where:
  $peak(0) = 0$
  $peak(i+1) = peak(i) \cdot (1 - DischargeRate)$ when $|x(i)| \leq peak(i)$
  $peak(i+1) = peak(i) \cdot (|x(i)| - peak(i)) \cdot ChargeRate$ when $|x(i)| > peak(i)$
  ChargeRate = 5e-2
  DischargeRate = 5e-5.

Each control signal was computed from 2 seconds of simulated ENG with a sampling period of 1 μs.

3.3 Results

The time course of current from nodes of Ranvier were computed for normal and regenerated axons with sizes of 2 to 11 μm in 1 μm increments. Figure 3-2 shows nodal currents for 5 μm diameter axons. For this size, the internodal distance for normal axons was 680 μm, while it was 297 μm for regenerated axons. As a result, the action potentials for adjacent nodes in the regenerated axons are much closer together temporally since they are also much closer together spatially. The action potential conduction velocity in the regenerated axon is however slower than in the normal axon.

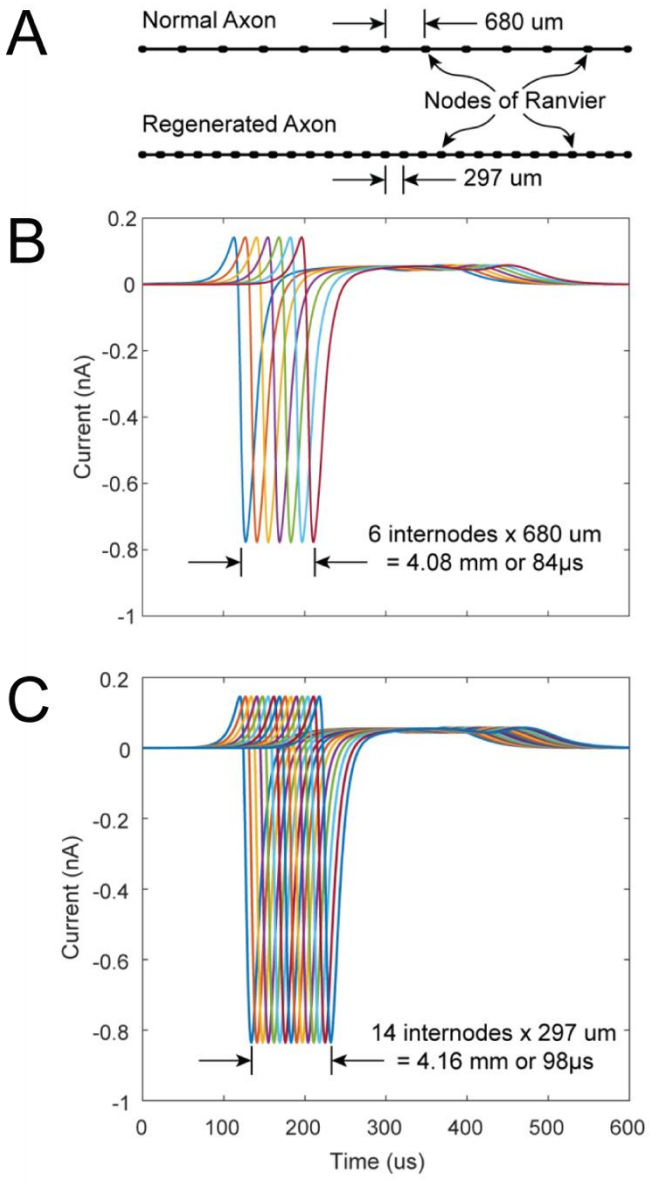

Figure 3-2. Time course of a normal and regenerated 5 µm diameter axons nodal currents. A: Relative nodal geometry of a normal axon (upper trace) and regenerated axon (lower trace) showing that regenerated axons have closer internodal spacing. B: Nodal current time course for 7 nodes (~4 mm) of a normal axon. C: Nodal current time course for 15 nodes (~4 mm) of a regenerated axon. The nodal currents are very similar from normal to regenerated axons, but the propagation velocity is slower in the regenerated axon.

The electrical potential caused by a unit reference current from a simulated node of Ranvier for nodal locations throughout the simulation space was determined for the location of the recording electrode (for the TIME device) or 41 locations across the top of the micro-channel (for micro-

channel devices). For the TIME device, this is one set of data. For the micro-channel devices, this is a set of data for each geometry, i.e. combination of length and width. Figure 3-3 shows the potentials for axial nodal locations on an axon running down the center of a 3 mm long, 120 µm wide micro-channel compared to an axon located 60 µm directly above a TIME contact. In each case, the peak electrical potential is reached when the node is closest to the device's electrode - when the axial distance is 0. However, the micro-channel's peak voltage is about 10 times greater than that recorded from the TIME from an equidistant axon.

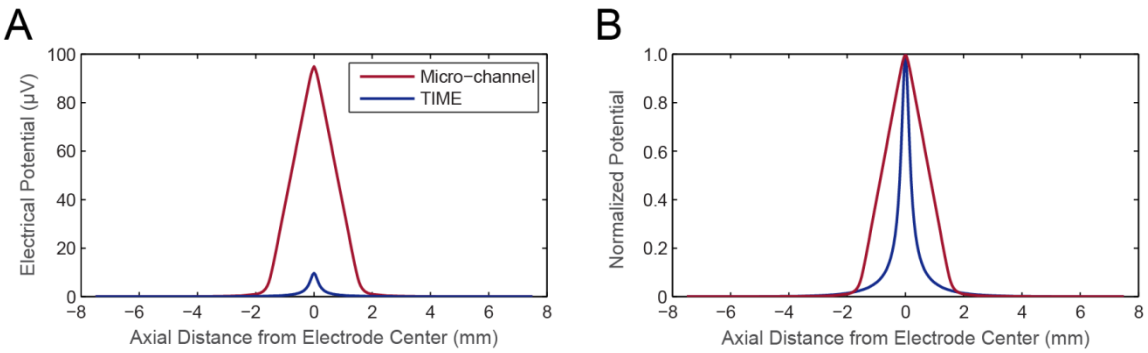

Figure 3-3. A: Electrical Potential at recording electrode for a reference nodal current moved axially along an axon. Axon is 60 µm above TIME recording electrode for the TIME trace and is in the center of a 120 µm wide, 3 mm long, micro-channel for the micro-channel case. The recorded electrical potential is about 10 times larger for the micro-channel than for the TIME given the same nodal current. B: Normalized electrical potential for a reference nodal current moved axially along an axon illustrating electrical field characteristics within and outside the micro-channel.

The Fuglevand motor neuron pool model was used with distribution of axon sizes appropriate for the device type (Figure 3-4) - regenerated axons for the micro-channel devices and normal axons for the TIME. At low neural drives, many low threshold motor neurons initially start firing. As neural drive increases, already active neurons increase their firing rate up to their maximum firing rate while progressively fewer, larger, higher threshold neurons are recruited, albeit at a low firing rate. This process continues until all neurons are firing, many at their maximum rate, then to a point where all neurons are firing at their maximum rate of 100% neural drive (Figure 3-4C).

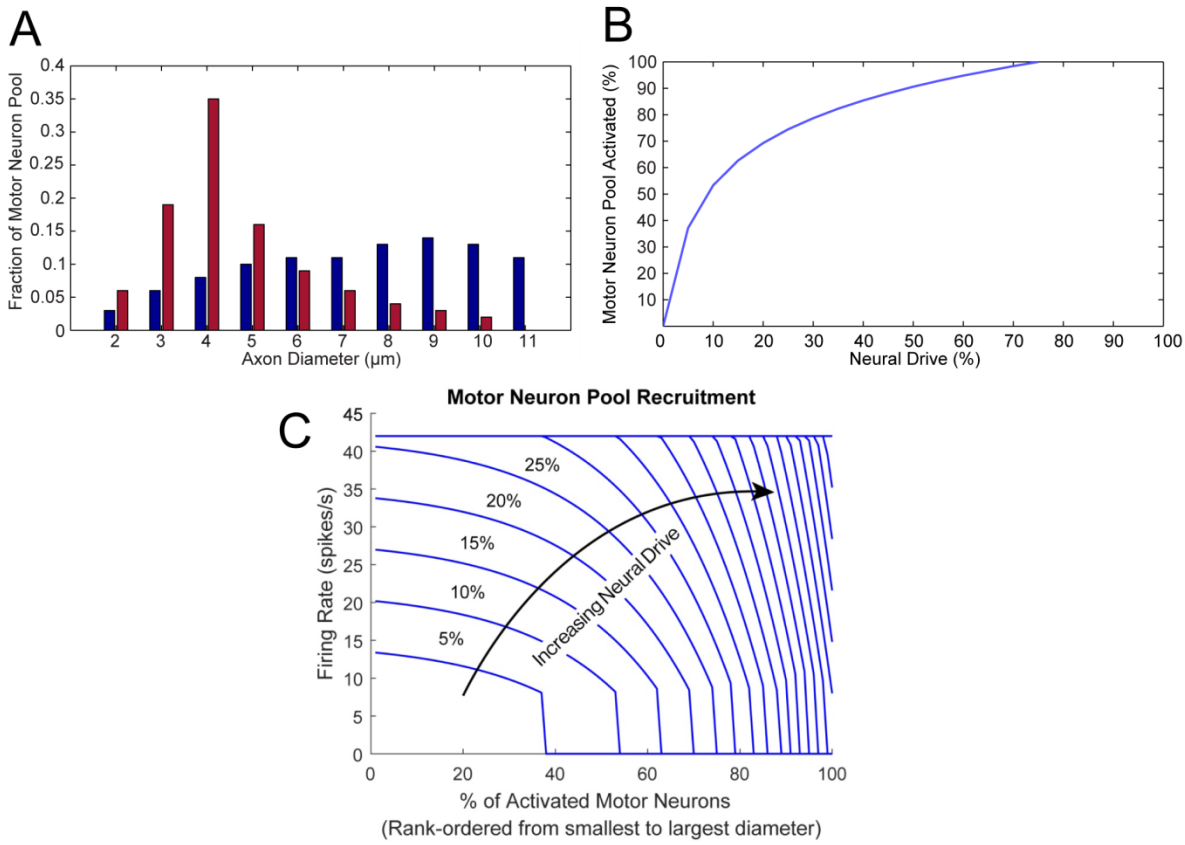

Figure 3-4. Motor neuron pool recruitment. A: Distribution of axon sizes for regenerated (red) and normal (blue) axonal populations. Regenerated axons are generally smaller in diameter. B: Cumulative distribution of motor unit recruitment as a function of neural drive. Initially, many, small neurons fire. As neural drive increases, larger, less numerous, neurons begin firing. C: Firing rate of motor neurons as a function of neural drive. Individual traces show firing rates across the motor neuron pool for a given neural drive. Increasing neural drive results in increased firing rates for already active neurons as well as recruitment of non-firing neurons.

ENG data was simulated from randomly placed axons with diameters stochastically assigned based on the size distribution shown in Figure 3-4. Each simulation was 2.5 seconds in length with the first 400 ms and last 100 ms excluded to minimize the axonal coherence at startup. Thus, 2 seconds of simulated ENG data was processed for each run. A few milliseconds of sample simulated ENG activity showing the effect of neural drive are shown for TIME and micro-channel devices respectively (Figure 3-5). For both devices, it is apparent that as the neural drive increases the firing pattern is more dense. That is, more action potentials are visible in the simulated ENG recordings. As drive increase, simulated ENG recordings also show larger

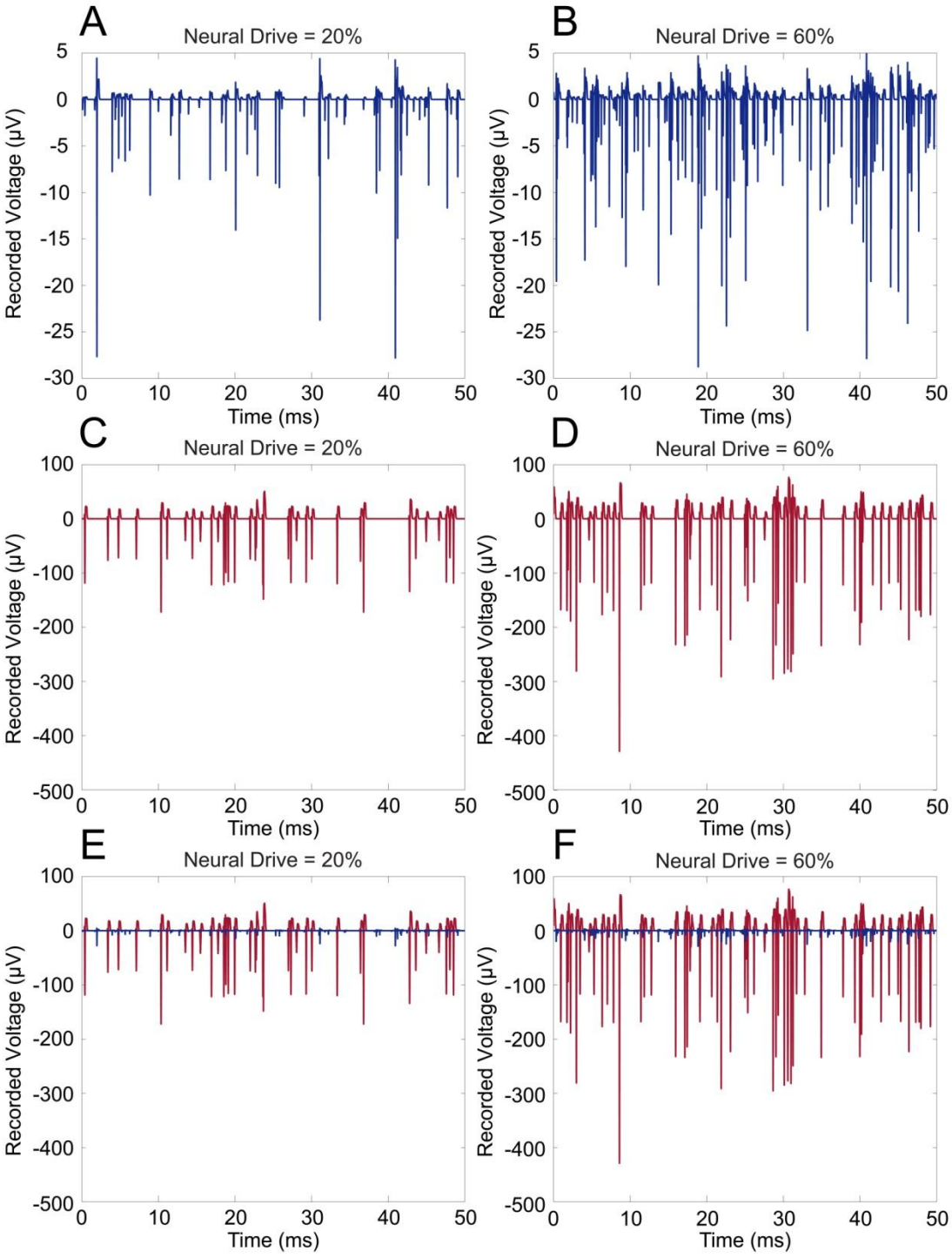

Figure 3-5. Comparison of simulated ENGs at 20% and 60% Neural Drive. A-B: Simulated TIME ENG (blue) from axons within 100 μm of the device for Neural Drive values of 20% and 60%. 20% Neural Drive has sporadic firing while 60% shows much denser firing with many mid-sized action potential. C-D: Simulated Micro-channel ENG (red) for a 120 μm wide, 3 mm long micro-channel as Neural Drive is increased. Again, 20% Neural Drive has sporadic firing while 60% has much larger action potentials. In either case, the recorded signal in the micro-channel electrode is an order of magnitude larger than the signal recorded by the TIME electrode (E-F).

neurons firing with larger action potentials in keeping with the "Size principle." This results in larger peak values as neural drive increases. Finally, consistent with Figure 3-3 showing the difference between TIME and micro-channel devices in electrical potential at the recording electrode, the micro-channel ENG has approximately 10 times greater peak values than would be recorded at the TIME.

Using both randomly selected axon locations and firing times, 1024 simulations were performed for each neural drive level to determine ENG characteristics (Figure 3-6A-B). In the TIME device, there was such high variability when both timing and location were randomized that additional simulations were performed with only the timing being randomized. Thus, using a single set of randomly selected axon locations, multiple simulations were performed across neural drive values where the effect from the exact timing of the action potentials could be examined. The results for three random geometries of axons for the TIME (Figure 3-6C-H) and micro-channel devices (Figure 3-7C-H, bottom 3 rows) each with 32 different axon firing times (Figure 3-6 bottom had 64 firing times) are shown. TIME devices were sensitive to the exact placement of axons, yielding widely varying results across the three geometries while the variation was substantially reduced when only the firing time was random. Additionally, TIME devices tended to have the output saturate at a relatively low neural drive. On the other hand, the micro-channel ENGs were a near linear function of neural drive and were consistent from one axon placement to the next. Similar to the single axon simulation results, the ENG recorded on the micro-channel interface is an order of magnitude greater than the TIME device (Figure 3-8).

To determine the effect of device geometry (channel length and width) on peak voltages for the micro-channel devices, 16 simulations at each combination of length (2, 3, 4, 5, and 9 mm) and width (90 - 240 μm in 30 μm increments) were performed with randomized axon locations (axon

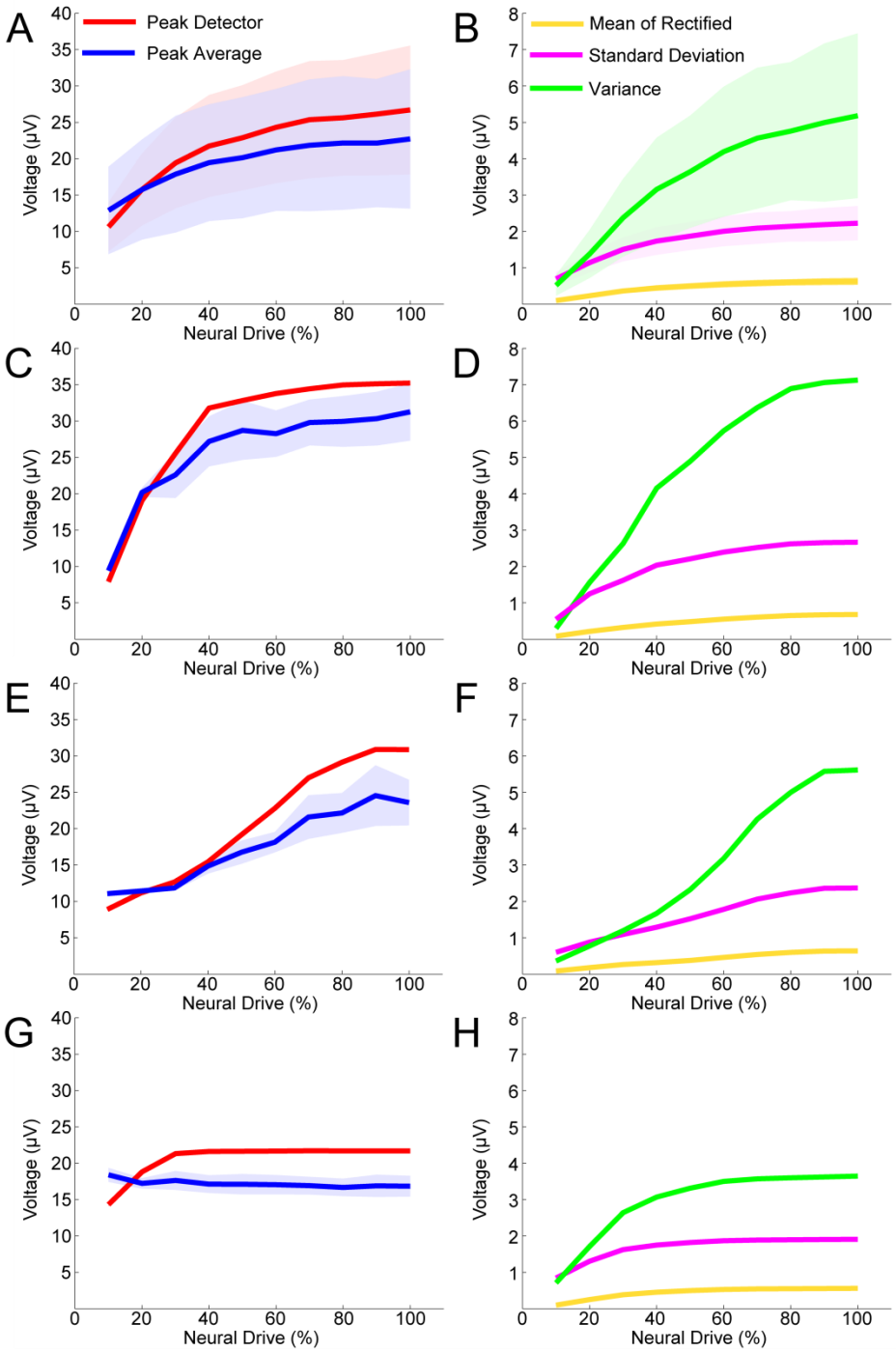

Figure 3-6. Variation in peak voltages (left column) and other control signals (right column) for randomized axon geometry and firing times (A-B) and 3 samples of fixed axon geometry (C-H) surrounding a TIME (75 µm radius of interest) where the variation in each of the 3 bottom rows is solely due to the specific time course of axon firing. A-B: Axon geometry and firing times were randomly selected (N=1024). Note large variability in performance. C-D: In this sample, saturation occurs in all measures making it difficult to discern the level of neural drive (N=32). E-F: Measures in this sample remained largely monotonic (N=32). G-H: Most measures saturated, the average peak level actually reduced as neural drive increased (N=64). Overall, there was wide variation in measures based predominately on the particular geometry of axons surrounding the TIME.

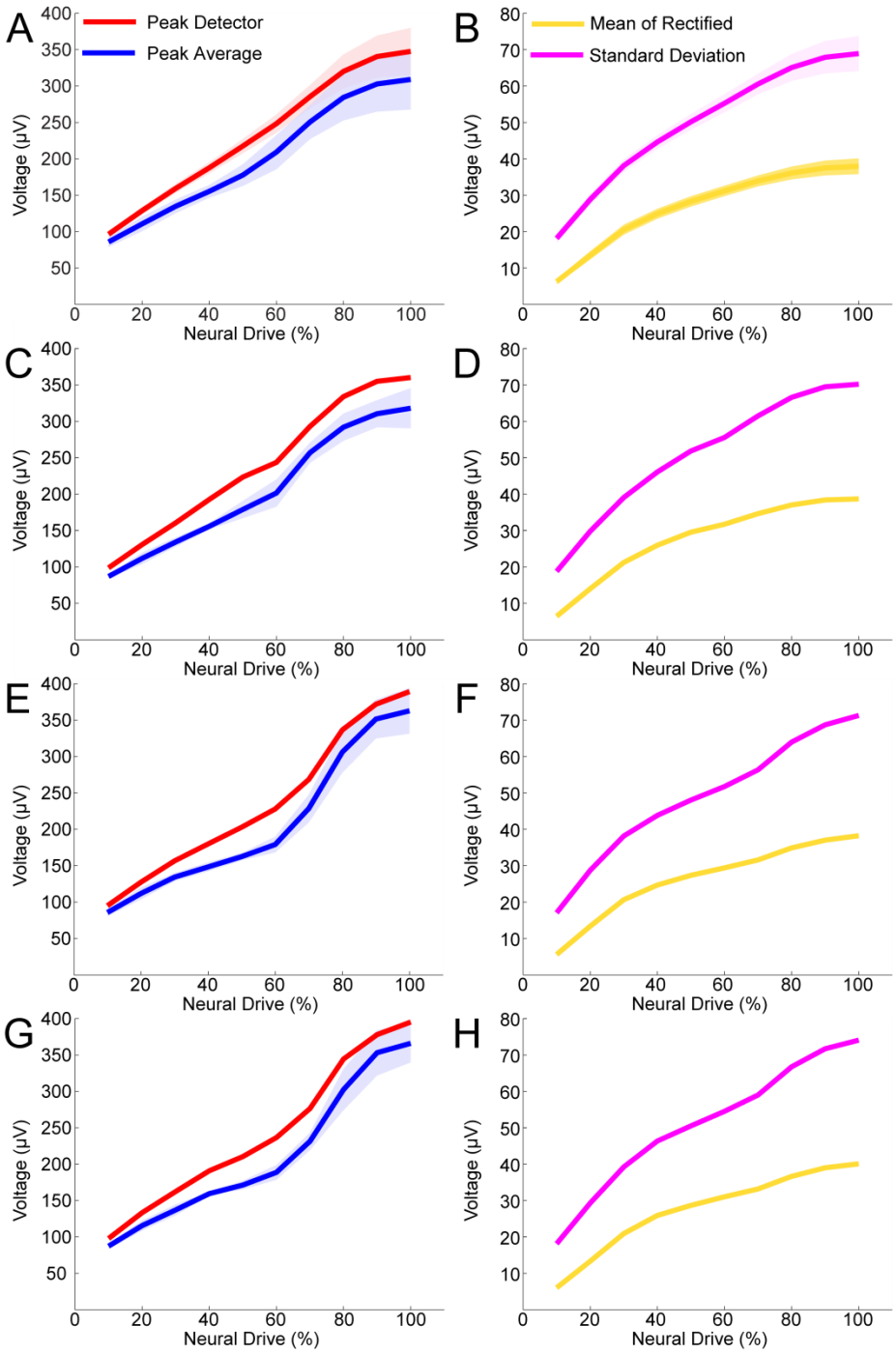

Figure 3-7. Variation in peak voltages (left column) and other control signals (right column) for randomized axon geometry and firing times (A-B) and 3 samples of fixed axon geometry (C-H) within a micro-channel device (5 mm length, 150 µm width, N=32) where the variation in each of the 3 bottom rows is solely due to the specific time course of axon firing. A-B: Axon geometry and firing times were randomly selected (N=1024). A-H: Measurements are far more consistent and linear than in the TIME case and are an order of magnitude greater, providing a much better indication of the patient's intention to move.

geometry) and firing times (Figure 3-9). As expected, narrower and longer channels result in higher peak values. The 9 mm long, 90 µm wide channel produces peak values in the 600 - 800 µV range! While a 9 mm may seem to be a long distance for a nerve to regenerate across, acellular nerve allografts are capable of supporting neural regeneration across a much longer distance of 3 cm (Saheb-Al-Zamani *et al.*, 2013; Poppler *et al.*, 2016).

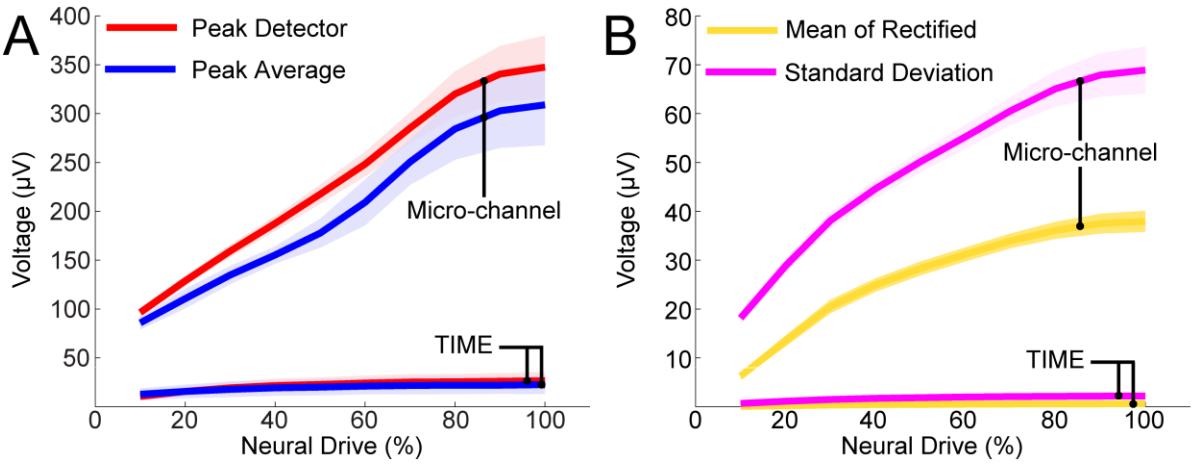

Figure 3-8. Comparison of variation in peak voltages (A) and other control signals (B) for randomized axon geometry and firing times for the micro-channel and TIME device.

3.4 Discussion

3.4.1 Extracting control signals from motor axonal activity

The modulation in a control signal as neural drive changes is one of the most important facets to consider in determining a control scheme for a prosthetic limb. It is strongly desired to be able to control the prosthetic limb's force output in a graduated way consistent with the desired force of the patient. That requires there to be a discernible difference in the control signal as excitation level is increased. For instance, comparing Figure 3-6 with Figure 3-7 reveals that, regardless of the metric extracted from the ENG data, the TIME device control signals are far more sensitive

to the precise location of motor axons relative to the recording electrode compared to the micro-channel device. This sensitivity is a reflected in the much larger relative variation in the control signals extracted from ENG signals recorded in the TIME device (compare Figures 3-6A-B with 3-7A-B or for specific examples compare 3-6C with 3-6G, relative to 3-7C with 3-7G). This lack of consistency is a function of the 1/r roll-off of electrical potential around a monopolar current source (*e.g.* node of Ranvier) in a volume conductor.

The micro-channel device, on the other hand, has a linear reduction in potential from current source to the edge of the channel (Figure 3-3). This provides less variability in signal amplitude due to reduced dependence on large axon location with respect to the PNIs recording electrode. This implies that a TIME device's performance may be highly dependent on its exact placement within a nerve and within individual fascicles. Detailed knowledge about the topographical organization of motor axons within a complex multifasicular nerve is not known prior to implantation. Therefore, electrode placement invariably includes significant unknowns even with excellent surgical technique. When using the TIME electrode, the presence of such unknowns will result to significant discrepancies in patient outcomes. Specifically, if multiple patients were implanted with the device, we would expect to be able to extract relatively precise and granular control signals in some of them (exemplified in Figure 3-6C), imprecise control in some of them (Figure 6E) and very poor control in some of them (Figure 3-6G). In contrast, very little such variability would be expected in patients implanted with the micro-channel device. Needless to say, such variability could limit the clinical viability of the former device.

Finally, all control signals show increase in magnitude over excitation level with signal compression around 80% excitation level. This property is particularly salient in the TIME control signals which saturate more sharply and at a lower neural drive (Figure 3-6).

3.4.2 Effect of micro-channel device geometry on recorded signals

The geometry of a micro-channel device makes a profound difference in the expected ENG amplitude. To maximize the recorded signal, the micro-channel should be designed to be as long and narrow as possible within the ability of axons to regenerate through the device. Since the neural tissue in the channel acts as a volume conductor, the long and narrow channels focus the current in a tighter space increasing current density which, in turn, increases the electric field (*i.e.*, $\vec{\boldsymbol{J}} = \boldsymbol{\sigma}\vec{\boldsymbol{E}}$). The wider and shorter channels allow current to spread more (even into extracellular space outside the micro-channel) thus reducing the electric field and its spatial integral – the electric potentials we record with our electrodes). Another way to look at it is that while volume resistivity does not change between channel sizes, the effective axial resistance along the channel increases with reduced cross-sectional area. It is the increased resistance seen by the axonal currents compared to extracellular space that causes the signal amplification seen in the micro-channels (Fitzgerald *et al.* 2008).

In this work, 90 µm micro-channel width was chosen as a minimum size that is currently viable for regeneration based on the work of Lacour and Srinivisan. The 90 µm width provides a large voltage increase over 120 µm and 150 µm which appear to surround the "knee" of the curve (Figure 3-9). For optimal length, Lacour and Srinivisan showed good regeneration in rats for micro-channel lengths up to 3 mm (Lacour *et al.* 2009; Srinivasan *et al.* 2015); thus, there appears to be little reason to go below 3 mm since a reduction in length leads to a reduction in recording amplitude, particularly for narrower widths (Figure 3-9). Techniques like adding nano-structures within the device or adding neurotrophic factors (Wood *et al.* 2009; Sivolella *et al.* 2014), which are used to enhance peripheral nerve recovery from a traumatic injury, could be

used to increase the regeneration length and potentially facilitate the utilization of longer/narrower channels in future systems.

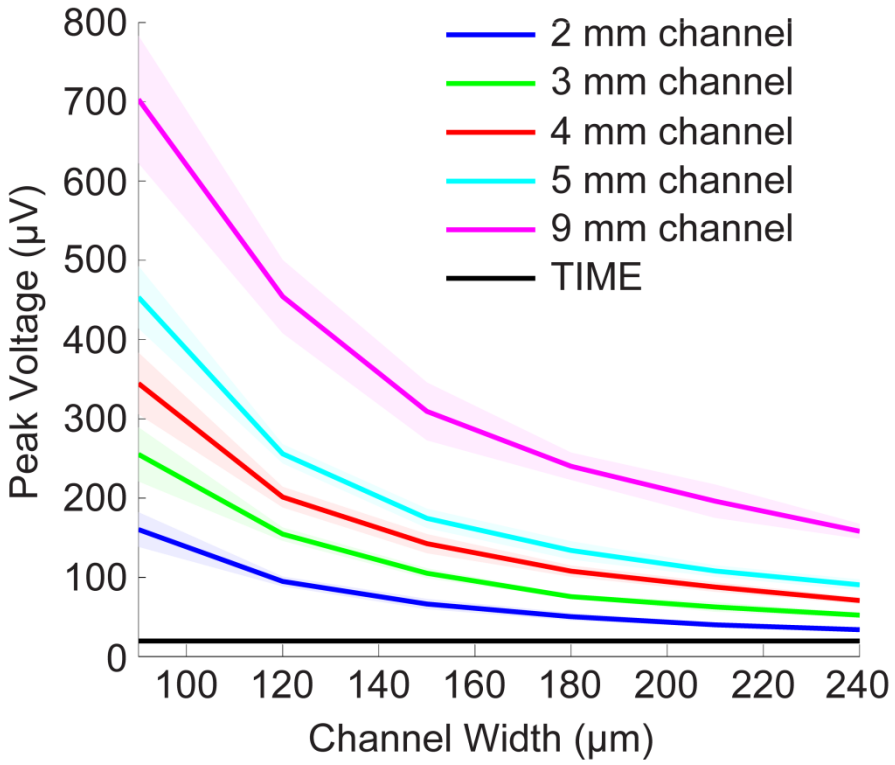

Figure 3-9. Variation in average peak signals over device geometry for the micro-channel electrode (50% neural drive, N=16 random geometries and axon firing times). Longer, narrower channels have larger peak ENG voltages. The TIME electrode (black) had lower peak voltages than all micro-channel devices.

3.4.3 Limitations of multi-polar recordings

Bipolar recording has an important advantage over unipolar recording. Since the recording is a differential recording, it rejects common mode noise or interference. In the case of peripheral neural recordings, a chief contributor to interference is the much stronger electrical signals from skeletal muscles (Hoffer *et al.* 1996). Because the ENG was computed at 41 evenly spaced locations across the top of the micro-channel device, bipolar recordings could also be modeled by differencing two locations, symmetric about the micro-channels longitudinal center (e.g. proximal and distal electrode sites in Figure 3-10A).

The comparison of unipolar and bipolar signals for a 3 mm long micro-channel is shown in Figure 10B. The combination of conduction velocity of the action potential in a myelinated axon with the number of simultaneously active nodes of Ranvier results in an action potential that is nearly as wide as the micro-channel lengths we investigated (Figure 3-2). Thus, the electrodes in the micro-channel are simply too close together to get a good differential signal (like the Expected trace in Figure 3-10D), resulting in partial cancellation of the desired signal in addition to noise. An additional complicating fact is that the peak potential occurs at channel center where there is high resistance to ground for the nodal current. The peak recording magnitude drops linearly from the center to the channel edge. What if a longer micro-channel were used? That could, at least mitigate the cancellation effect. If the channel were long enough, one could still place the recording sites relatively close to the center to maximize the recording amplitude. To answer this question, a much longer (50 mm) micro-channel was modeled in a 16 cm overall space with 501 Nodes of Ranvier. This is longer than the maximum 30 mm regeneration currently achievable using an acellular nerve allografts. However, ongoing research into the mechanisms that limit regrowth could make 50 mm a possibility in the next few decades (Saheb-Al-Zamani *et al.*, 2013; Poppler *et al.*, 2016). Regardless, the longer channel was primarily considered to test the hypothesis that the fundamental problem was the action potential length.

The overall methods herein were employed with a single 5 µm diameter axon centered within the micro-channel. The action potential was recorded at proximal, median and distal electrodes and the difference between the proximal and distal signals were unlike that expected for a bipolar recording (Figure 3-10D). Instead of having the odd symmetry of a negative peak followed by positive peak (or *vice versa*), there are two negative peaks. Further, the median and distal signals

look unusual (Figure 3-10C). Intuitively, we would anticipate these signals as being time-shifted versions of the proximal signal.

To further analyze the distal signal, the voltage time-course at that electrode was overlaid with individual traces from each node of Ranvier (Figure 3-11). These look normal. First, the shape of each individual curve shows the downward spike followed by a refractory period. Second, the magnitude of voltage traces increases linearly as the nodes become closer to the recording site. Finally, the magnitude decreases rapidly for nodes close to the distal edge of the micro-channel.

While the individual traces in Figure 3-11 look standard, their superposition or summation looks very different. Starting with the node of Ranvier (node 326) immediately underneath the distal electrode and progressively combining the contribution of nodes symmetrically around it generated an action potential that appeared normal (Figure 3-12A) for the first 17 nodes. Given the regenerated internodal distance of 297 μm for regenerated axons, this covers a distance of 4.7 mm which is a typical micro-channel length used in simulating recorded ENGs (Figure 3-9). However, as the number of nodes included is progressively increased, the shape of the recording changes dramatically. Specifically, the refractory period of the signal becomes as large as the initial depolarization phase. The final combination used 166 nodes proximal to the electrode and all the distal nodes; however, the distal nodes outside the micro-channel contribute very little to superposition. As seen in Figure 3-12B (cyan trace) the large superposition (effectively all the nodes in the 50 mm channel) matched the distal electrode recording seen in Figure 3-10C.

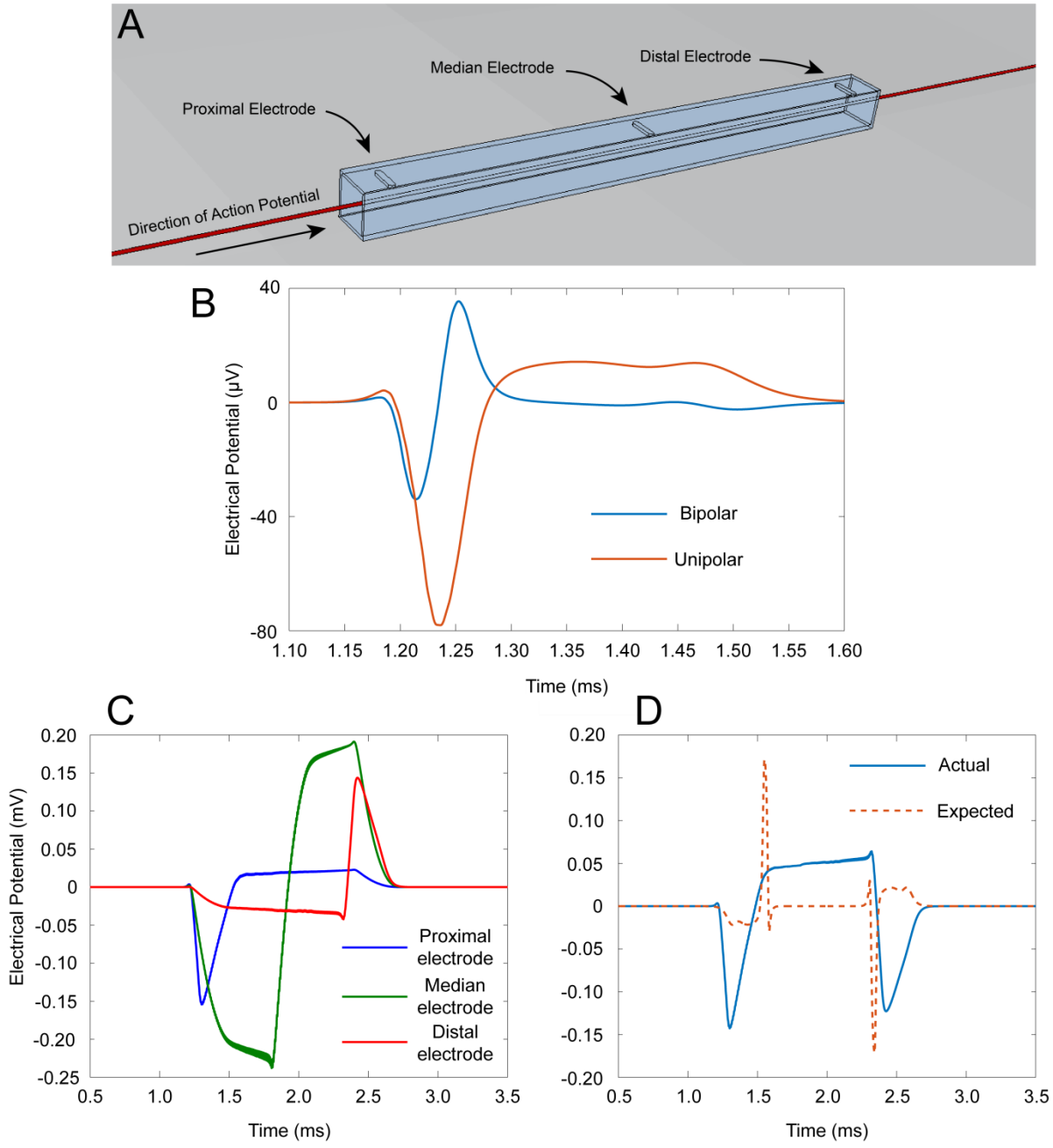

Figure 3-10. Multipolar recordings of an action potential (A.P.) in a micro-channel. A: The modeled axon (red) going through a micro-channel with three electrode locations marked. B: Comparison of unipolar and bipolar recordings in a 3 mm long, 180 μm wide micro-channel where the length of channel is less than the A.P. length. The bipolar recording is derived from differencing the proximal and distal electrode signals. C: The unipolar recordings from each of the three electrode sites in a 50 mm extra-long micro-channel. Median and distal signals are not time-shifted versions of the proximal signal as expected. Median signal is not part of the bipolar measurement, but is shown to demonstrate a normal unipolar recording in the center of a long micro-channel D: Modeled bipolar recording (blue) of a single action potential propagating through a 50 mm long micro-channel compared to the expected recording – the distal minus proximal signal using only a few nodes of Ranvier directly under each electrode which creates a signal much closer to a stereotypical action potential (as in B).

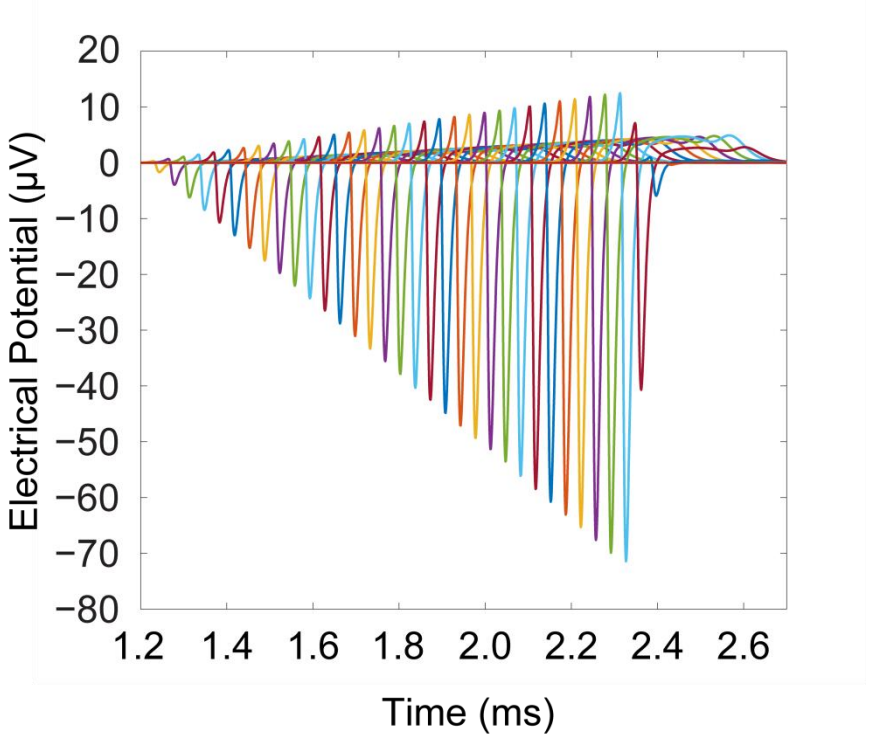

Figure 3-11. Action Potentials recorded at the distal electrode from every 5th Node of Ranvier within the micro-channel. The signals from proximal nodes peak sooner than more distal nodes showing the action potentials propagation down the axon. The magnitude of the recording from each node increases linearly as the node nears the recording site from the proximal side, but falls off dramatically distal to the recording site due to the nearness of the distal channel edge.

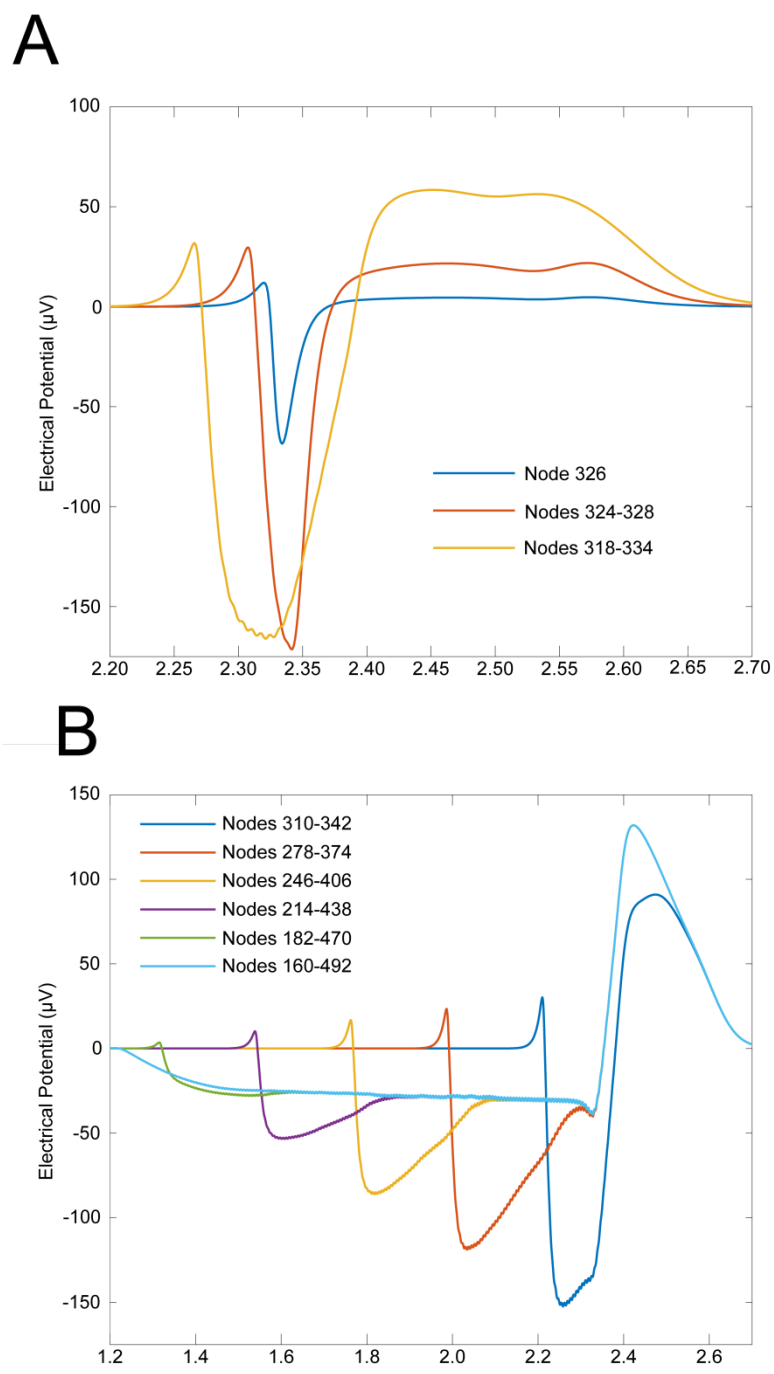

Figure 3-12. Voltage trace at distal micro-channel electrode due to progressively larger sets of Nodes of Ranvier centered on the node directly under the distal contact point (at ~47 mm into the 50 mm channel). Nodes 167 - 335 are the nodes inside the channel. A: Voltage trace due to the node nearest the electrode (Node 326) and the effect of combining a few surrounding nodes. The appearance of the action potential is normal with a depolarization spike and subsequent inward repolarization current. B: As more nodes are used, the recorded signal progressively looks more like the distal trace from Figure 3-10.

What is it about the currents in a micro-channel that cause this? There are two effects that interact. The first is that a current anywhere within a micro-channel has a larger affect throughout the channel than it would in the "free space" of a homogenous volume conductor. As previously stated, the dropoff in electrical potential due to a monopole current source is 1/r in a volume conductor. However, the electrical potential within the micro-channel decays linearly to the channel edge (Figure 3-2B). In essence, the micro-channel functions as a spatial low-pass filter making the voltage gradient gradual within the channel. The second effect is the non-linearity associated with the channel edges. As seen in Figures 3-2 and 3-11, the voltage within the channel decreases rapidly toward and beyond the edge of the micro-channel and is not a smooth function at the channel edge. Thus, the onset of the recorded action potential on the proximal end of the channel will only be affected by the relatively few nodes between it and the channel edge, but is affected by many nodes during the refractory period. On the other hand, the onset seen at the distal electrode is contributed to by all the nodes within the channel, but by very few nodes after it. This further explains why the recording at the median electrode is symmetrical. The spatial low-pass characteristic of the micro-channel amplifies the contributions of distant nodes while the electrode being in the middle of the channel provides symmetry since the non-linear edge effects are balanced.

In conclusion, micro-channels that an axon can currently regenerate through are too short for viable bipolar recording techniques. The spread of the action potential across multiple nodes of Ranvier combined with the conduction velocity and the spatial low-pass filtering of the micro-channel result in a nearly identical signal at both electrodes. This negates the effectiveness of the technique. Furthermore, if an axon was capable of regenerating through a much longer micro-channel, the recorded signal would look very different from a stereotypical bipolar recording.

However, the common-mode noise cancellation property should still be intact. Thus, the possibility of using techniques described earlier is still a possibility. However, successful implementation would depend on an axon being able to regenerate a few centimeters.

Finally, Srinivasan created bipolar signals by using an electrode immediately outside the channel (Srinivasan *et al.* 2015). Based on the work herein, that may work to eliminate common mode noise that permeates the entire space, but it will not create the characteristic bipolar signal (Figure 3-10D) since the magnitude of the recording outside the channel will be much smaller than that of the recording from inside the channel.

3.5 References

Akin, T., K. Najafi, R.H. Smoke, and R.M. Bradley. 1994. "A Micromachined Silicon Sieve Electrode for Nerve Regeneration Applications." *IEEE Transactions on Biomedical Engineering* 41 (4):305–13. https://doi.org/10.1109/10.284958.

Beuche, W., and R. L. Friede. 1985. "A New Approach toward Analyzing Peripheral Nerve Fiber Populations. II. Foreshortening of Regenerated Internodes Corresponds to Reduced Sheath Thickness." *Journal of Neuropathology and Experimental Neurology* 44 (1):73–84.

Bjornsson, C S, S J Oh, Y A Al-Kofahi, Y J Lim, K L Smith, J N Turner, S De, B Roysam, W Shain, and S J Kim. 2006. "Effects of Insertion Conditions on Tissue Strain and Vascular Damage during Neuroprosthetic Device Insertion." *Journal of Neural Engineering* 3 (3):196–207. https://doi.org/10.1088/1741-2560/3/3/002.

Boretius, Tim, Jordi Badia, Aran Pascual-Font, Martin Schuettler, Xavier Navarro, Ken Yoshida, and Thomas Stieglitz. 2010. "A Transverse Intrafascicular Multichannel Electrode (TIME) to Interface with the Peripheral Nerve." *Biosensors & Bioelectronics* 26 (1):62–69. https://doi.org/10.1016/j.bios.2010.05.010.

Branner, A., R. B. Stein, and R. A. Normann. 2001. "Selective Stimulation of Cat Sciatic Nerve Using an Array of Varying-Length Microelectrodes." *Journal of Neurophysiology* 85 (4):1585–94.

Burke, R E. 1968. "Firing Patterns of Gastrocnemius Motor Units in the Decerebrate Cat." *Journal of Physiology* 196 (3):631–54.

Chiu, S Y, J M Ritchie, R B Rogart, and D Stagg. 1979. “A Quantitative Description of Membrane Currents in Rabbit Myelinated Nerve.” *The Journal of Physiology* 292 (1):149–66. https://doi.org/10.1113/jphysiol.1979.sp012843.

Clamann, H Peter, and Elwood Henneman. 1976. “Electrical Measurement of Axon Diameter and Its Use in Relating Motoneuron Size to Critical Firing Level.” *Journal of Neurophysiology* 39 (4):844–51.

Dhillon, Gurpreet Singh, and Kenneth W. Horch. 2005. “Direct Neural Sensory Feedback and Control of a Prosthetic Arm.” *IEEE Transactions on Neural Systems and Rehabilitation Engineering: A Publication of the IEEE Engineering in Medicine and Biology Society* 13 (4):468–72. https://doi.org/10.1109/TNSRE.2005.856072.

Edell, D. J. 1986. “A Peripheral Nerve Information Transducer for Amputees: Long-Term Multichannel Recordings from Rabbit Peripheral Nerves.” *IEEE Transactions on Biomedical Engineering* BME-33 (2):203–14. https://doi.org/10.1109/TBME.1986.325892.

Fischer, Hannah. 2010. “U.S. Military Casualty Statistics: Operation New Dawn, Operation Iraqi Freedom, and Operation Enduring Freedom.”

Fitzgerald, James J, Stéphanie P Lacour, Stephen McMahon, and James Fawcett. 2008. “Microchannels as Axonal Amplifiers.” *IEEE Transactions on Biomedical Engineering* 55 (3):1136–46.

Fitzgerald, James J, Natalia Lago, Samia Benmerah, Jordi Serra, Christopher P Watling, Ruth E Cameron, Edward Tarte, Stéphanie P Lacour, Stephen McMahon, and James W Fawcett. 2012. “A Regenerative Microchannel Neural Interface for Recording from and Stimulating Peripheral Axons in Vivo.” *Journal of Neural Engineering* 9 (1).

Fugleholm, Kåre, Henning Schmalbruch, and Christian Krarup. 2000. “Post Reinnervation Maturation of Myelinated Nerve Fibers in the Cat Tibial Nerve: Chronic Electrophysiological and Morphometric Studies,” June, 82–95.

Fuglevand, Andrew J., David A Winter, and Aftab E Patla. 1993. “Models of Recruitment and Rate Coding Organization in Motor-Unit Pools.” *Journal of Neurophysiology* 70 (6):2470–88.

Goodall, E. V., T. M. Lefurge, and K. W. Horch. 1991. “Information Contained in Sensory Nerve Recordings Made with Intrafascicular Electrodes.” *IEEE Transactions on Biomedical Engineering* 38 (9):846–50. https://doi.org/10.1109/10.83604.

Gore, Russell K, Yoonsu Choi, Ravi V Bellamkonda, and Arthur W English. 2015. “Functional Recordings from Awake, Behaving Rodents through a Microchannel Based Regenerative Neural Interface.” *Journal of Neural Engineering* 12 (1):016017.

Greenman, M. J. 1913. “Studies on the Regeneration of the Peroneal Nerve of the Albino Rat: Number and Sectional Areas of Fibers: Area Relation of Axis to Sheath.” *The Journal of Comparative Neurology* 23 (5):479–513. https://doi.org/10.1002/cne.900230503.

Grill, W.M., and J.T. Mortimer. 1995. “Stimulus Waveforms for Selective Neural Stimulation.” *IEEE Engineering in Medicine and Biology Magazine* 14 (4):375–85. https://doi.org/10.1109/51.395310.

Gutmann, E., and F. K. Sanders. 1943. “Recovery of Fibre Numbers and Diameters in the Regeneration of Peripheral Nerves.” *The Journal of Physiology* 101 (4):489–518.

Hassler, Christina, Tim Boretius, and Thomas Stieglitz. 2011. “Polymers for Neural Implants.” *Journal of Polymer Science Part B: Polymer Physics* 49 (1):18–33. https://doi.org/10.1002/polb.22169.

Henneman, Elwood. 1957. “Relation between Size of Neurons and Their Susceptibility to Discharge.” *Science* 126 (3287):1345–47.

Henneman, Elwood, George Somjen, and David O Carpenter. 1965a. “Excitability and Inhibitability of Motoneurons of Different Sizes.” *Journal of Neurophysiology* 28:599–620.

———. 1965b. “Functional Significance of Cell Size in Spinal Motoneurons.” *Journal of Neurophysiology* 28:560–80.

Hildebrand, C., J. D. Kocsis, S. Berglund, and S. G. Waxman. 1985. “Myelin Sheath Remodelling in Regenerated Rat Sciatic Nerve.” *Brain Research* 358 (1–2):163–70.

Hines, M L, and N T Carnevale. 1997. “The NEURON Simulation Environment.” *Neural Computation* 9:1179–1209.

Hiscoe, H. B. 1947. “Distribution of Nodes and Incisures in Normal and Regenerated Nerve Fibers.” *The Anatomical Record* 99 (4):447–75.

Hoffer, J. A., R. B. Stein, M. K. Haugland, T. Sinkjaer, W. K. Durfee, A. B. Schwartz, G. E. Loeb, and C. Kantor. 1996. “Neural Signals for Command Control and Feedback in Functional Neuromuscular Stimulation: A Review.” *Journal of Rehabilitation Research and Development* 33 (2):145–57.

Hossain, Ridwan, Bongkyun Kim, Rachel Pankratz, Ali Ajam, Sungreol Park, Sibani L Biswal, and Yoonsu Choi. 2015. “Handcrafted Multilayer PDMS Microchannel Scaffolds for Peripheral Nerve Regeneration.” *Biomedical Microdevices* 17 (6):109.

Jenq, C. -B., and R. E. Coggeshall. 1985. “Numbers of Regenerating Axons in Parent and Tributary Peripheral Nerves in the Rat.” *Brain Research* 326 (1):27–40. https://doi.org/10.1016/0006-8993(85)91381-2.

Kim, Bongkyun, Alejandro Reyes, Bernardo Garza, and Yoonsu Choi. 2015. “A Microchannel Neural Interface with Embedded Microwires Targeting the Peripheral Nervous System.” *Microsystem Technologies* 21 (7):1551–57.

Kovacs, G. T A, C.W. Storment, and J.M. Rosen. 1992. “Regeneration Microelectrode Array for Peripheral Nerve Recording and Stimulation.” *IEEE Transactions on Biomedical Engineering* 39 (9):893–902. https://doi.org/10.1109/10.256422.

Kuiken TA, Li G, Lock BA, and et al. 2009. “Targeted Muscle Reinnervation for Real-Time Myoelectric Control of Multifunction Artificial Arms.” *JAMA* 301 (6):619–28. https://doi.org/10.1001/jama.2009.116.

Lacour, Stéphanie P, Raghied Atta, James FitzGerald, Mark Blamire, Edward Tarte, and James Fawcett. 2008. “Polyimide Micro-Channel Arrays for Peripheral Nerve Regenerative Implants.” *Sensors and Actuators A: Physical* 147 (2):456–63.

Lacour, Stéphanie P., Samia Benmerah, Edward Tarte, James FitzGerald, Jordi Serra, Stephen McMahon, James Fawcett, Oliver Graudejus, Zhe Yu, and Barclay Morrison Iii. 2010. “Flexible and Stretchable Micro-Electrodes for in Vitro and in Vivo Neural Interfaces.” *Medical & Biological Engineering & Computing* 48 (10):945–54. https://doi.org/10.1007/s11517-010-0644-8.

Lacour, Stéphanie P, James J Fitzgerald, Natalia Lago, Edward Tarte, Stephen McMahon, and James Fawcett. 2009. “Long Micro-Channel Electrode Arrays: A Novel Type of Regenerative Peripheral Nerve Interface.” *IEEE Transactions on Neural Systems and Rehabilitation Engineering: A Publication of the IEEE Engineering in Medicine and Biology Society* 17 (5):454–60. https://doi.org/10.1109/TNSRE.2009.2031241.

Lago, Natalia, Dolores Ceballos, Francisco J Rodríguez, Thomas Stieglitz, and Xavier Navarro. 2005. “Long Term Assessment of Axonal Regeneration through Polyimide Regenerative Electrodes to Interface the Peripheral Nerve.” *Biomaterials* 26 (14):2021–31. https://doi.org/10.1016/j.biomaterials.2004.06.025.

Leuthardt, E. C, G. Schalk, J. R Wolpaw, J. G Ojemann, and D. W Moran. 2004. “A Brain–computer Interface Using Electrocorticographic Signals in Humans.” *Journal of Neural Engineering* 1:63.

MacEwan, Matthew R., Erik R. Zellmer, Jesse J. Wheeler, Harold Burton, and Daniel W. Moran. 2016. “Regenerated Sciatic Nerve Axons Stimulated through a Chronically Implanted Macro-Sieve Electrode.” *Frontiers in Neuroscience* 10. https://doi.org/10.3389/fnins.2016.00557.

Mannard, A., R. B. Stein, and D. Charles. 1974. “Regeneration Electrode Units: Implants for Recording from Single Peripheral Nerve Fibers in Freely Moving Animals.” *Science (New York, N.Y.)* 183 (4124):547–49.

Marks, A F. 1969. “Bullfrog Nerve Regeneration into Porous Implants.” *Anatom. Rec.* 163:226.

McQuarrie, I G. 1985. “Effect of Conditioning Lesion on Axonal Sprout Formation at Nodes of Ranvier.” *The Journal of Comparative Neurology* 231 (2):239–49. https://doi.org/10.1002/cne.902310211.

Micera, Silvestro, Xavier Navarro, Jacopo Carpaneto, Luca Citi, Oliver Tonet, Paolo Maria Rossini, Maria Chiara Carrozza, et al. 2008. “On the Use of Longitudinal Intrafascicular Peripheral Interfaces for the Control of Cybernetic Hand Prostheses in Amputees.” *IEEE Transactions on Neural Systems and Rehabilitation Engineering* 16 (5):453–72.

Micera, Silvestro, Paolo M Rossini, Jacopo Rigosa, Luca Citi, Jacopo Carpaneto, Stanisa Raspopovic, Mario Tombini, et al. 2011. “Decoding of Grasping Information from Neural Signals Recorded Using Peripheral Intrafascicular Interfaces.” *Journal of NeuroEngineering and Rehabilitation* 8 (September):53. https://doi.org/10.1186/1743-0003-8-53.

Miller, Laura A., Robert D. Lipschutz, Kathy A. Stubblefield, Blair A. Lock, He Huang, T. Walley Williams, Richard F. Weir, and Todd A. Kuiken. 2008. “Control of a Six Degree of Freedom Prosthetic Arm after Targeted Muscle Reinnervation Surgery.” *Archives of Physical Medicine and Rehabilitation* 89 (11):2057–65. https://doi.org/10.1016/j.apmr.2008.05.016.

Minev, Ivan R, Daniel J Chew, Evangelos Delivopoulos, James Fawcett, and Stéphanie P Lacour. 2012. “High Sensitivity Recording of Afferent Nerve Activity Using Ultra-Compliant Microchannel Electrodes: An Acute in Vivo Validation.” *Journal of Neural Engineering* 9 (2).

Naples, G.G., J.T. Mortimer, A. Scheiner, and J.D. Sweeney. 1988. “A Spiral Nerve Cuff Electrode for Peripheral Nerve Stimulation.” *IEEE Transactions on Biomedical Engineering* 35 (11):905–16. https://doi.org/10.1109/10.8670.

Navarro, Xavier, Thilo B. Krueger, Natalia Lago, Silvestro Micera, Thomas Stieglitz, and Paolo Dario. 2005. “A Critical Review of Interfaces with the Peripheral Nervous System for the Control of Neuroprostheses and Hybrid Bionic Systems.” *Journal of the Peripheral Nervous System: JPNS* 10 (3):229–58. https://doi.org/10.1111/j.1085-9489.2005.10303.x.

Nicolas-Alonso, Luis Fernando, and Jaime Gomez-Gil. 2012. “Brain Computer Interfaces, a Review.” *Sensors (Basel, Switzerland)* 12 (2):1211–79. https://doi.org/10.3390/s120201211.

Pet, Mitchell A., Jason H. Ko, Janna L. Friedly, Pierre D. Mourad, and Douglas G. Smith. 2014. “Does Targeted Nerve Implantation Reduce Neuroma Pain in Amputees?” *Clinical Orthopaedics and Related Research* 472 (10):2991–3001. https://doi.org/10.1007/s11999-014-3602-1.

Poppler, Louis H, Xueping Ee, Lauren Schellhardt, Gwendolyn M Hoben, Deng Pan, Daniel A. Hunter, Ying Yan, et al. 2016. “Axonal Growth Arrests After an Increased Accumulation of Schwann Cells Expressing Senescence Markers and Stromal Cells in Acellular Nerve Allografts.” *Tissue Engineering: Part B* 22 (13–14):949–61.

Raspopovic, Stanisa, Marco Capogrosso, Francesco Maria Petrini, Marco Bonizzato, Jacopo Rigosa, Giovanni Di Pino, Jacopo Carpaneto, et al. 2014. “Restoring Natural Sensory Feedback in Real-Time Bidirectional Hand Prostheses.” *Science Translational Medicine* 6 (222):222ra19–222ra19.

Rosen, J. M., M. Grosser, and V. R. Hentz. 1990. “Preliminary Experiments in Nerve Regeneration through Laser-Drilled Holes in Silicon Chips.” *Restorative Neurology and Neuroscience* 2 (2):89–102. https://doi.org/10.3233/RNN-1990-2205.

Rouse, A. G, and D. W Moran. 2009. “Neural Adaptation of Epidural Electrocorticographic (EECoG) Signals during Closed-Loop Brain Computer Interface (BCI) Tasks.” *Conf Proc IEEE Eng Med Biol Soc* 2009:5514–17.

Saheb-Al-Zamani, Maryam, Ying Yan, Scott J. Farber, Daniel A. Hunter, Piyaraj Newton, Matthew D. Wood, Sheila A. Stewart, Philip J. Johnson, and Susan E. Mackinnon. 2013. “Limited Regeneration in Long Acellular Nerve Allografts Is Associated with Increased Schwann Cell Senescence.” *Experimental Neurology*, no. 247 (September):165–77.

Sanders, F. K., and D. Whitteridge. 1946. “Conduction Velocity and Myelin Thickness in Regenerating Nerve Fibres.” *The Journal of Physiology* 105 (2):152–74.

Sivolella, Stefano, Giulia Brunello, Nadia Ferrarese, Alessandro Della Puppa, Domenico D’Avella, Eriberto Bressan, and Barbara Zavan. 2014. “Nanostructured Guidance for Peripheral Nerve Injuries: A Review with a Perspective in the Oral and Maxillofacial Area.” *International Journal of Molecular Sciences* 15 (2):3088–3117. https://doi.org/10.3390/ijms15023088.

Srinivasan, Akhil, Liang Guo, and Ravi V Bellamkonda. 2011. “Regenerative Microchannel Electrode Array for Peripheral Nerve Interfacing.” *Proceedings of the 5th International IEEE EMBS Conference on Neural Engineering*, May, 253–56.

Srinivasan, Akhil, Mayank Tahilramani, John T Bentley, Russell K Gore, Daniel C Millard, Vivek J Mukhatyar, Anish Joseph, et al. 2015. “Microchannel-Based Regenerative Scaffold for Chronic Peripheral Nerve Interfacing in Amputees.” *Biomaterials* 41 (February):151–65.

Stieglitz, T., X. Navarro, S. Calvet, C. Blau, and J.-U. Meyer. 1996. “Interfacing Regenerating Peripheral Nerves with a Micromachined Polyimide Sieve Electrode.” In *Proceedings of the 18th Annual International Conference of the IEEE Engineering in Medicine and Biology Society, 1996. Bridging Disciplines for Biomedicine*, 1:365–66 vol.1. https://doi.org/10.1109/IEMBS.1996.656995.

Suzuki, T., N. Kotake, K. Mabuchi, and S. Takeuchi. 2006. “Flexible Regeneration-Type Nerve Electrode with Integrated Microfluidic Channels.” In *2006 International Conference on Microtechnologies in Medicine and Biology*, 303–5. https://doi.org/10.1109/MMB.2006.251557.

Sweeney, J. D., K. Deng, E. Warman, and J. T. Mortimer. 1989. “Modeling of Electric Field Effects on the Excitability of Myelinated Motor Nerve.” In *Engineering in Medicine and Biology Society, 1989. Images of the Twenty-First Century., Proceedings of the Annual International Conference of the IEEE Engineering In*, 1281–82 vol.4. https://doi.org/10.1109/IEMBS.1989.96194.

Taylor, D. M., S. I. Tillery, and A. B. Schwartz. 2002. “Direct Cortical Control of 3D Neuroprosthetic Devices.” *Science* 296 (5574):1829–32.

Tyler, Dustin J., and Dominique M. Durand. 2002. “Functionally Selective Peripheral Nerve Stimulation with a Flat Interface Nerve Electrode.” *IEEE Transactions on Neural Systems and Rehabilitation Engineering: A Publication of the IEEE Engineering in Medicine and Biology Society* 10 (4):294–303. https://doi.org/10.1109/TNSRE.2002.806840.

Veraart, C., W. M. Grill, and J. T. Mortimer. 1993. “Selective Control of Muscle Activation with a Multipolar Nerve Cuff Electrode.” *IEEE Transactions on Bio-Medical Engineering* 40 (7):640–53. https://doi.org/10.1109/10.237694.

Vizoso, A. D., and J. Z. Young. 1948. “Internode Length and Fibre Diameter in Developing and Regenerating Nerves.” *Journal of Anatomy* 82 (Pt 1-2):110–134.1.

Williams, J. C, J. A Hippensteel, J. Dilgen, W. Shain, and D. R Kipke. 2007. “Complex Impedance Spectroscopy for Monitoring Tissue Responses to Inserted Neural Implants.” *Journal of Neural Engineering* 4:410.

Wodlinger, B., J. E. Downey, E. C. Tyler-Kabara, A. B. Schwartz, M. L. Boninger, and J. L. Collinger. 2015. “Ten-Dimensional Anthropomorphic Arm Control in a Human Brain-Machine Interface: Difficulties, Solutions, and Limitations.” *Journal of Neural Engineering* 12 (1):016011. https://doi.org/10.1088/1741-2560/12/1/016011.

Wodlinger, Brian, and Dominique M Durand. 2009. “Localization and Recovery of Peripheral Neural Sources With Beamforming Algorithms.” *IEEE Transactions on Neural Systems and Rehabilitation Engineering* 17 (5):461–68.

Wood, Matthew D., Amy M. Moore, Daniel A. Hunter, Sami Tuffaha, Gregory H. Borschel, Susan E. Mackinnon, and Shelly E. Sakiyama-Elbert. 2009. “Affinity-Based Release of Glial-Derived Neurotrophic Factor from Fibrin Matrices Enhances Sciatic Nerve Regeneration.” *Acta Biomaterialia* 5 (4):959–68. https://doi.org/10.1016/j.actbio.2008.11.008.

Wu, J., and D. T. Chiu. 1999. “Painful Neuromas: A Review of Treatment Modalities.” *Annals of Plastic Surgery* 43 (6):661–67.

Yoshida, K., K. Hennings, and S. Kammer. 2006. “Acute Performance of the Thin-Film Longitudinal Intra-Fascicular Electrode.” In *The First IEEE/RAS-EMBS International Conference on Biomedical Robotics and Biomechatronics, 2006. BioRob 2006.*, 296–300. https://doi.org/10.1109/BIOROB.2006.1639102.

Zellmer, Erik, Matthew MacEwan, and Daniel Moran. 2017. “Modelling the Impact of Altered Axonal Morphometry on the Response of Regenerative Nervous Tissue to Electrical Stimulation through Macro-Sieve Electrodes.” *Journal of Neural Engineering*.

Zhao, Q., J. Drott, T. Laurell, L. Wallman, K. Lindström, L. M. Bjursten, G. Lundborg, L. Montelius, and N. Danielsen. 1997. “Rat Sciatic Nerve Regeneration through a Micromachined Silicon Chip.” *Biomaterials* 18 (1):75–80.

Ziegler-Graham, Kathryn, Ellen J. MacKenzie, Patti L. Ephraim, Thomas G. Travison, and Ron Brookmeyer. 2008. “Estimating the Prevalence of Limb Loss in the United States: 2005 to 2050.” *Archives of Physical Medicine and Rehabilitation* 89 (3):422–29. https://doi.org/10.1016/j.apmr.2007.11.005.

Chapter 4: Stimulation and Bi-Directional Performance

4.1 Introduction

Loss of limb represents one of the most traumatic injuries and yet happens to nearly 200,000 people in the United States every year (Ziegler-Graham *et al.* 2008). In particular, loss of a hand makes many activities of daily living (ADLs) much more difficult, if not impossible, as many require coordinated effort of both hands. Much work has been put into developing motorized prosthetics (i-Limb, DEKA hand, and JPL etc.) to alleviate this loss (Loucks *et al.* 1987; Resnik, Klinger, and Etter 2014; Cordella *et al.* 2016). However, a major problem identified by individuals utilizing prosthetic limbs is poor integration of the limb with the whole person due to inadequate motor control and lack of sensory feedback (Cordella *et al.* 2016).

Our intact limbs provide haptic feedback, the sense of touch including proprioception that lets us know the location, orientation and speed of our limbs. However, until quite recently the patient had to rely on visual feedback or in some cases feedback through a different surface area of their body (Kuiken *et al.* 2007) to sense the location of a prosthetic limb. This poses a severe limitation to use of the device (Biddis and Chau 2007; Childress 1980). For example, in limb control where only visual feedback was available, a person would not be able to feel the position of her arm or how much force it was exerting, which would make ADLs such as drinking coffee or picking up a tomato difficult. In short, without information such as grasping pressure, activities of daily living are quite challenging (Ziegler-Graham *et al.* 2008). Further, the patient must pay visual attention to the hand, imposing limits on how it can be used.

With an artificial limb, the same kinds of options exist for haptic feedback as for decoding a subjects intention to move: direct brain computer interface (BCI) to sensory cortex with the required invasive surgery and problems with longevity of the device due to the foreign body response encapsulating the electrodes (Bjornsson *et al.* 2006; Williams *et al.* 2007); stimulating another surface area of the body with the possibility of rerouting sensory nerves to that area to avoid translation problems (Kuiken *et al.* 2007) with the drawback of an invasive surgery and difficulty of both recording the user's intention simultaneous with providing sensory feedback; and the use of peripheral neural interfaces (PNIs).

PNIs were used in a recent study by Raspopovic and colleagues to provide tactile feedback from a prosthetic hand to an amputee through thin-film transverse intra-fascicular electrodes (tfTIMEs or TIMEs). The natural sensory feedback to the user enabled him to have excellent control of the device's grip strength by somatosensation alone as well as to discriminate the shape of objects solely through the prosthetic hand (Raspopovic *et al.* 2014). The control of the hand, however, was not through the natural path of the peripheral nervous system, but through electromyogram (EMG) signals from the upper arm. Other studies have also shown the ability to generate graded touch and hand position sensations via stimulating the peripheral nerves (G.S. Dhillon and Horch 2005; Horch *et al.* 2011)). Further, from the Raspopovic study, it is clear that the patient can actually use sensory feedback in a functionally relevant manner. This alleviates an initial concern that peripheral nerves might degrade after limb loss or the central nervous system might use the cortical areas originally used for the limb for other purposes. In actuality, peripheral stump axons can be recorded and decoded to identify motor commands as well as stimulated to induce perceived sensation in a lost limb years after the limb loss (Dhillon *et al.* 2004).

It would seem ideal, then, to use PNIs both to provide sensation by stimulating sensory axons within the peripheral nerve while simultaneously recording signals from motor axons and decoding them to determine the patient's intended motion (Figure 4-1). Although several types of PNIs are considered bi-directional (Micera *et al.* 2008; Micera and Navarro 2009; Yoshida *et al.* 2000; Boretius *et al.* 2010), none can concurrently do both operations simultaneously. The reason for this is that the current required to stimulate sensory axons creates large voltages (i.e. stimulation artifact) at the recording sites that are several orders of magnitude greater than the electroneurograms (ENGs) used for control. Further, the stimulus artifact not only corrupts the desired signal, but can also cause the recording amplifiers to saturate and "ring" for a long time after the stimulus is gone (Loi *et al.* 2011). A common technique to try to mitigate this problem is to short the amplifier inputs for a brief window (8 ms) during and immediately after a stimulation pulse (Cozzi *et al.* 2005). This type of interlacing has the obvious drawback that you cannot record ENGs during the time period that the amplifier inputs are shunted.

Micro-channel PNIs may avoid this problem. Traditionally, sieve PNIs are a flat disk with many holes which, after being placed in between the transected ends of a peripheral nerve, spread out axons as they grow back (or regenerate) through the device (Marks 1969, 19; Mannard, Stein, and Charles 1974; Akin *et al.* 1994; Stieglitz *et al.* 1996; Navarro *et al.* 2005). Optimization of this device family has focused on using a more flexible material to match the stiffness of the neural substrate (Navarro *et al.* 2005) as well as experimentation with hole sizes and overall device transparency (Lago *et al.* 2007; MacEwan *et al.* 2016). Unlike traditional sieve electrodes, the pores through micro channel PNIs (Suzuki *et al.* 2006; Fitzgerald *et al.* 2008) are significantly longer which minimizes cross-talk between recording electrodes according to observations by Kim and collegues (Kim *et al.* 2015). This indirectly points to the potential for this device type to

minimize artifact from a stimulating electrode to a recording one - a necessity for having a simultaneous, bi-directional PNI.

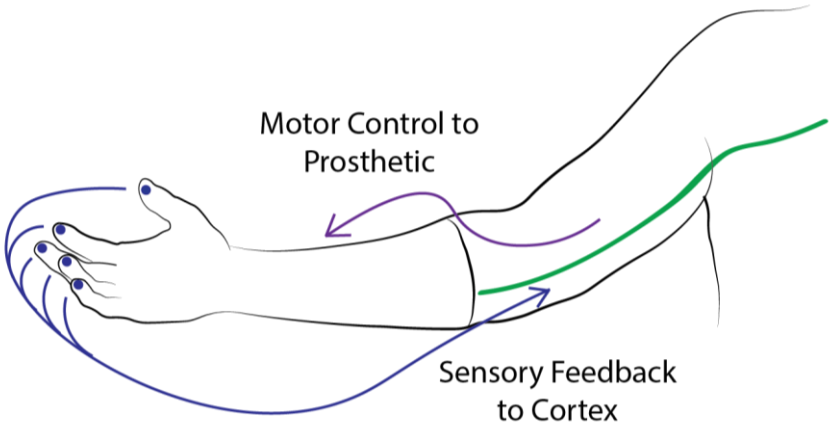

Figure 4-1. Goal of bi-directional peripheral neural interface for prosthetic limbs. Motor axons are recorded to control the prosthetic while sensors in the prosthetic drive stimulation of sensory axons to create artificial perception

A companion paper documents the expected electroneurogram (ENG) potentials during axonal recordings using micro-channel and tfTIME devices. This paper completes the bi-directional performance comparison by determining for both device types the required stimulation current to induce sensation and the stimulation artifact in neighboring electrodes for each device type. For micro-channels, multi-polar stimulation is also assessed. Combining the ENG results from the companion document with the results of this paper, the signal-to-artifact ratio for both device types are computed. Further, it is shown how to optimize the micro-channels design in terms of geometry, electrode configuration and placement, to maximize signal-to-artifact ratio. Together, these papers demonstrate the considerable performance advantage of the micro-channel design for a simultaneous bi-directional neural interface compared to the commonly used tfTIME electrode.

4.2 Methods

The computational modeling process (Figure 4-2) is briefly summarized here with details of the individual components explained in the subsequent sections.

Computational modeling was used to determine the stimulation current amplitudes required to elicit activation of interfaced axons using the TIME and micro-channel sieve interfaces along with the accompanying stimulation artifact at other device contacts or adjacent micro-channels respectively. The device geometry for each device was modeled in COMSOL multiphysics (V.4.3, COMSOL AB), which uses the finite element method to determine voltage profiles along the length of model axons simulated in NEURON (V. 7.1, Hines and Carnevale 1997). These voltage profiles as well as the artifact at nearby electrodes on the same device were computed based on a reference stimulation current of 1 μA. Mammalian axon models implemented in NEURON (CRRSS nodal dynamics) (Chiu *et al.* 1979; Sweeney *et al.* 1989) representing regenerated and normal axons (Zellmer, MacEwan, and Moran 2017) were used to determine the electrophysiological response of axons in a given radius around the TIME electrode or within the channel of the micro-channel device. The threshold of stimulation current to generate an action potential was determined for each axon being modeled and was used to construct recruitment curves describing the fraction of interfaced axons activated at a given stimulation amplitude. The threshold stimulation was further used to provide a scale factor for the stimulation artifact at the reference stimulation current to generate the actual stimulation artifact.

4.2.1 Finite element model of devices

Finite element (FE) models were developed in COMSOL for both tfTIME and micro-channel devices to evaluate the stimulation artifact at nearby electrodes for each device type and across variations in micro-channel geometry.

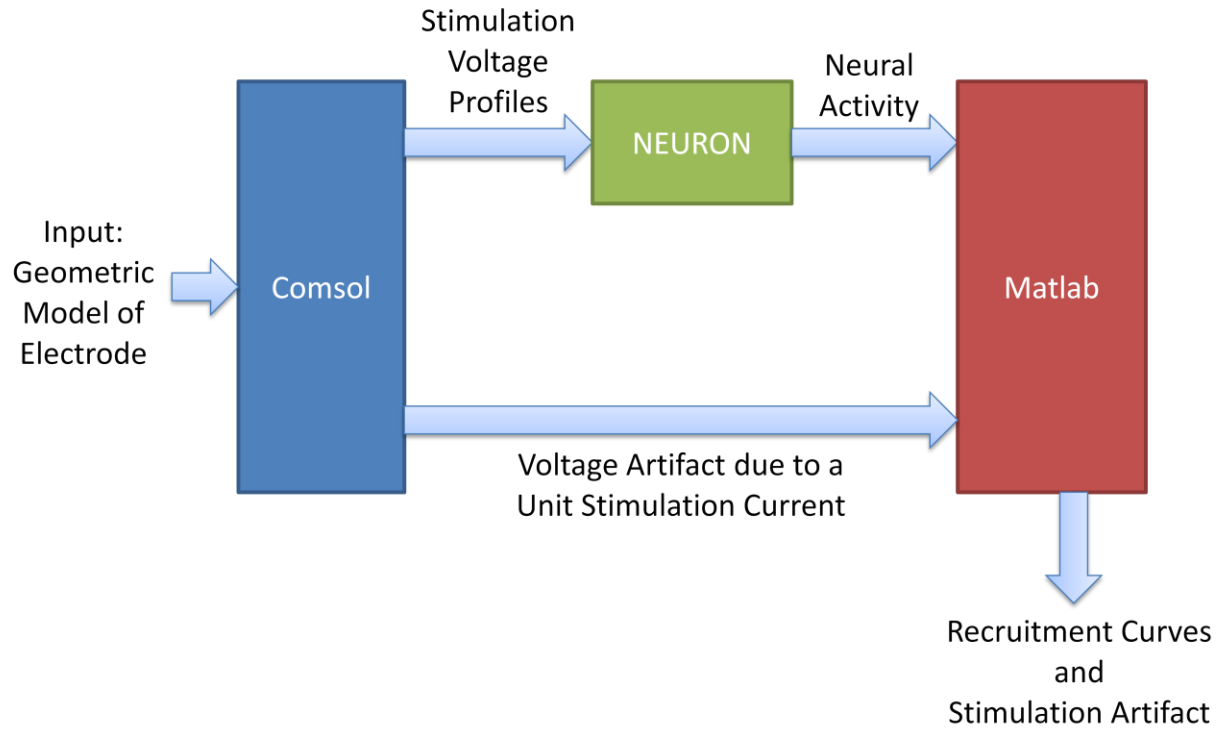

Figure 4-2. Overview of stimulation model. A geometric model of each type of device was created. The Electrical potential throughout the model space due to a reference stimulation current (1 µA) from the stimulating electrode (Comsol) was determined. This was used both to determine the minimum stimulation current for axons around/through the device to start firing (NEURON) as well as what the stimulation artifact due to the reference current would be. Matlab processed the Neuron output to generate the actual recruitment curve and scale the stimulation artifacts by the minimum stimulation current.

The reference design for the TIME (Figure 4-3A) was adopted using the design described in the work of Boretius *et al.* (2010) which was cited as the electrode design used in Raspopovic's 2014 study showing successful use of sensory feedback in a prosthetic hand. The device is symmetric and is folded at the mid-point to create a 2-sided device though only one side is shown in Figure 4-3A. Device and electrode sizes as well as the spacing between electrodes sites and the ground

surface were preserved. Boretius' design did not have all of the electrodes centered in the proximal-distal axis. Instead, they were staggered along that axis which appeared to be primarily for the purpose of easing the routing of the traces connecting the electrode sites to the electrical connector at the edge of the device. Our model was simplified to keep the electrodes centered in the proximal-distal axis instead of staggered. There are a few reasons for this. First, the amount of staggering is unknown, though it could be approximated by examining the diagram in Boretius *et al.* (2010). Second, the purpose of the staggering seemed to be primarily for ease in routing the traces to the electrodes (i.e. design/manufacturing concerns), not for any electrophysiological reason. Third, it will only have a minor effect on electrophysiological results since the difference in inter-electrode separation between Boretius' actual device and our model will be quite small since the magnitude of the staggering was small compared to the lateral distance between the electrode sites. Compounding this, the conductivity is greater in the distal-proximal axis meaning the signal will propagate more freely in that direction. This further lessens the effect due to the offset compared to a change in the lateral dimension. Finally, a recent paper from the same group investigating the selectivity of TIME devices did not have them staggered. Instead, they were all centered in the proximal-distance axis as modeled herein (Badia *et al.* 2016).

The micro-channel geometry implemented by Lacour and colleagues (Lacour *et al.* 2010), rather than the simplified design the same group computationally modeled (Fitzgerald *et al.* 2008), was used as the basis for our geometric design (see Figure 4-3B - 4-3D). This design employs channels with a square cross-section extruded out to the desired length. The channel width was varied from 90 µm to 240 µm in 30 µm increments, maintaining a square opening. The lower bound was chosen based on the size (<100 µm in width) under which Lacour and colleagues

found poor axonal regeneration (Lacour et al. 2009). Srinivasan *et al.* reported similar results finding that channel cross-sections 100 x 100 µm or larger have better regeneration than smaller channels (Srinivasan *et al.* 2015). Channel lengths of 2, 3, 4, 5 and 9 mm were used. The lower bound of this range was chosen to be short enough that little advantage would be gained from the presence of a micro-channel. The upper bound was the length where adequate axonal regeneration would be unlikely (9 mm) without adjuncts used to improve regeneration such as neurotrophic factors (Wood *et al.* 2009). For comparison, 3 cm is the longest regeneration current achievable by acellular nerve allografts (Saheb-Al-Zamani *et al.* 2013; Poppler *et al.* 2016). For a 180 µm channel width, the wall thickness was 20 µm. The ratio of channel width to wall thickness (or aspect ratio) was kept constant as channel width was varied.

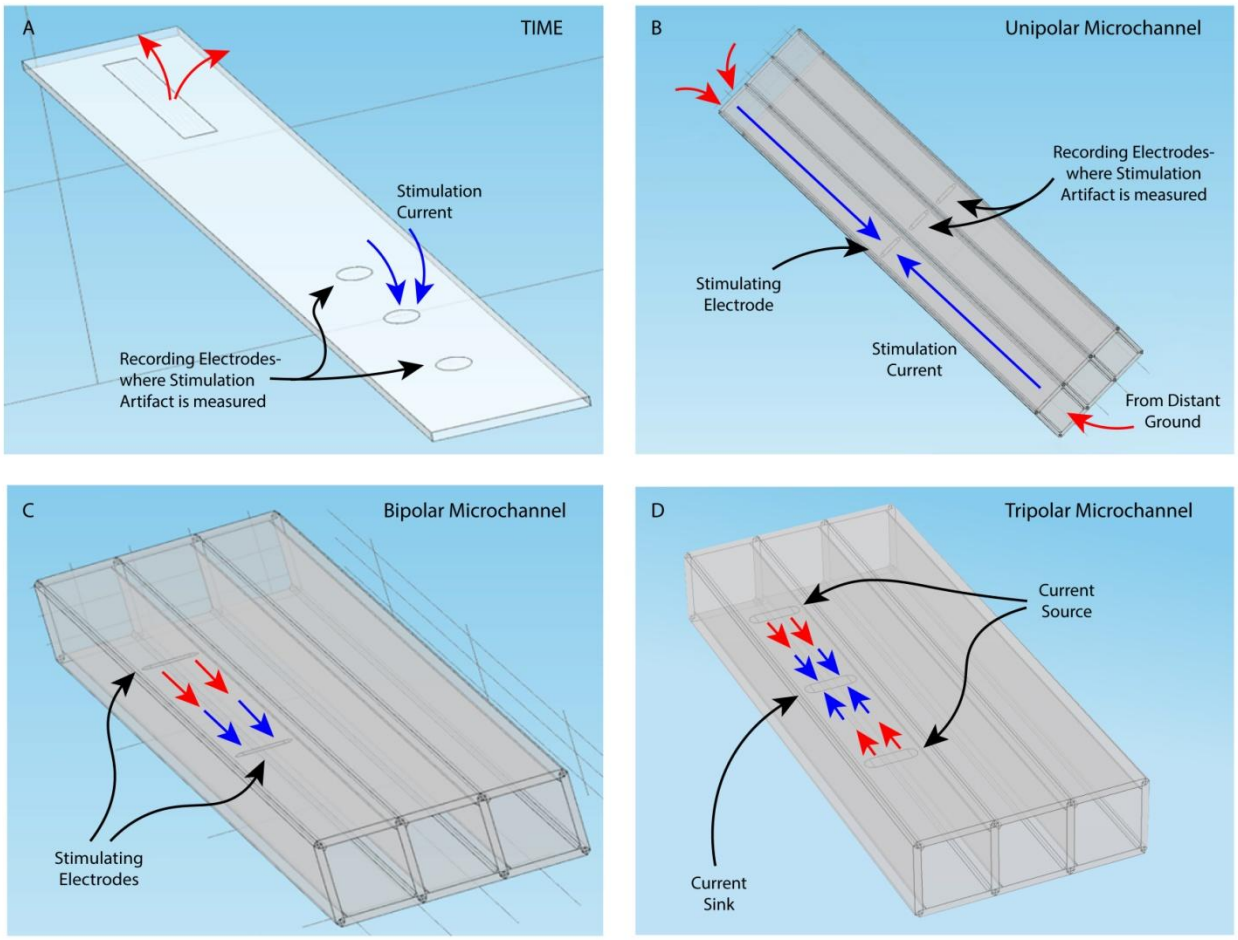

Figure 4-3. Comsol models of tfTime (A) and unipolar (B), bipolar (C) and tripolar (D) micro-channel configurations. One channel is chosen for stimulation while the other channels are used for recording. The micro-channel device provides a greater electrical impedance to extra-cellular space resulting in larger voltage signals as well as shielding adjacent channels. In the bipolar and tripolar micro-channel configurations, current is balanced by being sunk at one electrode and sourced by one (bipolar) to two (tripolar) electrodes, minimizing the stimulation current that escapes the channel.

Each geometry was placed in a 2 mm diameter cylinder representing a peripheral nerve. For reference, this is slightly larger than the rat sciatic nerve. Neural tissue was modeled with an anisotropic conductivity (Zellmer, MacEwan, and Moran 2017) while the devices were modeled as perfect insulators. The boundary of the peripheral nerve was considered to be at ground potential for two reasons. First, the device electrodes are not close to the edge of the nerve, so the boundary of the nerve is already a moderately distant ground. Second, the saline surrounding

the nerve is an excellent volume conductor and readily disperses the small current flows out of the device.

4.2.2 Stimulation voltage profiles

To determine the stimulation threshold of an axon traveling through or around the PNI, we first determined the extracellular voltage profile along the length of the axon due to a reference stimulation. This profile was then linearly scaled to simulate the application of a given stimulation amplitude. To this end, normal current density sufficient to generate a 1 μA reference current was applied to the face of the stimulation electrode for both geometries. The current density is computed as total current (or 1 μA) divided by the surface area of the contact. For simplicity, the sides of the electrode were not treated as the source of stimulation current. Though they, in fact, have a finite width (typically less than 100 nm), the surface area of the side of the electrode compared to the face in an actual device is negligible. Furthermore, for the size of geometries under consideration, the electrode could likely have been modeled as a point-source with little difference in results.

For the micro-channel devices, 10 μm x 10 μm grids were created across the channel cross-section while maintaining a minimum of 5 μm distance from the channel wall. These represented potential axon locations and were extended longitudinally through the 16 mm length of the modeled nerve trunk. Due to the side-side symmetry of the device, voltage profiles were only determined for one side of the channel to reduce computation time. Additionally, the voltage profiles along the center of the top surface (the channel surface with the electrode) of the channel of interest as well as the next 2 adjacent channels were computed in order to determine stimulation artifacts. In all cases, the longitudinal resolution was 10 μm, providing 1600

samples along the length of each axon. A similar grid 10 µm x 10 µm was used for the tfTIME device, starting 9 µm normal to the surface and limiting the locations to various radii (50, 100, 200, and 250 µm) from the stimulating electrode. Using different radii gives a sense of the selectivity of the device. In both tfTIME and micro-channels, a distance of 5 - 10 µm was kept between the device and the closest axon since frequently a thin layer of connective tissue grows around the device (e.g. micro-fascicularization). As with the micro-channel devices, in addition to computing the voltage profiles along the length of axon locations, voltage profiles were computed along the surface of the other electrodes on the device in order to compute stimulation artifacts at other electrode sites used for simultaneous recording.

4.2.3 Multipolar stimulation

In order to investigate bipolar stimulation, the finite element model of the micro-channel device was modified to include two electrodes, equidistant from channel center, with one a current source and the other a current sink. The distance of the electrodes from channel center was moved in 5% increments of the total distance to the edge of the channel. Similar modifications were made for evaluating tripolar stimulation, for which the center electrode is a current sink while each of the outer electrodes source current at half the magnitude. As in the bipolar case, the outer electrodes were moveable in 5% increments of the distance from channel center to channel edge.

Voltage profiles were computed on the same grid and along the top-center of the two adjacent micro-channels as in the simulations of unipolar micro-channel stimulation.

4.2.4 Computing neural response to stimulation current

A core conductor axon model (CRRSS model) (Chiu *et al.* 1979; Sweeney *et al.* 1989) implemented in NEURON was used to determine the response of interfaced mammalian axons to the voltage profiles determined from Finite Element Modeling. Different morphometric properties were assigned to axons interfaced by the two interfaces to account for morphometric differences in normal, undamaged axons and those that have suffered trauma such as being crushed or even severed (Greenman 1913) as in the case of using a regenerative PNI. After such a trauma, axonal degeneration occurs both distally and proximally to the injury (McQuarrie 1985). As crushed axons regenerate, they eventually grow back to their normal diameter (Gutmann and Sanders 1943; Hildebrand *et al.* 1985; Fugleholm, Schmalbruch, and Krarup 2000). But severing a nerve results in permanent changes including reduced axon size distal to the injury, modified myelin thickness to axon diameter ratio (Gutmann and Sanders 1943), reduced conduction velocity (Sanders and Whitteridge 1946), and a change in the distance between successive nodes of Ranvier (Hiscoe 1947; Vizoso and Young 1948). The latter modification is particularly important to micro-channel devices. In normal axons, internode distance (distance between nodes of Ranvier) increases with axon diameter. However, for regenerated axons, this is shortened and internodal distance is constant across axonal diameters (Beuche and Friede 1985). As a result, even for micro-channels as short as 1 mm, multiple nodes of Ranvier will be present inside the micro-channel.

To account for these changes, the morphometric differences between normal and regenerated axons were included in the computational model. Specifically, for determining the neural response to a TIME device, morphometry representing normal axons were used in which the internodal distance varied with the axon diameter while morphometry representative for

regenerated axons (Zellmer, MacEwan, and Moran 2017) were used for the micro-channel devices.

Model axons were positioned on the grid of computed stimulation voltage profiles with the center node of Ranvier directly above (or below) the stimulating electrode. The computed voltage profiles were applied as the extracellular potential to the axons for 200 μs to simulate the applied stimulus (and 0 at all other times). Models were integrated using implicit Euler integration, for a simulation time of 5 ms and an integration time step of 0.01 ms. Data was recorded at each time slice (10 μs) to determine if an action potential occurred during the application of a stimulus of a given amplitude. Using an iterative method, the minimum stimulation current (or stimulation threshold) was determined to the nearest 0.01 μA.

This process was repeated with the Node of Ranvier offset in the proximal-distal axis by 5% increments up to 50% of the internodal distance. The stimulation thresholds for each axon grid position at the 11 different nodal staggering values were used to generate the expected stimulation currents given random nodal placements for 50% and 100% recruitment. Trials were conducted (N=1024) where the staggering for each axon grid position was randomly chosen as one of the 11 staggering values. The corresponding threshold stimulations for each axon was used to form a recruitment curve. The median and maximum stimulation thresholds were taken as the 50% and 100% recruitment thresholds for that trial. The mean and standard deviation were then taken from the 1024 trials for both thresholds (50% and 100%).

4.2.5 Computation of stimulation artifact

The stimulation artifact for each device is determined by multiplying the current required for stimulation by the voltage profile due to the reference current. The electrical potential at the site

of the adjacent recording site(s) is the expected stimulation artifact. Stimulation artifacts were computed for both tfTIME device and micro-channel devices at 50% recruitment. It is worthwhile noting that comparing at the 50% recruitment level favors the TIME device since the 50% and 100% recruitment thresholds are quite different for TIMEs, but nearly the same for micro-channels.

4.3 Results

4.3.1 Comparison of electrical potentials in unipolar devices

The electrical potential was computed along lines (or traces) running perpendicular to the tfTIME device, i.e. the same orientation to that of axons within the interfaced nerve (See Figure 4-4). For the purpose of determining stimulation artifact, potential traces were computed directly over each other electrode on the device. This includes the opposite side of the device, since it is folded over and thus has symmetric contacts on both sides (Figure 4-4). Additionally, the electrical potential was computed for traces passing through a 10 μm grid surrounding the device to determine axonal recruitment. For the stimulation artifact, there is a deep null at the contact directly opposite the stimulating electrode since the device itself presents a high impedance barrier to current flow. The null is also apparent at the other contacts on the opposite side of the device, though not as pronounced (Figure 4-4). It is worth noting the large drop in potential from the stimulating contact (70 mV) to the contact with the highest stimulus artifact (3.5 mV). This represents a 20:1 ratio or a 26 dB drop.

Similar to the TIME analysis, the electrical potential was determined for micro-channel devices along lines running the length of the channels at the surface of the device with the electrical contacts (Figure 4-5) shows the example of a 4 mm long, 120 μm wide device). Again, these

lines are parallel to the path that axons would take in an *in-vivo* context. This process was performed for all combinations of channel lengths and widths to find the voltage in the adjacent micro-channel at the channel contact. The worst-case (highest) stimulus artifact due to a 1 µA reference current is 1.9 mV which is lower than for the TIME device, but not dramatically. However, the desired stimulation voltage within the channel is considerably higher (170 mV) suggesting that a lower stimulation current may be required to elicit a response in the interfaced tissue. Specifically, since the stimulation current represents a scale factor for the stimulation artifact, the difference in stimulation artifact is magnified by the difference in the stimulation current required for axonal recruitment. The voltage ratio from the stimulating channel to adjacent channel for this geometry is 90:1 or 39 dB of inter-channel separation.

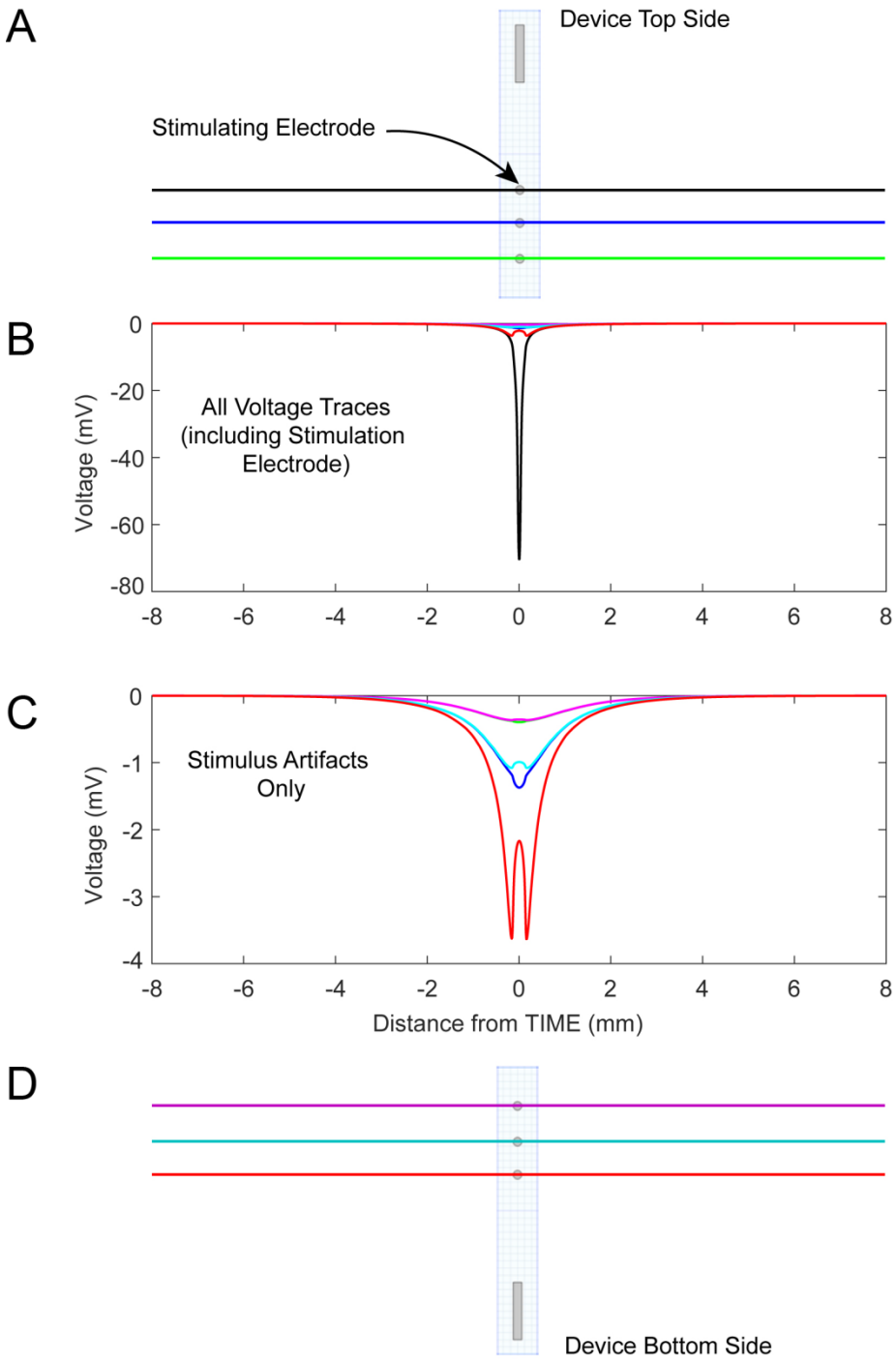

Figure 4-4. Stimulation voltage artifact resulting from unipolar stimulation through a single TIME electrode using a 1 μA reference current. **A:** Top surface of device with stimulating electrode and 2 recording electrodes. **D:** Bottom surface of device with 3 recording electrodes. **B-C:** Voltage at the surface of axons running perpendicular to the device's electrodes with stimulation electrode removed (**C**) to provide greater resolution. Colors of traces in voltage plots match colors of axons in top and bottom plots.

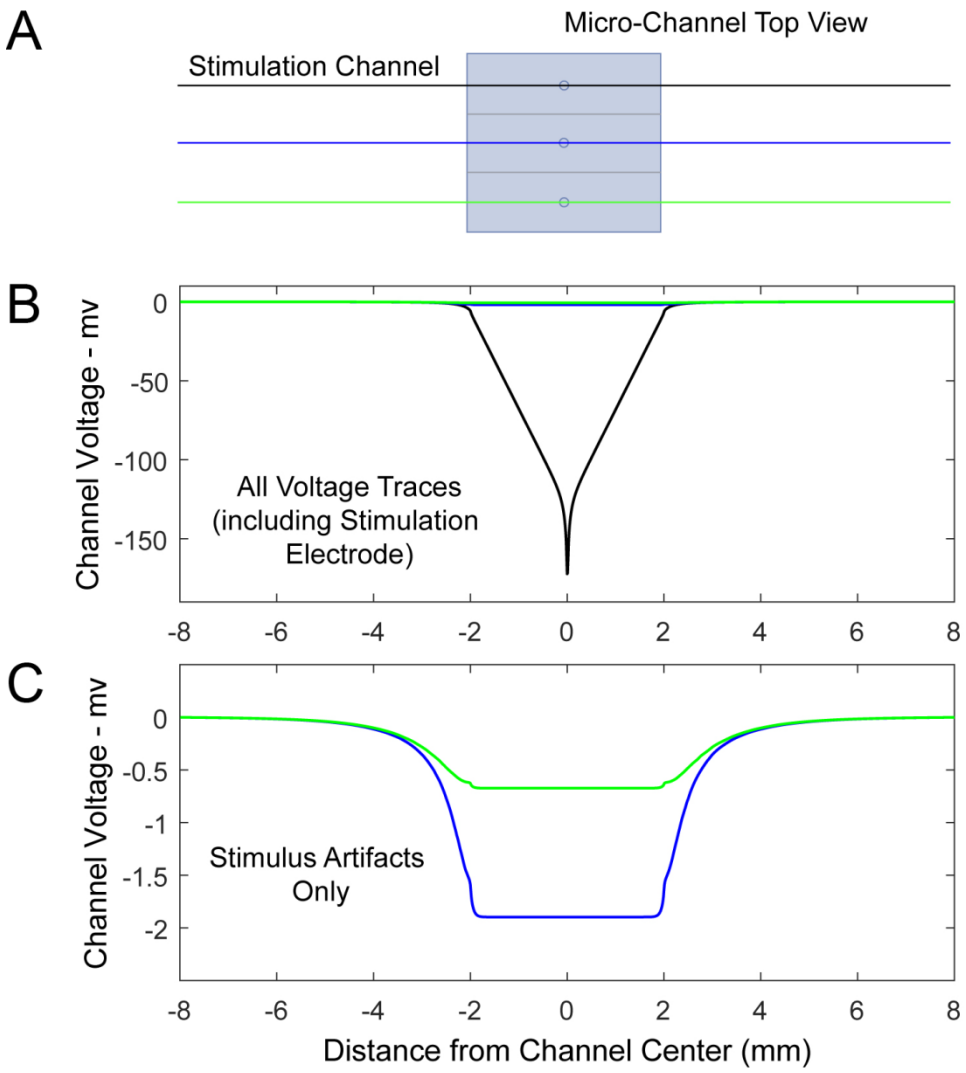

Figure 4-5. Stimulation voltage at the surface of axons running through micro-channel device (length = 4 mm, width = 120 µm) resulting from a 1 µA reference current. (**A:** Top view of micro-channel device showing 3 channels with an axon running through each channel. **B-C:** Voltage at the surface of axons running perpendicular to the device's electrodes with stimulation electrode removed (**C**) to provide greater resolution. Colors of traces in voltage plots match colors of axons in top plot. Electrical potential is much larger in the stimulation micro-channel than directly above the tfTime stimulation electrode, while the stimulus artifact in adjacent channels is comparable.

4.3.2 Comparison of stimulation current in unipolar devices

Recruitment curves were determined for the tfTIME and micro-channel devices as axon diameter was varied. Figure 4-6 compares the stimulation current required to elicit action potentials in 8 µm diameter model axons (using the CRRSS model nodal dynamics) within a 100 µm radius of the stimulating electrode for a tfTIME and within a 180 µA wide, 4 mm long micro-channel at

two nodal staggering values - directly above and maximally offset. Three salient differences between the response of axons stimulated by the two devices can be observed from this example. First, although the cross-sectional area being stimulated is comparable in the two scenarios, when the nodes of Ranvier are directly above (or below) the stimulating electrode, the micro-channel is able to elicit action potentials in 50% of the axons (50% recruitment) with 1/4 of the stimulation current required for the tfTIME device. Furthermore, for 100% activation, the micro-channel requires 1/6 the stimulation current. For implanted devices operating on battery power, this is an obvious advantage. Second, for the tfTIME device, there is a long linear range of operation in which a change in stimulation current results in progressively more neural stimulation. This is beneficial when trying to induce graded sensations from a prosthetic limb, e.g. being able to generate the gentle pressure sensation of lightly gripping an object compared to a moderate finger pressure for a tighter grip. Finally, for the micro-channel case, where a fiber's nodes of Ranvier are in relation to the stimulating electrode makes almost no difference to its activation threshold. However, for the TIME electrode, the axonal recruitment threshold increases 6 fold when the nearest two nodes are equidistant from the stimulating electrode.

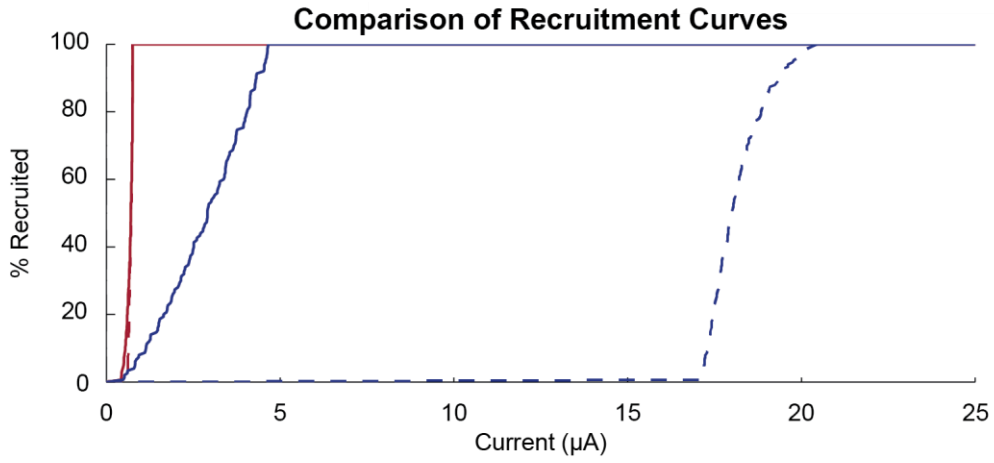

Figure 4-6. Sample neural recruitment curves for TIME (100 µA radius) (blue trace) and unipolar micro-channel (180 µA width, 4 mm length)(brown trace) electrodes for 8 µA diameter axons. TIME requires more than 4x stimulation current than micro-channel with comparable cross-section to achieve 50% recruitment (solid lines) and more than 6x for 100% recruitment (dashed lines). When random staggering is incorporated, this difference is compounded since it drastically increases the recruitment thresholds predicted for the TIME devices.

In addition to axon size variation, different radii around the tfTIMEs stimulating electrode were considered. A monopole in a homogenous material can be determined analytically to have a resulting electrical potential that is inversely proportional to the radius. Thus, trying to stimulate axons further from the electrode would be expected to require progressively more current. Conversely, under certain conditions (e.g. if one node of Ranvier is positioned directly above the center of the stimulating electrode) larger diameter axons have lower thresholds. In such cases, we would expect the stimulation threshold to decline as axon diameter increases - shifting the recruitment curve to the left. However, when the node of Ranvier nearest the stimulating electrode is offset longitudinally, there is the opposite effect that is interrelated with the overall axon distance. For axons close to the device, the distance from the closest node to the electrode is not impacted much by a longitudinal offset for a small caliber axon since the internodal distance is small. For larger axons, the longitudinal offset distance of the node can increase the overall distance from the closest node to electrode dramatically since the internodal distance is

much larger. For fibers located further away from the electrode (greater radius), this effect is not nearly as pronounced (Veltink, Alste, and Boom 1988; Veltink, van Alsté, and Boom 1989; Butson *et al.* 2011; Zellmer, MacEwan, and Moran 2017)). Both the impact of axon size and desired stimulation radius on recruitment thresholds are shown in Figure 4-7 for 50% activation (i.e. the stimulation amplitude resulting in 50% of the modeled axons firing an action potential) where nodal longitudinal placement was randomly staggered. It can be seen that the impact of axon size on recruitment thresholds saturates somewhat as the axon diameter increases beyond 5 μm for larger radii of interest. For a given axon size, shifts in recruitment thresholds solely due to radius is clearly non-linear as can be seen by comparing the increase in stimulation current between 50 and 100 to the increase between 200 and 250 μm radii.

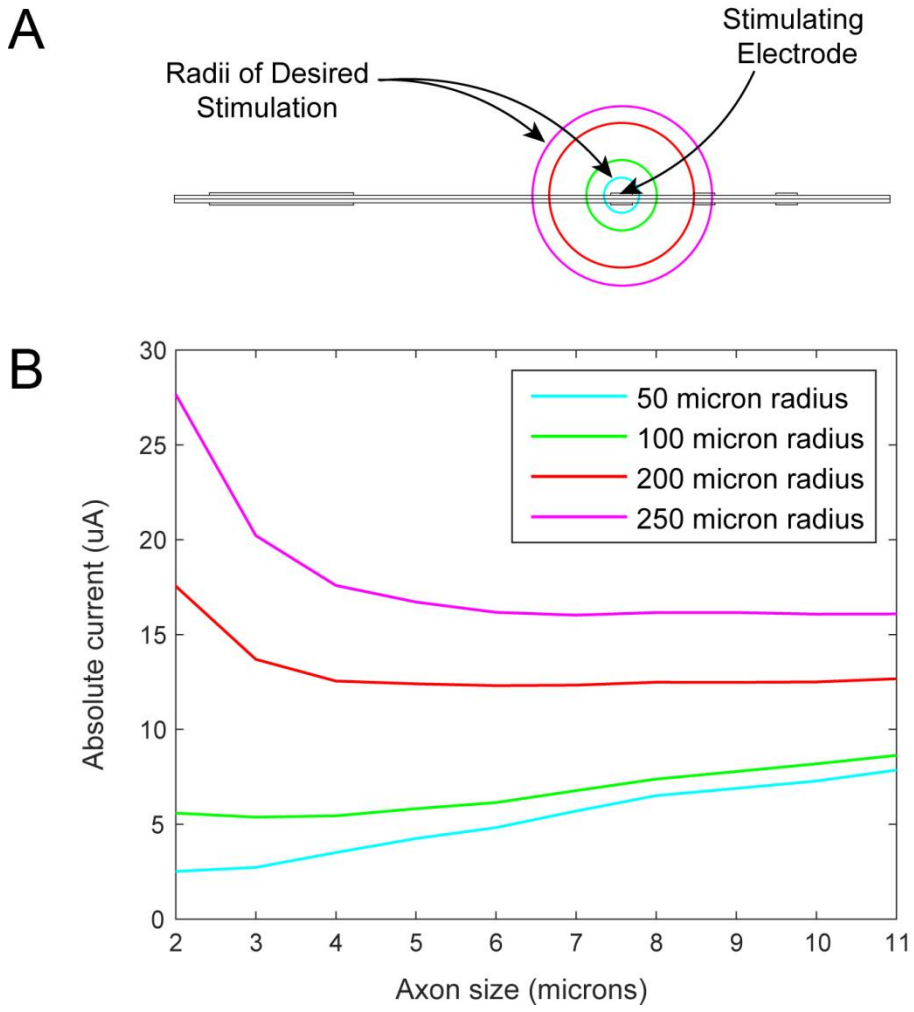

Figure 4-7. Stimulation current required to activate axons at different distances from the stimulating electrode for TIME device. **A:** Side view of the TIME device showing the 6 electrodes on the right side of the device, 2 ground electrodes on the left side of the device, and the radii of interest around the stimulating electrode. **B:** Stimulation current required to activate 50% of CRRSS model axons within the radius of interest.

Similar to the tfTIME device process, model axons were used to determine the required stimulation current for the micro-channel design. However, in this case, the length and cross-sectional area was varied. The axons of interest are only those that run through the channel. As such, there was no need to consider the stimulation radius as in the TIME case, though widening the channels had fundamentally the same effect of increasing the cross sectional area being considered. The example recruitment curve (Figure 4-6) shows significant recruitment at much

lower stimulation amplitudes than the tfTIME device did as well as a much steeper recruitment curve.

Furthermore, for micro-channel devices, the effect of modulating micro-channel length and width was examined. These parameters are relevant since the material forming the micro-channel constitutes an electrical insulator surrounding the cross-sectional area of the regenerated peripheral nervous tissue. The voltage-current relationship is described by a volume conductor in which increasing the cross-sectional area reduces the resistance while increasing the length increases the resistance. Thus, the electrical potential induced in a long channel given a reference current should be greater than that of a short channel. Conversely, the electrical potential induced in a wide channel is less than that of a narrower one. As a result, lower stimulation thresholds are expected for longer, narrower channels. The computational model confirmed this prediction (Figure 4-9A). Overall, increasing the length of the channel has a moderate impact on the 50% activation thresholds while increasing channel width showed a more dramatic effect.

4.3.3 Stimulation artifact for unipolar devices

To determine the stimulation artifact for each device, the stimulation current needed to recruit a given percentage of interfaced axons is multiplied by the voltage profile due to the reference current. The electrical potential at the site of the contact is the expected stimulation artifact. This artifact was computed for both the tfTIME device (Figure 4-8) and the micro-channel device (Figure 4-9) at 50% recruitment, while Table 4-1 shows stimulation current and artifact for both 50% and 100% recruitment. For each case, a weighted average of the 50% (or 100%) recruitment threshold was taken across the axon size using the axon size distribution for normal,

undamaged nerves (Zellmer, MacEwan, and Moran 2017) for the tfTIME and regenerated nerves for the micro-channel.

For the micro-channel device, the length of the channel has very little effect on the stimulation artifact due to a reference current (Figure 4-9B). In fact, the individual traces associated with channel length are almost on top of each other. This is due to the fact that a reference current was used. Regardless of the length of the channel, the full reference current enters the channel since there is no other path for it to travel. Thus, nearly the same artifact is elicited in adjacent channels.

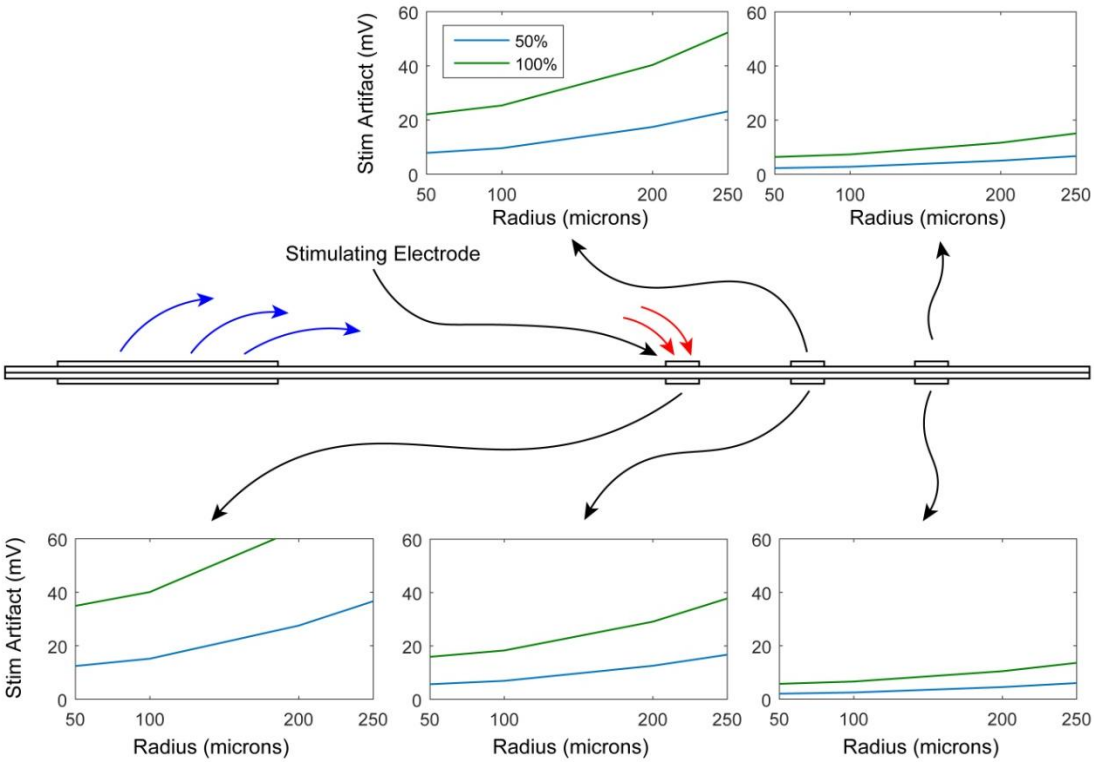

Figure 4-8. Stimulation Artifacts at TIME electrodes showing the stimulation artifact for 50% and 100% recruitment using a weighted average of axon sizes based on the size distribution in an undamaged nerve. .

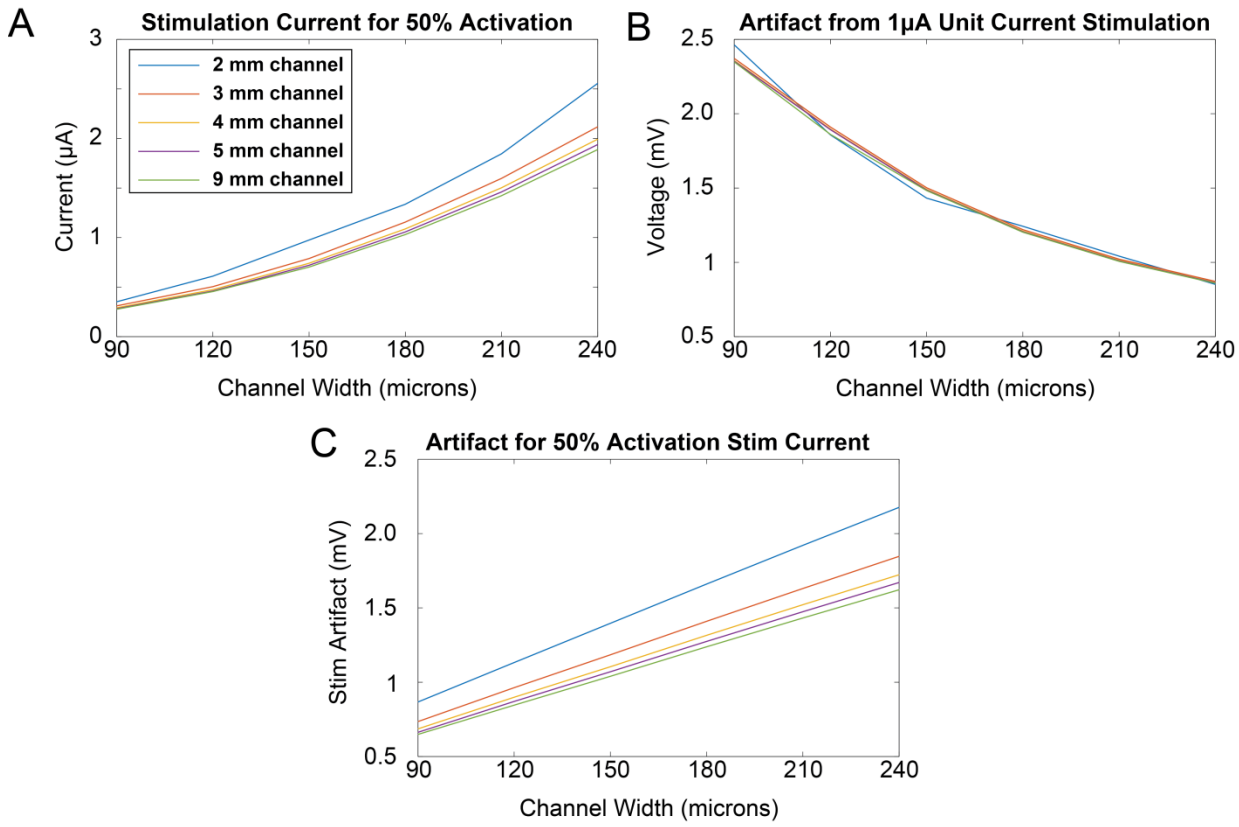

Figure 4-9. Performance of unipolar micro-channel stimulation. **A:** Stimulation current required to activate 50% of in-channel axons (CRRSS model) as a function of Micro-Channel device geometry using a weighted average of axon sizes based on the size distribution in a regenerated nerve. **B:** Voltage in the channel adjacent to the stimulated channel caused by a 1 µA reference unipolar current as channel length and width are varied. **C:** Stimulation artifact in adjacent channel for 50% CRRSS recruitment showing variation over geometry. Once the channel is at least 3 mm long, channel cross-sectional area is far more important than channel length. Artifact is much lower than for the tfTIME device.

The results of the computational modeling to determine stimulation artifact is shown in Table 4-1 below. As can be seen, the micro-channel devices compare favorably to the TIMEs across each category.

Table 4-1 Summary of Unipolar Stimulation Artifact

Measure	Device Type	
	TIME	Micro-Channel
Stimulation Artifact at adjacent channel/contact due to reference current (mV)	1.4 (adjacent contact) -2.2 (opposite side)	0.85 - 2.5 (across all geometries)

Stimulation Current (μA) for 50% recruitment	7.0 (100 μm radius)	0.27 - 2.6 (across all geometries)
Stimulation Artifact at 50% recruitment (mV)	9.6 (adjacent contact) 15.2 (opposite side) (100 μm radius)	0.65 - 2.2 (across all geometries)
Stimulation Current (μA) for 100% recruitment	18.5 (100 μm radius)	0.29 - 3.1 (across all geometries)
Stimulation Artifact at 100% recruitment (mV)	25.4 (adjacent contact) 40.1 (opposite side) (100 μm radius)	0.68 - 2.6 (across all geometries)

4.3.4 Electrical potential in multi-polar micro-channel devices

The basic unipolar micro-channel stimulation model was modified to investigate bipolar and tripolar arrangements. Among other benefits, bipolar and tripolar architectures present an opportunity to design and optimize performance by choosing the location of the electrodes within the micro-channel.

This design optimization is limited to the micro-channel architecture. Since the tfTIME device is inserted across the nerve transversely, the utility in using a bipolar or tripolar electrode configuration is minimal. It is, of course, possible to sink current from one electrode and source it from another. However, the result of this would be steering the region of activation within the nerve. For example, instead of being centered over an electrode, the activated region could be shifted to the side of the electrode. This technique would be useful to select which portion of the nerve cross-section is activated, but is a quite different effect than the desire to stimulate the same set of neurons while minimizing the artifact at neighboring electrodes.

As in the unipolar case, the electrical potential was computed along lines parallel to the micro-channel, through the center of the surface of the electrodes for bipolar (Figure 4-10) and tripolar (Figure 4-11) stimulation. The peak stimulation artifact in the adjacent channel using reference current bipolar stimulation is slightly lower than the unipolar case, but not a huge improvement. However, the artifact at channel center is nearly 0 because of the balanced current source and sink. In contrast, during unipolar stimulation, the artifact throughout the adjacent micro-channel is nearly constant. Thus, a unipolar recording in a micro-channel adjacent to bipolar stimulation would see very little stimulation artifact.

During tripolar stimulation, the center electrode is a current sink while the outside electrodes source current at half the magnitude. Similar to bipolar stimulation, the current is balanced within the micro-channel and should have very little leakage outside the channel. For the geometry shown in Figure 4-11, the peak voltage in the adjacent channel was 0.1 μV! During simulations of tripolar stimulation, modeling results were sensitive to current imbalances between the various electrodes. If, for example, one of the flanking electrodes sourced slightly more current than the other, the resulting artifact increased substantially compared to a completely symmetrical model configuration. This suggests a problem that is likely to occur in an implementation. Namely, whatever imbalance of current occurs between the electrodes will appear as a net current that flows outside the channel. As such, it will have the same effect as would be seen from unipolar stimulation. Further, it will not be mitigated by the opposing electrode since both the outer electrodes are the same polarity.

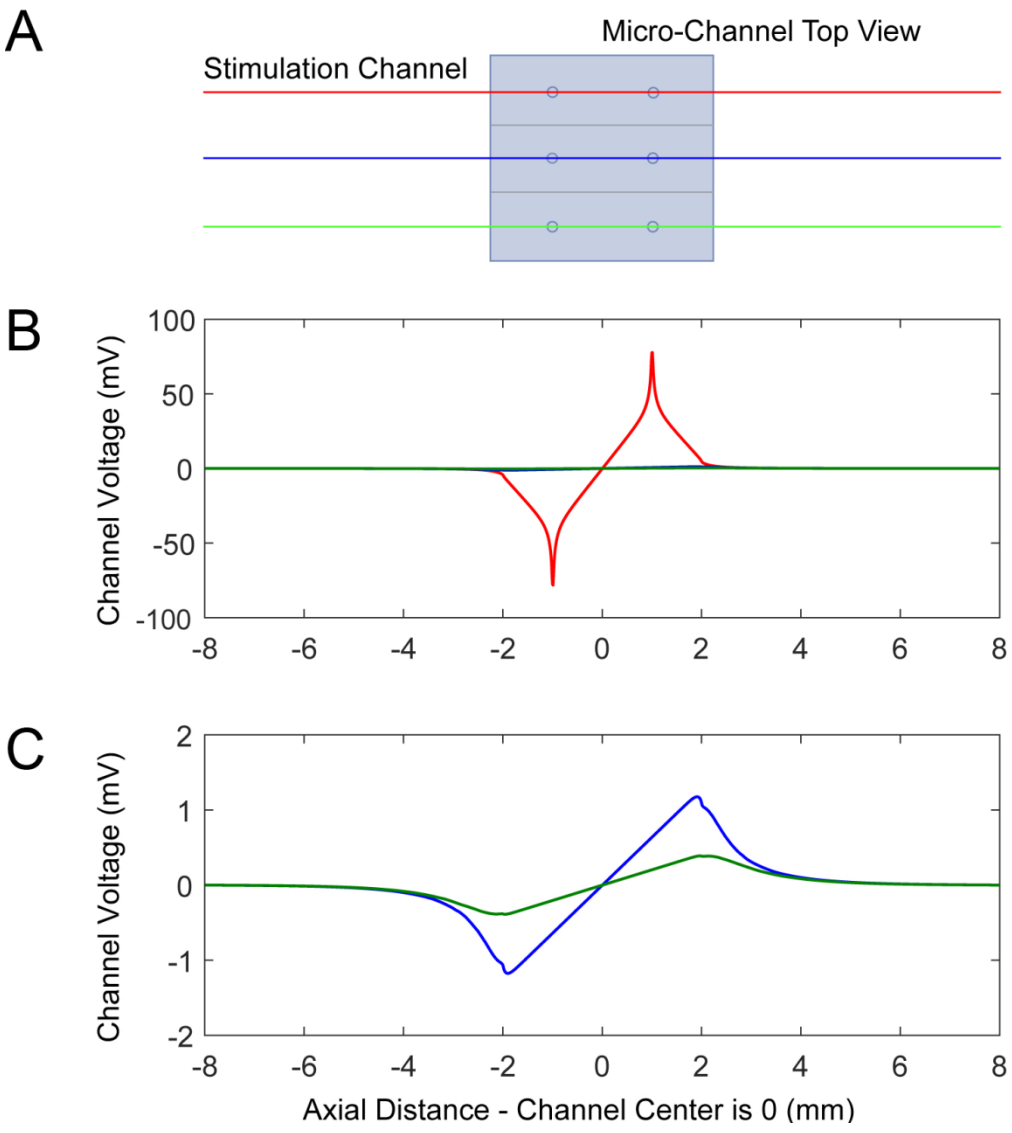

Figure 4-10. Stimulation voltage at the surface of axons running through a bipolar micro-channel device (length = 4 mm). **A:** Top view of micro-channel device showing 3 channels with an axon running through each channel. **B-C:** Voltage at the surface of axons running perpendicular to the device's electrodes with stimulation electrode removed (**C**) to provide greater resolution. Colors of traces in voltage plots match colors of axons in top plot. Electrical potential is reduced compared to unipolar stimulation, but the voltage gradient is still large and the stimulus artifacts are correspondingly reduced.

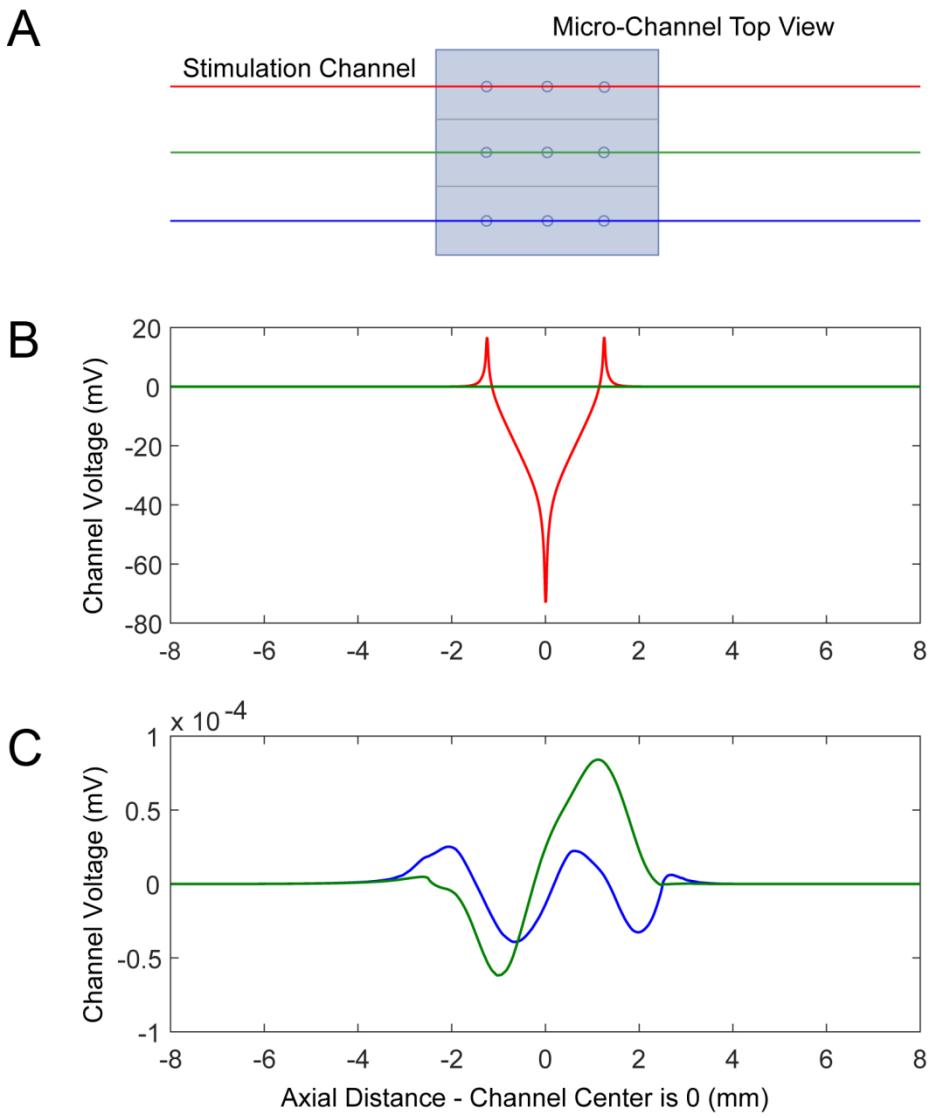

Figure 4-11. Stimulation voltage at the surface of axons running through a tripolar micro-channel device (length = 4 mm). **A:** Top view of micro-channel device showing 3 channels with an axon running through each channel. **B-C:** Voltage at the surface of axons running perpendicular to the device's electrodes with stimulation electrode removed (**C**) to provide greater resolution. Colors of traces in voltage plots match colors of axons in top plot. Electrical potential is reduced compared to unipolar stimulation, but the stimulus artifacts are almost entirely removed (sub µV range).

4.3.5 Design optimization, stimulation current and artifact in multi-polar micro-channel devices

A key design question when using multi-polar stimulation is where to place the electrodes (contacts) for optimal performance. To determine this, the contact placement was varied in 5% increments of the half-channel length (contact placement is illustrated in Figure 4-12A) in a

subset of micro-channel geometries and axon diameters. In general, a low-middle-high strategy was used for parameter values to get a representative covering of the space. The parameter values were:

- Channel Length: 2, 5, and 9 mm
- Channel Width: 90, 165, and 240 μm
- Axon Diameter: 2, 4, 9 μm

providing 27 combinations in each of which the contact placement was tested at 5% increments. Longitudinal staggering of nodes of Ranvier was not used since it had little effect in the micro-channel case and was considered, therefore, unlikely to differentially affect contact placement. As before, the voltage profile generated in COMSOL was used within NEURON to determine the stimulation threshold. The required stimulation current as a function of contact placement was normalized across micro-channel geometry and axon diameter (27 combinations) to be able to determine the optimal contact placement. The normalized data (stimulation data normalized to have a minimal stimulation current of 1 μA) shows that the results are consistent across geometries and axon diameters (Figure 4-12).

For bipolar stimulation, the stimulation current is minimized in the 40 - 60% contact placement with the lowest value being at 50% (Figure 4-12B) meaning that the contacts are half-way between the channel center and edge. The same strategy was used in the tripolar case. The farther the contacts are apart, the lower the stimulation current as shown in Figure 4-12C. However, the improvement from 40% to 95% is quite small (Figure 4-12C).

Minimizing the required stimulation current only optimizes for one variable, whereas the total stimulation artifact depends on two. The second variable is the effect of contact placement on the stimulation artifact in the adjacent micro-channel. Using the same micro-channel geometries

specified above, the peak-peak voltage for the 9 geometries was extracted from the potential profiles generated in COMSOL. The axon size did not need to be varied since it does not affect the artifact. Again, the data was normalized in order to see which contact placement minimized stimulation artifact. Across geometries, placing the contacts as close as possible to center resulted in the lowest stimulation artifact as shown in Figure 4-13 (Stim Artifact trace).

The two design goals had conflicting optimal solutions. To minimize the stimulation artifact, the electrodes should be placed at 5%. However, that results in the largest required stimulation currents. Since the stimulation artifact computation is based on a reference current, increasing the required stimulation current acts as a scale factor to find the actual stimulation artifact. To determine the optimal design with these competing factors, they were converted to a logarithmic scale where the multiplication of the stimulation current by the reference artifact can be performed as an addition. Figure 4-13 shows the results of combining the effects of stimulation artifact and threshold. The 5% contact placement is optimal to minimize stimulation artifact even after considering that a much higher stimulation current is required.

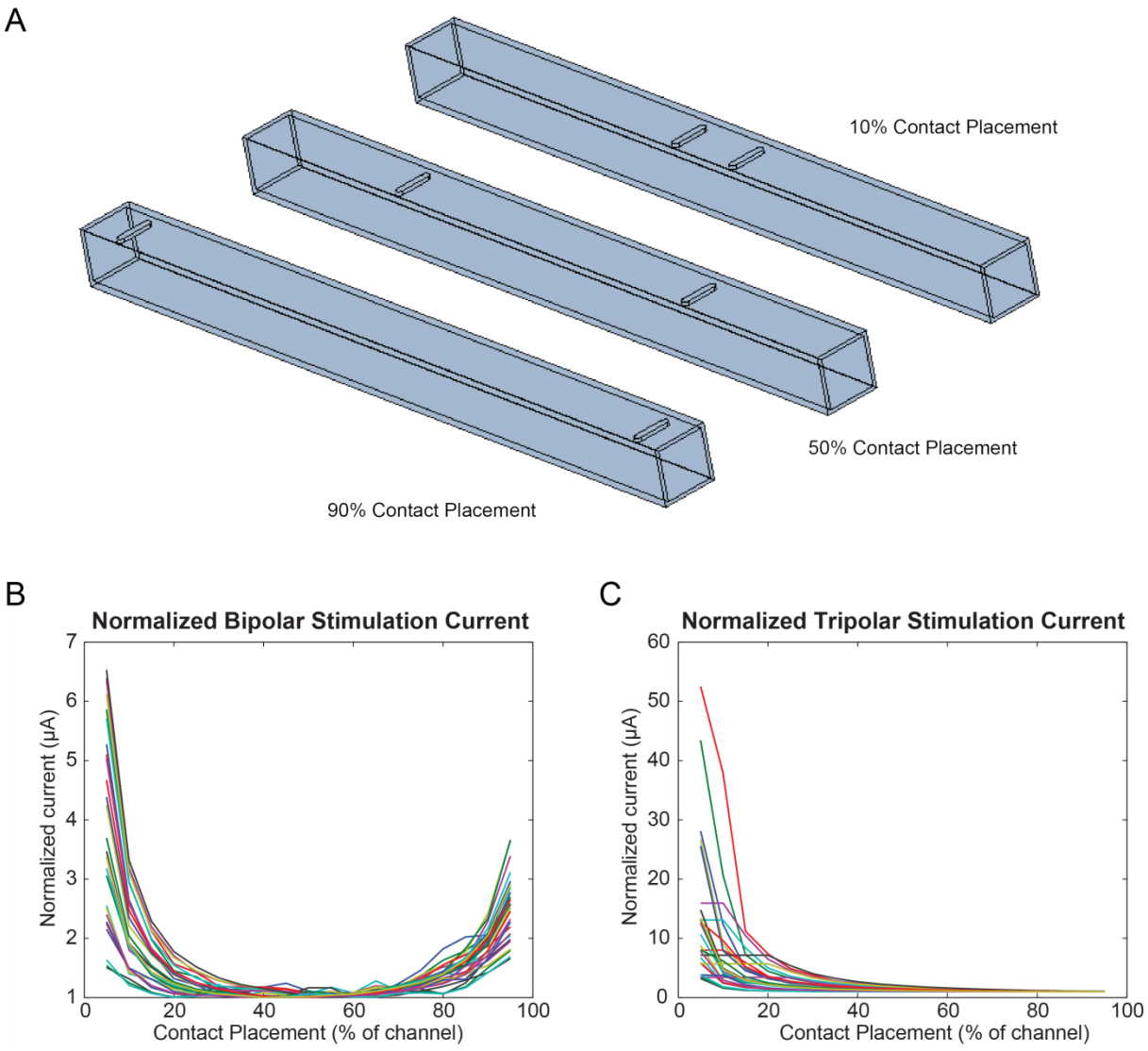

Figure 4-12. Optimal placement of contacts in bipolar and tripolar micro-channels. **A:** Illustration of contact placements for 10%, 50% and 90% locations. Percentage denotes fractional distance between channel center and edge. Tripolar configurations have an additional contact at channel center. **B-C:** Stimulation current thresholds (CRRSS, 50% activation) as a function of contact placement for all combinations of axon sizes (2, 4, 9 µm diameter), channel widths (90, 165, 240 µm) and lengths (2, 5, 9 mm) with all curves scaled to have a minimum value of 1 µA. **B:**. Bipolar geometries consistently have lowest required stimulation current at contact placement = 50% with a large flat region between 30% and 70%. **C:** Tripolar geometries have lowest required stimulation currents with the contacts as far from center as possible, though the curve flattens for placements above 40%.

While 5% is the optimal contact placement, one may also want to minimize stimulation current even if that is sub-optimal in terms of stimulation artifact. This would be the case, for example,

during optimizations of implant battery life. So, using the 5% and 50% contact placements, the full set of geometries and axon sizes was tested and nodes of Ranvier were staggered:

- Channel Length: 2, 3, 4, 5, and 9 mm
- Channel Width: 90 - 240 μm in 30 μm increments
- Axon Size: 2 - 11 μm in 1 μm increments
- Nodal staggering: 0 - 50% in 5% increments

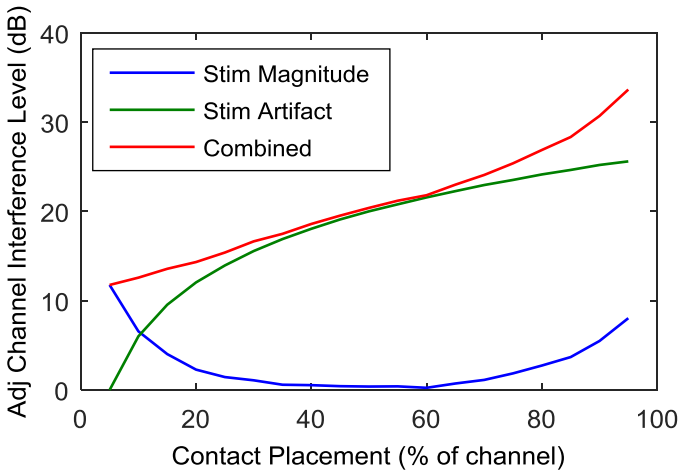

Figure 4-13. Bipolar Micro-channel Performance. This shows the combined effect of stimulation current threshold and stimulation artifact induced by reference current. Data is averaged over geometry and axon size. Optimal contact placement for minimizing stimulation artifact is as close to channel center as possible. Optimal location for minimizing stimulation current is 50%. When these effects are combined, placing contacts near channel center minimizes adjacent channel interference.

The required stimulation current to generate 50% recruitment in the CRRSS axon model as a function of geometry and averaged across axon size was determined (Figure 4-14A). As was seen in the initial set of simulations, using a 5% contact placement requires much greater stimulation current - as high as 20.5 μA in the worst case. On the other hand, the highest stimulation current for the 50% contact placement was 3.4 μA. As expected from the unipolar case as well as general principles, increasing the channel width and decreasing the channel length results in a greater stimulation current threshold.

To determine expected stimulation artifact, the stimulation current was used to scale the stimulation artifact resulting from stimulation with the reference stimulation current. Looking at the stimulation artifact in the adjacent micro-channel as a result of stimulation at the threshold, the highest artifact at adjacent channel center is < 10 µV for the 50% contact placement (Figure 4-14C).

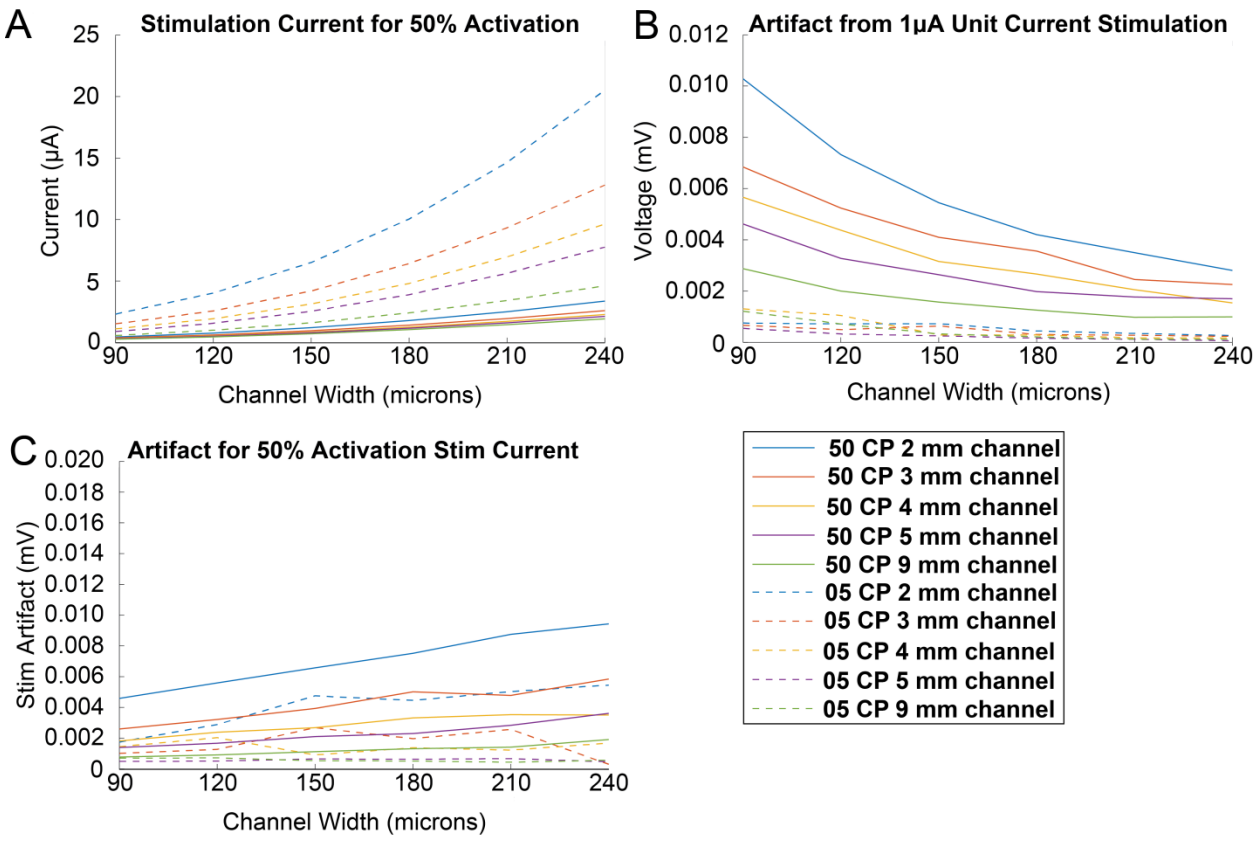

Figure 4-14. Bipolar results averaged across axon sizes. **A-B:** Stimulation Current required to activate 50% of axons across device size (micro-channel length and width) and contact placements and artifacts produced using the reference current (5% for minimum artifact, and 50% for minimum stimulation current). **C:** Corresponding stimulation artifacts.

Both bipolar stimulation and tripolar stimulation results were numerically sensitive. However, with proper meshing for tripolar stimulation, all stimulation artifacts from the 1 µA reference current were less than 70 µV and less than 2 µV for the 50% contact placement! As in the

bipolar case, placing the contacts near channel center resulted in the lowest stimulation artifact from a reference current (Figure 4-15B).

Two electrode placements were chosen to test the impact of interface geometry on recruitment thresholds and stimulation artifacts. The 95% contact placement was chosen because it has the lowest stimulation current threshold (Figure 4-15A). Additionally, the 50% contact placement was chosen for a few reasons. First, it is a suitable electrode placement for bipolar stimulation. Therefore, this electrode placement would make it easy to switch between stimulation paradigms - bipolar and tripolar. An additional reason is that having the electrodes closer to center reduces the stimulation artifact (Figure 4-15B). At 50% contact placement, the stimulation threshold was still relatively low as the improvement seemed asymptotic, so the combination of being able to use the same contact placements as bipolar, dramatically reducing the stimulation artifact, while maintaining very low current requirements merited including it.

As with the bipolar design, the stimulation current required to generate 50% activation of the model axons as a function of device geometry and averaged across axon sizes for 50% and 95% contact placements was computed (Figure 4-15A). If a channel length of at least 4 mm is used, the 50% contact placement required only slightly more stimulation current to achieve a comparable level of axonal recruitment compared to the 95% contact placement. As in the bipolar paradigm, the required stimulation current was used to scale the stimulation artifact from a reference current to create the total stimulation artifact (Figure 4-15C).

There is a clear advantage of the 50% contact placement. It has a much lower stimulation artifact due to a reference current while having only slightly larger required stimulation currents.

This results in a stimulation artifact much lower than the 95% contact placement. The worst case stimulation artifact from the 50% contact placement is 2 μV!

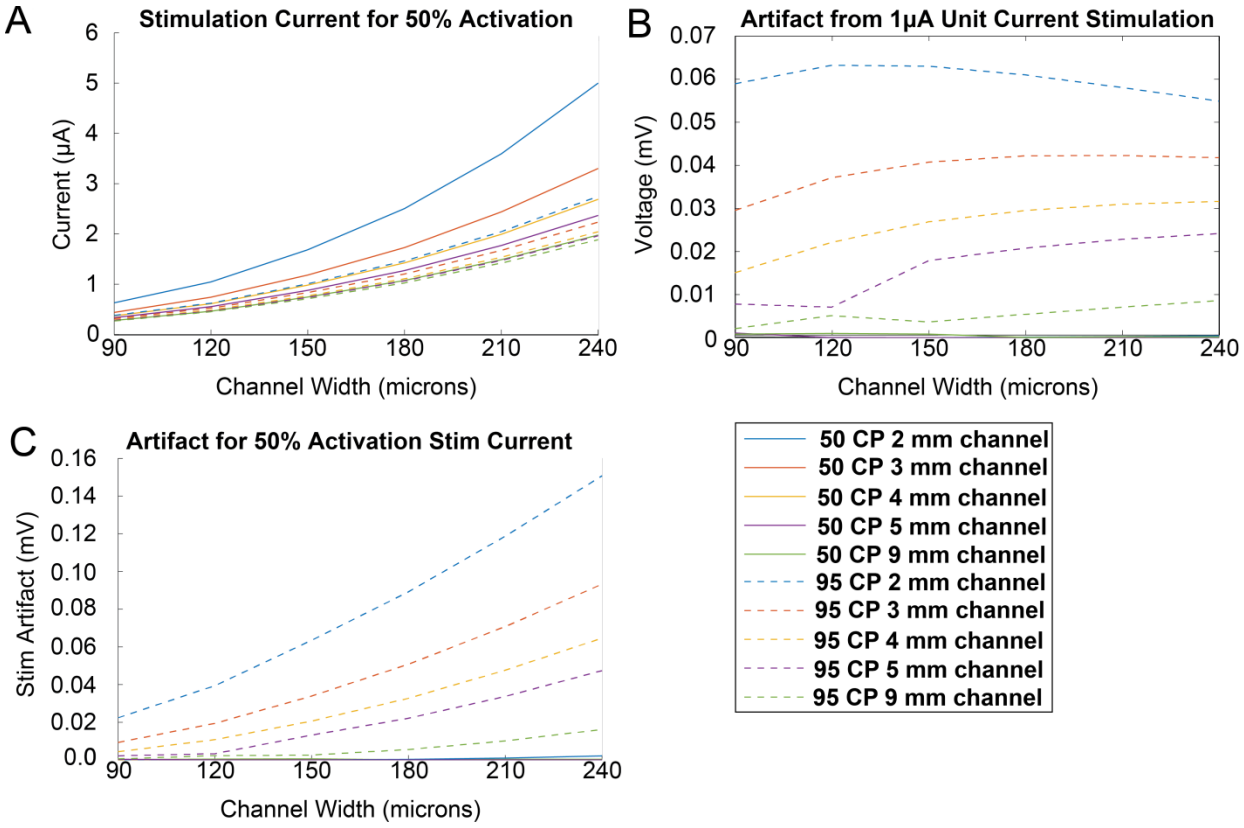

Figure 4-15. Tripolar results averaged across axon sizes. **A-B:** Stimulation Current required to activate 50% of axons across device size (micro-channel length and width) and contact placements and artifacts produced using the reference current (50% for minimum artifact, and 95% for minimum stimulation current). **C:** Corresponding stimulation artifacts.

Table 4-2 Summary of Multi-polar Micro-channel Stimulation Artifact

Measure	Micro-channel Stimulation Paradigm	
	Bipolar	Tripolar
Stimulation Artifact at adjacent channel contact due to reference current (μV)	< 1 (5% CP) 1 – 10 (50% CP)	< 2 (50% CP) 2 –63 (95% CP)
Stimulation Current (μA) for 50% recruitment	0.6 – 20.5 (5% CP) 0.27 – 3.4 (50% CP)	0.28 – 5.0 (50% CP) 0.27 – 2.7 (95% CP)
Stimulation Artifact at 50% recruitment (μV)	0.4 – 5.5 (5% CP) 0.75 – 9.5 (50% CP)	< 2 (50% CP) 0.5 –150 (95% CP)

Stimulation Current (μA) for 100% recruitment	0.65 – 34.2 (5% CP) 0.28 – 4.8 (50% CP)	0.28 – 7.7 (50% CP) 0.28 – 3.6 (95% CP)
Stimulation Artifact at 100% recruitment (mV)	0.6 – 9.1 (5% CP) 0.8 – 13.6 (50% CP)	< 2 (50% CP) 0. 6 – 200 (95% CP)

A summary of the micro-channel multi-polar computation results is shown in Table 4-2.

4.4 Discussion

4.4.1 Comparison of unipolar micro-channel with tfTIME

The unipolar micro-channel regardless of the exact geometry has substantially lower artifact at adjacent recording sites (adjacent on the same side and site directly opposite the stimulation) than the tfTIME. This advantage is caused by two effects. First, the stimulation artifact for a given reference stimulation current is typically lower, though that is dependent on the micro-channel geometry. Narrower channels did create comparable artifacts to the opposite tfTIME recording site. Second, the voltage inside the micro-channel is considerably higher for the reference stimulation current. This meant that lower stimulation currents could be used to achieve a given degree of axonal activation resulting in overall lower stimulation artifacts.

The unipolar stimulation artifact was computed at the stimulation current amplitudes sufficient to activate 50% of the axons within the micro-channel or within a given radius of the tfTIME electrode. However, the recruitment curve of the tfTIME was much more gradual than that of the micro-channel (Figure 4-6). While the reduced stimulation current of the micro-channel is certainly desirable, the sharp transition between no axonal activation and complete activation

leaves less room to generate a graded sensation unless multiple micro-channels contained sensory axons originating from a similar source. For such axonal topographies, instead of progressively increasing the stimulation current within a single micro-channel, it would be possible to provide suprathreshold stimuli through multiple micro-channels to create a sense of progression. The smaller in cross-section the channels are, the more likely that would be the case since it would allow for greater separation of spatially clustered functionally similar axons. Also, multiple studies have shown that stimulation frequency can be modulated to control intensity of percepts (Dhillon *et al.* 2004; Dhillon and Horch 2005). While the tfTIMEs recruitment characteristics arguably makes controlling graduated sensation easier to accomplish, it also means that the micro-channels advantage in terms of stimulation current and corresponding artifact is understated at 50%. The tfTIME stimulus artifact would be more than twice as large for 100% recruitment while the micro-channel's would increase only slightly.

4.4.2 Multi-polar stimulation in micro-channels

Compared to unipolar micro-channel stimulation, bipolar stimulation with the 50% contact placement required comparable stimulation current. Bringing the contacts closer together (5%) dramatically increased the required stimulation current (Figure 4-16A). Despite the increased stimulation current, the stimulation artifact at 5% contact placement was found to be lower than that of 50%. For either contact placement, the highest stimulation artifact was less than 10 μV, roughly 200 times lower than the unipolar case for corresponding micro-channel geometries. For narrower channels, the improvement is even more pronounced (Figure 4-16B).

Tripolar stimulation also had an advantage over unipolar. The threshold stimulation current amplitudes were in the same range with the 95% contact placement, while the 50% contact

placement required somewhat greater stimulation current for certain geometries. Due to the current being balanced within the channel (similar to during bipolar stimulation), the stimulation artifact was much lower than unipolar stimulation (Figure 4-16B). Depending on channel placement, the tripolar stimulation resulted in higher or much lower stimulation artifacts compared to bipolar stimulation (Figure 4-17). Very low bipolar stimulation artifacts were only found at channel center and relied on perfect balance of currents and homogeneity of neural tissue. Importantly, the peak voltage in the channel adjacent to bipolar stimulation was much higher during bipolar stimulation than during tripolar stimulation. As such, the recording site should be positioned at channel center. *In vivo* testing should be used to assess whether such low artifacts are attainable in practice. During simulations of tripolar stimulation with 50% contact placement the largest magnitude voltage in the adjacent micro-channel for any geometry was less than 1 μV during stimulation with the reference current. Such low artifacts are again dependent on currents being perfectly balanced. However, *in-vivo* measurements may show less sensitivity to the homogeneity of the neural tissue since the electrical potential in the adjacent channel has lower peak voltages.

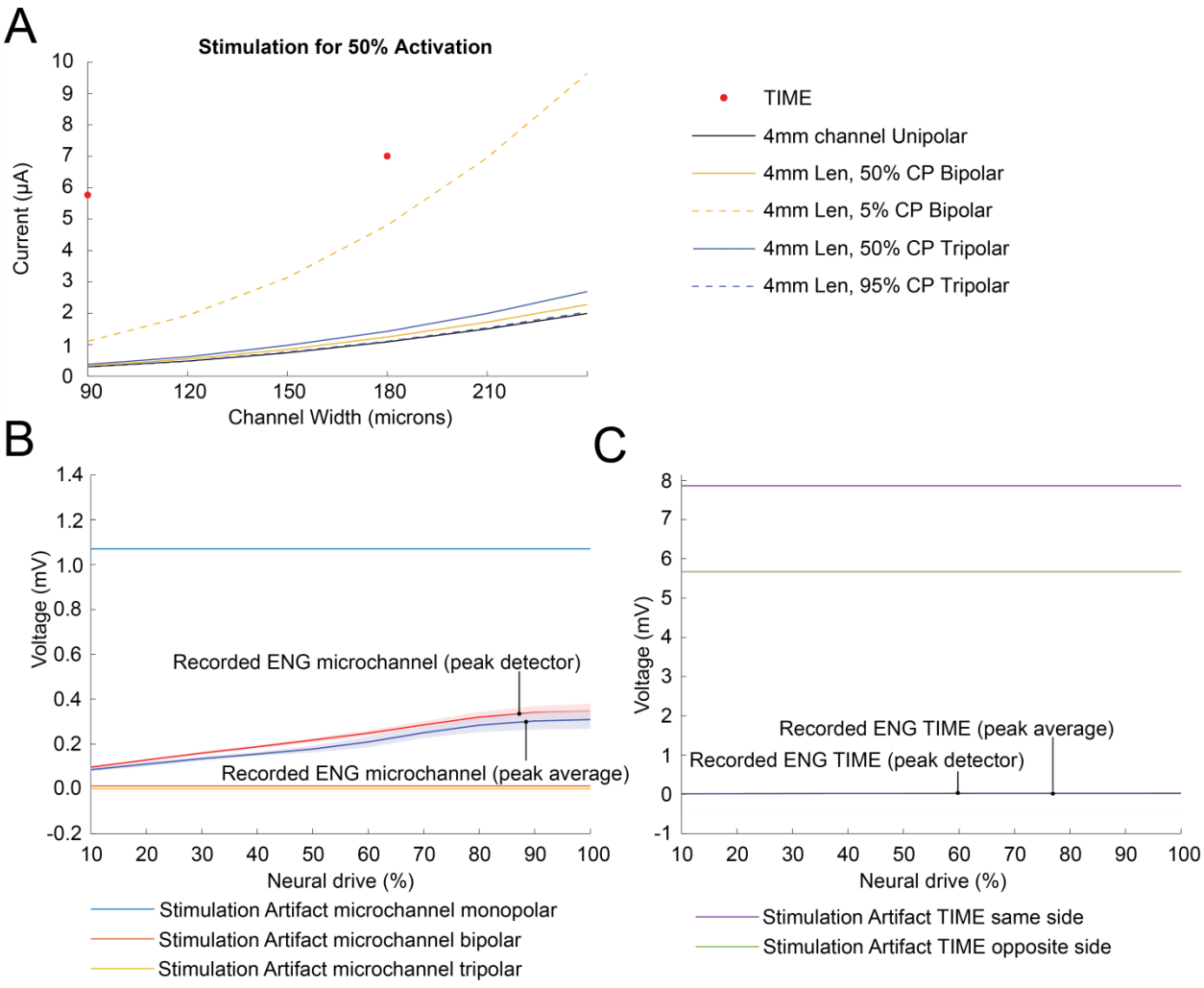

Figure 4-16. **A:** Comparison between stimulation currents required to achieve 50% activation during stimulation using the TIME, and the micro-channel devices in unipolar, bipolar and tripolar configurations. **B:** Recorded ENG traces from micro-channel (see companion paper) together with stimulation artifacts during stimulation of regenerated fibers from the micro-channel device. Stimulation artifacts are larger than signals during unipolar stimulation but much lower during bipolar and tripolar stimulation. **C:** Recorded ENG traces from TIME together with stimulation artifacts during stimulation of normal fibers. Note the massive discrepancy in voltages between the recorded ENG signals (See companion paper) and the artifacts.

Overall, simulations showed that computational results of both bipolar and tripolar stimulations were sensitive to small geometrical discrepancies and current balances. This caused significant shifts in the simulated results due to the sensitivity of the model. During bipolar stimulations, we observed a negative voltage peak on one side of the adjacent channel and a positive peak on the other. Therefore, a large gradient in the electrical potential was observed at the center, making

the computed stimulation artifact quite numerically sensitive. For the tripolar case, the sensitivity of the model manifested itself somewhat differently. Instead of being caused by the exact spatial balance between positive and negative peaks in the channel, the sensitivity was caused by current imbalances. In the tripolar configuration, the outer electrodes are the same polarity. However, any imbalance in the current between the sites will manifest as a net current flow in or out of the micro-channel. The shape of the electrical potential curve in the adjacent channel is the same as during unipolar micro-channel stimulation, albeit with a much lower voltage. If the currents are perfectly matched, the adjacent channel artifact will approach zero as was seen in one device geometry where the peak voltage in the adjacent channel was less than 0.1 µV.

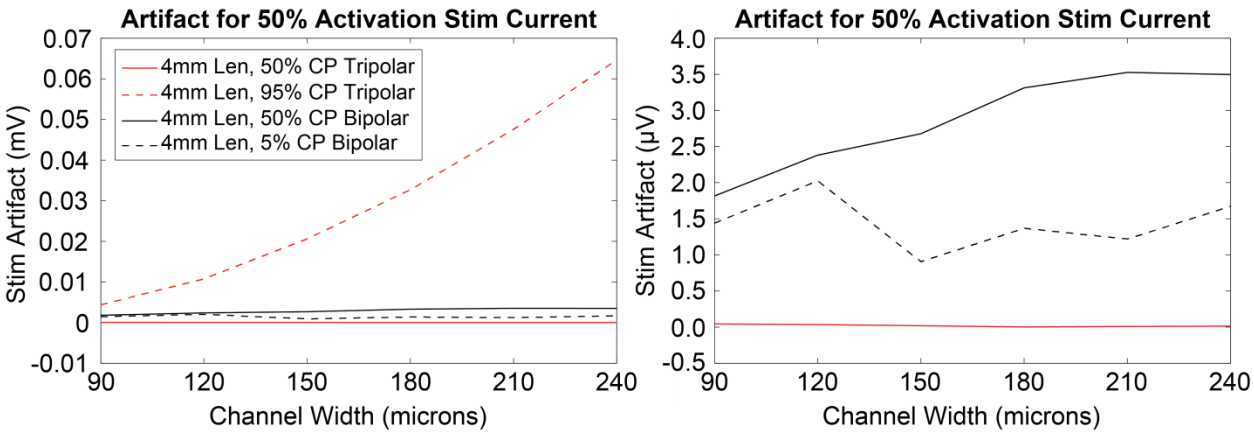

Figure 4-17. Side by side comparisons between stimulation artifacts generated during bipolar and tripolar stimulation with different contact placements. Notably, the stimulation artifact is higher during tripolar stimulation with certain channel placements (A) while being substantially lower for other channel placements.

4.4.3 Signal-to-Artifact ratio

Incorporating the results from the companion paper, Signal-to-Artifact ratios are shown in Table 4-3. One key concern in implementing a bi-directional system is having such large stimulation artifacts that preamplifiers may saturate. Of course, an amplifier could be designed with enough

input range; however, the following digitizing circuitry would require much higher resolution (i.e. bits). Even so, there would be additional system complexity in the processing software as well. For both tfTIME and unipolar micro-channel stimulation, the artifact is larger than the recorded signal (Figure 4-16 B-C). As a result, the stimulation system would need to estimate the voltage artifact that is created and subsequently subtract it from the recorded signal before trying to process the electroneurogram (ENG) for a given recording site.

Table 4-3 Signal-to-Artifact ratio across device types and stimulation techniques. Peak ENG uses Peak Detector metric from companion paper. Micro-channel recordings are unipolar for reasons given in companion paper.

Measure	tfTIME (100 μm radius for stimulation, 75 μm radius for recording)	Micro-channel Stimulation (150 μm wide, 5 mm long)		
		Unipolar	Bipolar (50% contact placement)	Tripolar (50% contact placement)
Peak ENG at 50% Neural Drive (μV)	22.9	218	218	218
Peak ENG at 100% Neural Drive (μV)	26.7	348	348	348
Stimulation Artifact at 50% Activation (μV)	15200	1070	2.1	< 0.5
Stimulation Artifact at 100% Activation (μV)	40100	1170	2.3	< 0.5
Signal-to-Artifact ratio (dB) at 50% Neural Drive & 50% Activation	-56.4	-13.8	40.3	> 52.8
Signal-to-Artifact ratio (dB) at 50% Neural Drive & 100% Activation	-64.9	-14.6	39.5	> 56.9
Signal-to-Artifact ratio (dB) at 100% Neural Drive & 50% Activation	-55.1	-9.8	44.4	> 52.8
Signal-to-Artifact ratio (dB) at 100% Neural Drive & 100% Activation	-63.5	-10.5	43.6	> 56.9

Given that the unipolar micro-channel outperforms the tfTIME by 40 - 50 dB in signal-to-artifact ratio, electronics design requirements for both the preamplifier and the Digital-to-Analog

Converter (DAC) for the micro-channel would be much less (e.g., the DAC could have 7 - 8 less bits of resolution).

For either of the two multi-polar micro-channel configurations, additional circuit capability to handle stimulation artifact is not needed. In both cases, the signal is much greater than the artifact meaning that the preamplifier would only need to match the dynamic range of the ENG. As such, no extra resolution is required in the DAC to be able to continue recording ENG signals in the presence of a stimulation artifact.

4.4.4 Choice of Axon Model

During initial simulation trials, this study used multiple axons models to assess axonal recruitment. The choice of utilizing the CRRSS model exclusively was made after it was found that it produced simulated recruitment thresholds most similar to those found in an *in-vivo* rat sciatic nerve model (Zellmer, MacEwan, and Moran 2017). Secondly, the companion paper used the CRRSS model for determining the expected ENG used in this paper to determine signal-to-artifact ratios. Based on the earlier work and our initial efforts, alternate axonal models would result in moderate shifts in simulated recruitment thresholds but would not be expected to have a large impact on relative differences in recruitment thresholds (thresholds would either increase or decrease for all configurations of electrodes and fiber populations).

4.5 References

Akin, T., K. Najafi, R.H. Smoke, and R.M. Bradley. 1994. "A Micromachined Silicon Sieve Electrode for Nerve Regeneration Applications." *IEEE Transactions on Biomedical Engineering* 41 (4):305–13. https://doi.org/10.1109/10.284958.

Badia, Jordi, Stanisa Raspopovic, Jacopo Carpaneto, Silvestro Micera, and Xavier Navarro. 2016. "Spatial and Functional Selectivity of Peripheral Nerve Signal Recording With the Transversal

Intrafascicular Multichannel Electrode (TIME)." *IEEE Transactions on Neural Systems and Rehabilitation Engineering* 24 (1):20–27.

Beuche, W., and R. L. Friede. 1985. "A New Approach toward Analyzing Peripheral Nerve Fiber Populations. II. Foreshortening of Regenerated Internodes Corresponds to Reduced Sheath Thickness." *Journal of Neuropathology and Experimental Neurology* 44 (1):73–84.

Biddis, Elaine A., and Tom T. Chau. 2007. "Upper Limb Prosthesis Use and Abandonment: A Survey of the Last 25 Years." *Prosthetics and Orthotics International* 31 (3):236–57. https://doi.org/10.1080/03093640600994581.

Bjornsson, C S, S J Oh, Y A Al-Kofahi, Y J Lim, K L Smith, J N Turner, S De, B Roysam, W Shain, and S J Kim. 2006. "Effects of Insertion Conditions on Tissue Strain and Vascular Damage during Neuroprosthetic Device Insertion." *Journal of Neural Engineering* 3 (3):196–207. https://doi.org/10.1088/1741-2560/3/3/002.

Boretius, Tim, Jordi Badia, Aran Pascual-Font, Martin Schuettler, Xavier Navarro, Ken Yoshida, and Thomas Stieglitz. 2010. "A Transverse Intrafascicular Multichannel Electrode (TIME) to Interface with the Peripheral Nerve." *Biosensors & Bioelectronics* 26 (1):62–69. https://doi.org/10.1016/j.bios.2010.05.010.

Butson, Christopher R., Ian O. Miller, Richard A. Normann, and Gregory A. Clark. 2011. "Selective Neural Activation in a Histologically Derived Model of Peripheral Nerve." *Journal of Neural Engineering* 8 (3):036009. https://doi.org/10.1088/1741-2560/8/3/036009.

Childress, Dudley S. 1980. "Closed-Loop Control in Prosthetic Systems: Historical Perspective." *Annals of Biomedical Engineering* 8 (4–6):293–303. https://doi.org/10.1007/BF02363433.

Chiu, S Y, J M Ritchie, R B Rogart, and D Stagg. 1979. "A Quantitative Description of Membrane Currents in Rabbit Myelinated Nerve." *The Journal of Physiology* 292 (1):149–66. https://doi.org/10.1113/jphysiol.1979.sp012843.

Cordella, Francesca, Anna Lisa Ciancio, Rinaldo Sacchetti, Angelo Davalli, Andrea Giovanni Cutti, Eugenio Guglielmelli, and Loredana Zollo. 2016. "Literature Review on Needs of Upper Limb Prosthesis Users." *Frontiers in Neuroscience* 10. https://doi.org/10.3389/fnins.2016.00209.

Cozzi, L, P D'Angelo, M Chiappalone, AN Ide, A Novellino, S Martinoia, and V Sanguineti. 2005. "Coding and Decoding of Information in a Bi-Directional Neural Interface." *Neurocomputing* 65–66:783–92.

Dhillon, G.S., and K.W. Horch. 2005. "Direct Neural Sensory Feedback and Control of a Prosthetic Arm." *IEEE Transactions on Neural Systems and Rehabilitation Engineering* 13 (4):468–72. https://doi.org/10.1109/TNSRE.2005.856072.

Dhillon, Gurpreet S, Stephen M Lawrence, Douglas T Hutchinson, and Kenneth W Horch. 2004. "Residual Function in Peripheral Nerve Stumps of Amputees: Implications for Neural Control of Artificial Limbs1." *The Journal of Hand Surgery* 29 (4):605–15. https://doi.org/10.1016/j.jhsa.2004.02.006.

Fitzgerald, James J., Stéphanie P. Lacour, Stephen B. McMahon, and James W. Fawcett. 2008. "Microchannels as Axonal Amplifiers." *IEEE Transactions on Bio-Medical Engineering* 55 (3):1136–46. https://doi.org/10.1109/TBME.2007.909533.

Fugleholm, K., H. Schmalbruch, and C. Krarup. 2000. "Post Reinnervation Maturation of Myelinated Nerve Fibers in the Cat Tibial Nerve: Chronic Electrophysiological and Morphometric Studies." *Journal of the Peripheral Nervous System: JPNS* 5 (2):82–95.

Greenman, M. J. 1913. "Studies on the Regeneration of the Peroneal Nerve of the Albino Rat: Number and Sectional Areas of Fibers: Area Relation of Axis to Sheath." *The Journal of Comparative Neurology* 23 (5):479–513. https://doi.org/10.1002/cne.900230503.

Gutmann, E., and F. K. Sanders. 1943. "Recovery of Fibre Numbers and Diameters in the Regeneration of Peripheral Nerves." *The Journal of Physiology* 101 (4):489–518.

Hildebrand, C., J. D. Kocsis, S. Berglund, and S. G. Waxman. 1985. "Myelin Sheath Remodelling in Regenerated Rat Sciatic Nerve." *Brain Research* 358 (1–2):163–70.

Hines, M L, and N T Carnevale. 1997. "The NEURON Simulation Environment." *Neural Computation* 9:1179–1209.

Hiscoe, H. B. 1947. "Distribution of Nodes and Incisures in Normal and Regenerated Nerve Fibers." *The Anatomical Record* 99 (4):447–75.

Horch, K., S. Meek, T.G. Taylor, and D.T. Hutchinson. 2011. "Object Discrimination With an Artificial Hand Using Electrical Stimulation of Peripheral Tactile and Proprioceptive Pathways With Intrafascicular Electrodes." *IEEE Transactions on Neural Systems and Rehabilitation Engineering* 19 (5):483–89. https://doi.org/10.1109/TNSRE.2011.2162635.

Kim, Bongkyun, Alejandro Reyes, Bernardo Garza, and Yoonsu Choi. 2015. "A Microchannel Neural Interface with Embedded Microwires Targeting the Peripheral Nervous System." *Microsystem Technologies* 21 (7):1551–57.

Kuiken, Todd A., Paul D. Marasco, Blair A. Lock, R. Norman Harden, and Julius P. A. Dewald. 2007. "Redirection of Cutaneous Sensation from the Hand to the Chest Skin of Human Amputees with Targeted Reinnervation." *Proceedings of the National Academy of Sciences of the United States of America* 104 (50):20061–66. https://doi.org/10.1073/pnas.0706525104.

Lacour, Stéphanie P., Samia Benmerah, Edward Tarte, James FitzGerald, Jordi Serra, Stephen McMahon, James Fawcett, Oliver Graudejus, Zhe Yu, and Barclay Morrison Iii. 2010. "Flexible and Stretchable Micro-Electrodes for in Vitro and in Vivo Neural Interfaces." *Medical & Biological Engineering & Computing* 48 (10):945–54. https://doi.org/10.1007/s11517-010-0644-8.

Lacour, Stéphanie P, James J Fitzgerald, Natalia Lago, Edward Tarte, Stephen McMahon, and James Fawcett. 2009. "Long Micro-Channel Electrode Arrays: A Novel Type of Regenerative Peripheral Nerve Interface." *IEEE Transactions on Neural Systems and Rehabilitation Engineering: A Publication of the IEEE Engineering in Medicine and Biology Society* 17 (5):454–60. https://doi.org/10.1109/TNSRE.2009.2031241.

Lago, Natalia, Esther Udina, Anup Ramachandran, and Xavier Navarro. 2007. "Neurobiological Assessment of Regenerative Electrodes for Bidirectional Interfacing Injured Peripheral Nerves." *IEEE Transactions on Bio-Medical Engineering* 54 (6 Pt 1):1129–37. https://doi.org/10.1109/TBME.2007.891168.

Loi, Daniela, Caterina Carboni, Gianmarco Angius, Gian Nicola Angotzi, Massimo Barbaro, Luigi Raffo, Stanisa Raspopovic, and Xavier Navarro. 2011. "Peripheral Neural Activity Recording and Stimulation System." *IEEE Transactions on Biomedical Circuits and Systems* 5 (4):368–79.

Loucks, C., V. Johnson, P. Boissiere, G. Starr, and J. Steele. 1987. "Modeling and Control of the Stanford/JPL Hand." In *1987 IEEE International Conference on Robotics and Automation Proceedings*, 4:573–78. https://doi.org/10.1109/ROBOT.1987.1088031.

MacEwan, Matthew R., Erik R. Zellmer, Jesse J. Wheeler, Harold Burton, and Daniel W. Moran. 2016. "Regenerated Sciatic Nerve Axons Stimulated through a Chronically Implanted Macro-Sieve Electrode." *Frontiers in Neuroscience* 10. https://doi.org/10.3389/fnins.2016.00557.

Mannard, A., R. B. Stein, and D. Charles. 1974. "Regeneration Electrode Units: Implants for Recording from Single Peripheral Nerve Fibers in Freely Moving Animals." *Science (New York, N.Y.)* 183 (4124):547–49.

Marks, A F. 1969. "Bullfrog Nerve Regeneration into Porous Implants." *Anatom. Rec.* 163:226.

McQuarrie, I G. 1985. "Effect of Conditioning Lesion on Axonal Sprout Formation at Nodes of Ranvier." *The Journal of Comparative Neurology* 231 (2):239–49. https://doi.org/10.1002/cne.902310211.

Micera, Silvestro, and Xavier Navarro. 2009. "Bidirectional Interfaces with the Peripheral Nervous System." *International Reivew of Neurobiology* 86:23–38.

Micera, Silvestro, Xavier Navarro, Jacopo Carpaneto, Luca Citi, Oliver Tonet, Paolo Maria Rossini, Maria Chiara Carrozza, et al. 2008. "On the Use of Longitudinal Intrafascicular Peripheral Interfaces for the Control of Cybernetic Hand Prostheses in Amputees." *IEEE Transactions on Neural Systems and Rehabilitation Engineering* 16 (5):453–72.

Navarro, Xavier, Thilo B. Krueger, Natalia Lago, Silvestro Micera, Thomas Stieglitz, and Paolo Dario. 2005. "A Critical Review of Interfaces with the Peripheral Nervous System for the Control of Neuroprostheses and Hybrid Bionic Systems." *Journal of the Peripheral Nervous System* 10 (3):229–58. https://doi.org/10.1111/j.1085-9489.2005.10303.x.

Poppler, Louis H, Xueping Ee, Lauren Schellhardt, Gwendolyn M Hoben, Deng Pan, Daniel A. Hunter, Ying Yan, et al. 2016. "Axonal Growth Arrests After an Increased Accumulation of Schwann Cells Expressing Senescence Markers and Stromal Cells in Acellular Nerve Allografts." *Tissue Engineering: Part B* 22 (13–14):949–61.

Raspopovic, Stanisa, Marco Capogrosso, Francesco Maria Petrini, Marco Bonizzato, Jacopo Rigosa, Giovanni Di Pino, Jacopo Carpaneto, et al. 2014. "Restoring Natural Sensory Feedback in Real-Time Bidirectional Hand Prostheses." *Science Translational Medicine* 6 (222):222ra19-222ra19. https://doi.org/10.1126/scitranslmed.3006820.

Resnik, Linda, Shana L Klinger, and Katherine Etter. 2014. "The DEKA Arm: Its Features, Functionality, and Evolution during the Veterans Affairs Study to Optimize the DEKA Arm." *Prosthetics and Orthotics International* 38 (6):492–504. https://doi.org/10.1177/0309364613506913.

Saheb-Al-Zamani, Maryam, Ying Yan, Scott J. Farber, Daniel A. Hunter, Piyaraj Newton, Matthew D. Wood, Sheila A. Stewart, Philip J. Johnson, and Susan E. Mackinnon. 2013. "Limited Regeneration in Long Acellular Nerve Allografts Is Associated with Increased Schwann Cell Senescence." *Experimental Neurology*, no. 247 (September):165–77.

Sanders, F. K., and D. Whitteridge. 1946. "Conduction Velocity and Myelin Thickness in Regenerating Nerve Fibres." *The Journal of Physiology* 105 (2):152–74.

Srinivasan, Akhil, Mayank Tahilramani, John T Bentley, Russell K Gore, Daniel C Millard, Vivek J Mukhatyar, Anish Joseph, et al. 2015. "Microchannel-Based Regenerative Scaffold for Chronic Peripheral Nerve Interfacing in Amputees." *Biomaterials* 41 (February):151–65.

Stieglitz, T., X. Navarro, S. Calvet, C. Blau, and J.-U. Meyer. 1996. "Interfacing Regenerating Peripheral Nerves with a Micromachined Polyimide Sieve Electrode." In *Proceedings of the 18th Annual International Conference of the IEEE Engineering in Medicine and Biology Society, 1996. Bridging Disciplines for Biomedicine*, 1:365–66 vol.1. https://doi.org/10.1109/IEMBS.1996.656995.

Suzuki, T., N. Kotake, K. Mabuchi, and S. Takeuchi. 2006. "Flexible Regeneration-Type Nerve Electrode with Integrated Microfluidic Channels." In *2006 International Conference on Microtechnologies in Medicine and Biology*, 303–5. https://doi.org/10.1109/MMB.2006.251557.

Sweeney, J. D., K. Deng, E. Warman, and J. T. Mortimer. 1989. "Modeling of Electric Field Effects on the Excitability of Myelinated Motor Nerve." In *Engineering in Medicine and Biology Society, 1989. Images of the Twenty-First Century., Proceedings of the Annual International Conference of the IEEE Engineering In*, 1281–82 vol.4. https://doi.org/10.1109/IEMBS.1989.96194.

Veltink, P. H., J. A. van Alsté, and H. B. Boom. 1989. "Multielectrode Intrafascicular and Extraneural Stimulation." *Medical & Biological Engineering & Computing* 27 (1):19–24.

Veltink, P. H., J. A. van Alste, and H. B. K. Boom. 1988. "Influences of Stimulation Conditions on Recruitment of Myelinated Nerve Fibres: A Model Study." *IEEE Transactions on Biomedical Engineering* 35 (11):917–24. https://doi.org/10.1109/10.8671.

Vizoso, A. D., and J. Z. Young. 1948. "Internode Length and Fibre Diameter in Developing and Regenerating Nerves." *Journal of Anatomy* 82 (Pt 1-2):110–134.1.

Williams, J. C, J. A Hippensteel, J. Dilgen, W. Shain, and D. R Kipke. 2007. "Complex Impedance Spectroscopy for Monitoring Tissue Responses to Inserted Neural Implants." *Journal of Neural Engineering* 4:410.

Wood, Matthew D., Amy M. Moore, Daniel A. Hunter, Sami Tuffaha, Gregory H. Borschel, Susan E. Mackinnon, and Shelly E. Sakiyama-Elbert. 2009. "Affinity-Based Release of Glial-Derived Neurotrophic Factor from Fibrin Matrices Enhances Sciatic Nerve Regeneration." *Acta Biomaterialia* 5 (4):959–68. https://doi.org/10.1016/j.actbio.2008.11.008.

Yoshida, Ken, D Pellinen, D Pivin, Patrick J Rousche, and Daryl R Kipke. 2000. "Development of the Thin-Film Longitudinal Intra-Fascicular Electrode." *IFESS 2000. NP 2000, Proceedings, 5th Annual Conference of the International Functional Electrical Stimulation Society, 6th Triennial Conference "Neural Prostheses: Motor Systems", 18-24 June 2000, Aalborg, Denmark. Ed. / T. Sinkjær; D. Popovic; J. J. Struijk. Center for Sensory-Motor Interaction (SMI), Department of Health Science and Technology, Aalborg University*, 279–81.

Zellmer, Erik, Matthew MacEwan, and Daniel Moran. 2017. "Modelling the Impact of Altered Axonal Morphometry on the Response of Regenerative Nervous Tissue to Electrical Stimulation through Macro-Sieve Electrodes." *Journal of Neural Engineering*.

Ziegler-Graham, Kathryn, Ellen J. MacKenzie, Patti L. Ephraim, Thomas G. Travison, and Ron Brookmeyer. 2008. "Estimating the Prevalence of Limb Loss in the United States: 2005 to 2050." *Archives of Physical Medicine and Rehabilitation* 89 (3):422–29. https://doi.org/10.1016/j.apmr.2007.11.005.

Chapter 5: Electrostatic Model Validation

In the prior chapters, electrostatic models (implemented in Comsol) have been relied on to predict the electrical potential for various geometries of devices. As with any engineering model, it is sound practice to attempt verify the model. This chapter discusses efforts to do that. Two large scale channel models were built. The first had two adjacent channels with electrodes in each, while the second was a single channel with one end sealed and several electrodes at along its length. The Comsol models used in prior chapters were updated to match the increased size, specific channel locations, and use of saline instead of neural tissue. Each electrode was used as a stimulation source and the recorded results from every other electrode were compared with the Comsol model results. After correcting for electrode - electrolyte interface impedance, the results matched quite well.

5.1 Electrode - Electrolyte Impedance

In the Comsol model developed in the prior chapters, a controlled current source was used as is common in laboratory settings. However, in the clinical setting for which these devices are ultimately destined, the stimulation is frequently accomplished with a voltage source. The electrode-electrolyte interface has an impedance that is a function of both frequency and current density. During stimulation, this results in a voltage drop across that interface such that the voltage seen by the neural tissue is less than is applied at the electrode.

Often the electrode-electrolyte interface is modeled as parallel combination of a resistor and capacitor, sometimes also in series with a battery representing the half-cell potential of the electrode-electrolyte interface. However, the value of the resistor and capacitor are both

frequency-dependent (Geddes, 1972) which means this model is not useful for evaluating the frequency response of the system as would typically be done with a circuit model. Further, unless one is looking at the DC response, the half-cell potential can be ignored as well.

The dependence of the impedance on the amplitude of the current density is such that as the current density increases, a region is reached where there are dramatic increases in capacitance (Figure 5-1) and decreases in series resistance (Figure 5-2), resulting in an overall sharp decrease in impedance. The ultimate effect is that at high current densities, the impedance over frequency becomes relatively flat (Figure 5-3) (Geddes, 1972).

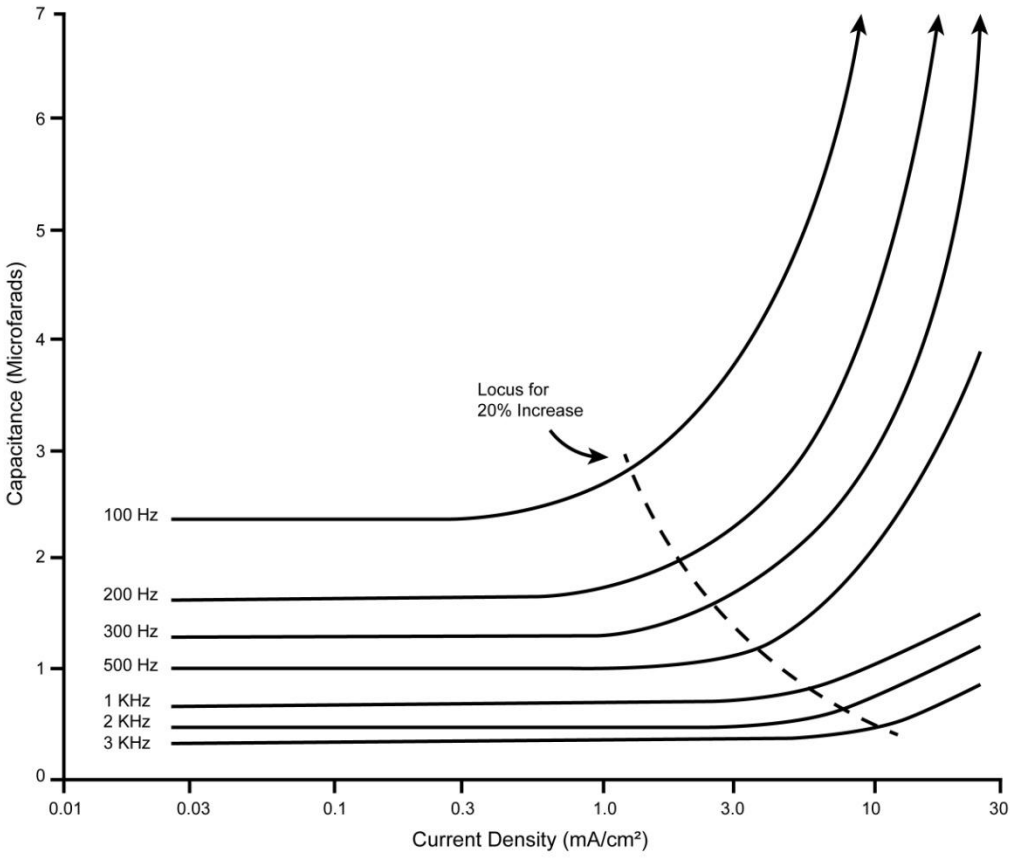

Figure 5-1. Capacitance as a function of current density for an electrode-electrolyte interface (data taken from Geddes, 1972). Notice the "knee" in the capacitance as current density increases.

This dependence on current density becomes significant if one tests the impedance of a working electrode at a low current density, but uses it operationally at a much higher current density. First, the impedance will be much lower than predicted, particularly at low frequencies (< 1 kHz). Second, because the effect is exaggerated at low frequencies, there will not be the expected reduction in impedance as stimulating frequency is increased (Figure 5-3).

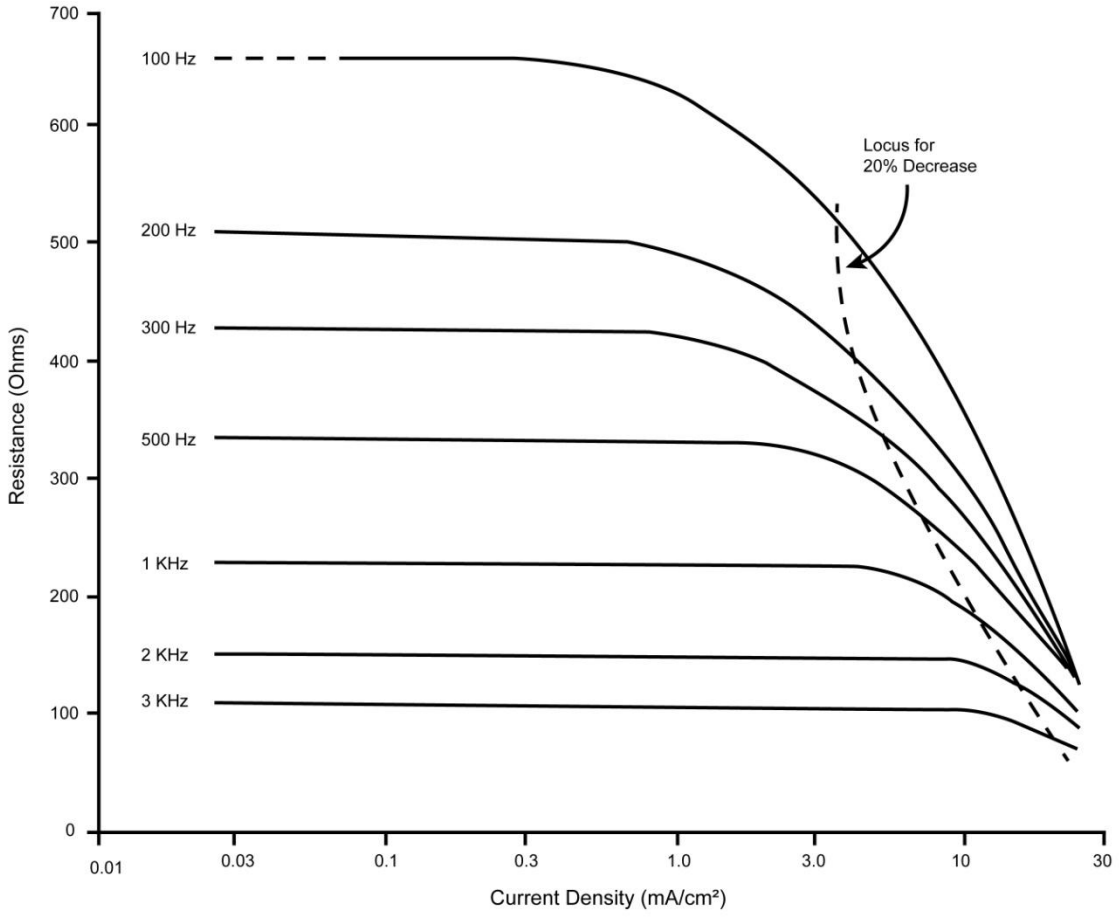

Figure 5-2. Equivalent Series Resistance (ESR) as a function of current density (data taken from Geddes, 1972). Notice the sharp rolloff as current density increases.

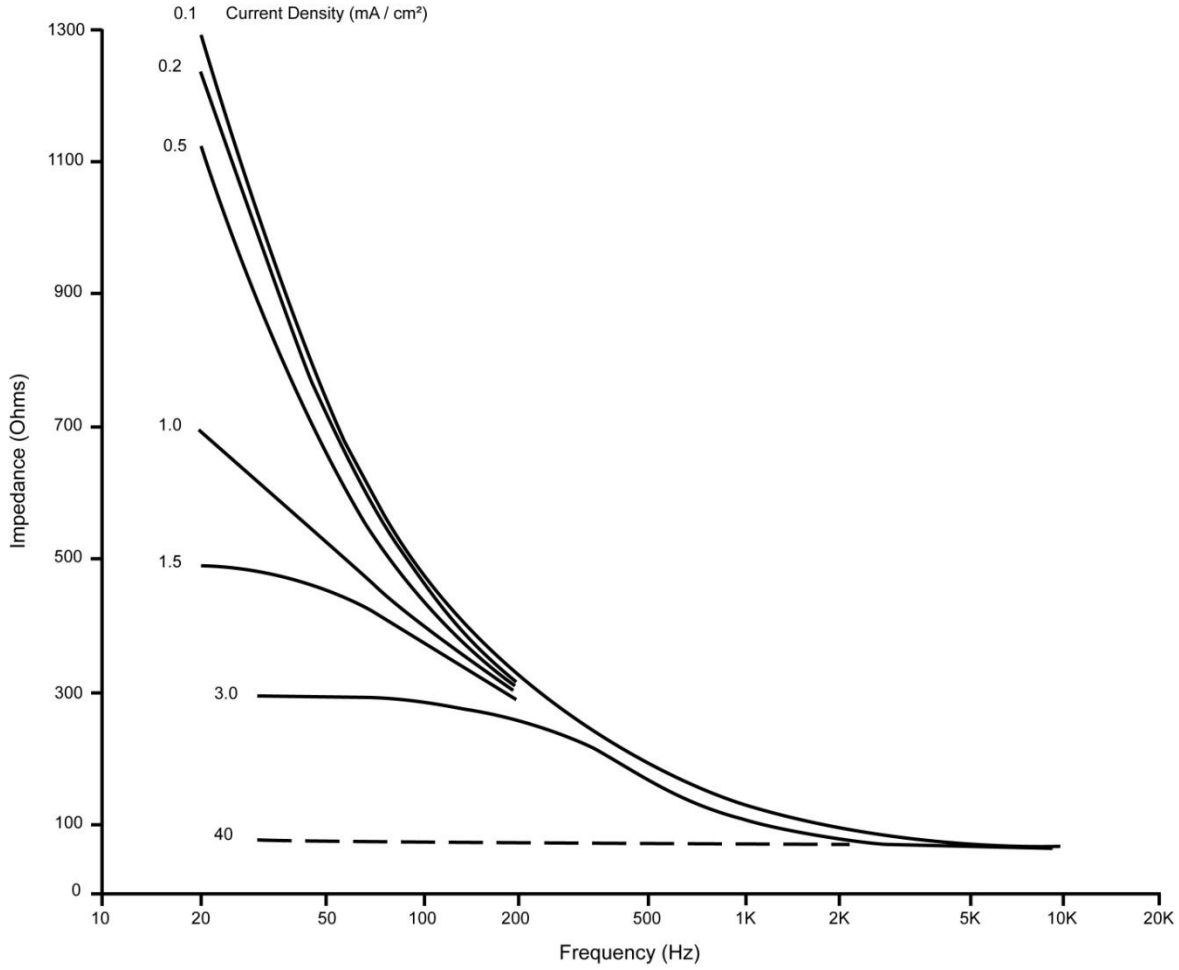

Figure 5-3. Impedance as a function of frequency at different current densities (data taken from Geddes, 1972). For high current densities, there is much less dependence on frequency.

5.2 Adjacent Channel Geometry

The first physical model used to test the Comsol model was very similar in overall structure to the micro-channel devices of earlier chapters. Two plastic tubes (6 cm long, 1/4" outer diameter, 1/8" inner diameter) were secured adjacent to each other on a glass slide. Holes were made in the tubing near each end of one channel and in three locations toward the middle of the other. Lengths of magnet wire (28 AWG, 0.32 mm diameter) had roughly 3 mm stripped from the end which was inserted in the holes. Silicone was used to hold the wire in place as well as electrically

seal current inside the channel. A small length of the other end was also stripped so that sound electrical contact could be made.

5.2.1 Comsol Model

The Comsol model of prior chapters was modified to match the physical geometry. Instead of using square channels, cylinders of the correct size were used as shown in Figure 5-4. Electrodes were placed to match the physical device. Instead of using the conductivity of peripheral neural tissue, an isotropic conductivity of 1.5 S/m was used - a typical value for 1x PBS. Each electrode in turn was set to 1V and the voltages along the center of both channels were computed.

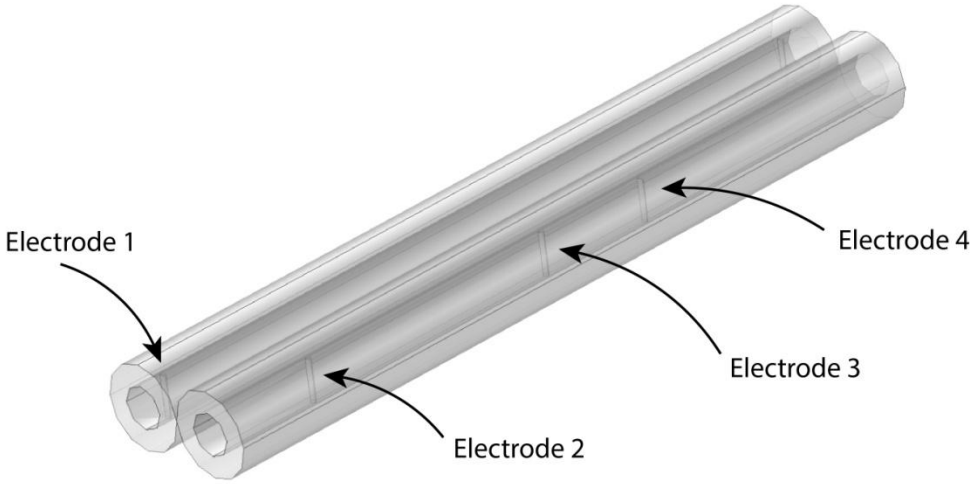

Figure 5-4. Comsol model of two adjacent channels

Table 5-1. Resistance from electrode to distant ground (2 channel model)

Electrode	Current (mA)	Resistance (Ohms)
1	3.22	311
2	1.12	893
3	0.653	1530
4	0.664	1510

Similar to prior modeling results in the micro-channels, stimulation within the channel results in large and far-reaching electrical potential until the edge of the channel is reached (Figure 5-5). As shown, stimulation in one channel has little effect on the neighboring channel. In addition to the 2D contour maps which provide a qualitative sense of the voltage distribution, the voltage axially along the center of the channels was exported. Finally, the current density from the surface of the electrodes was integrated within Comsol to determine the predicted impedance from the electrode to a distant, large ground (Table 5-1).

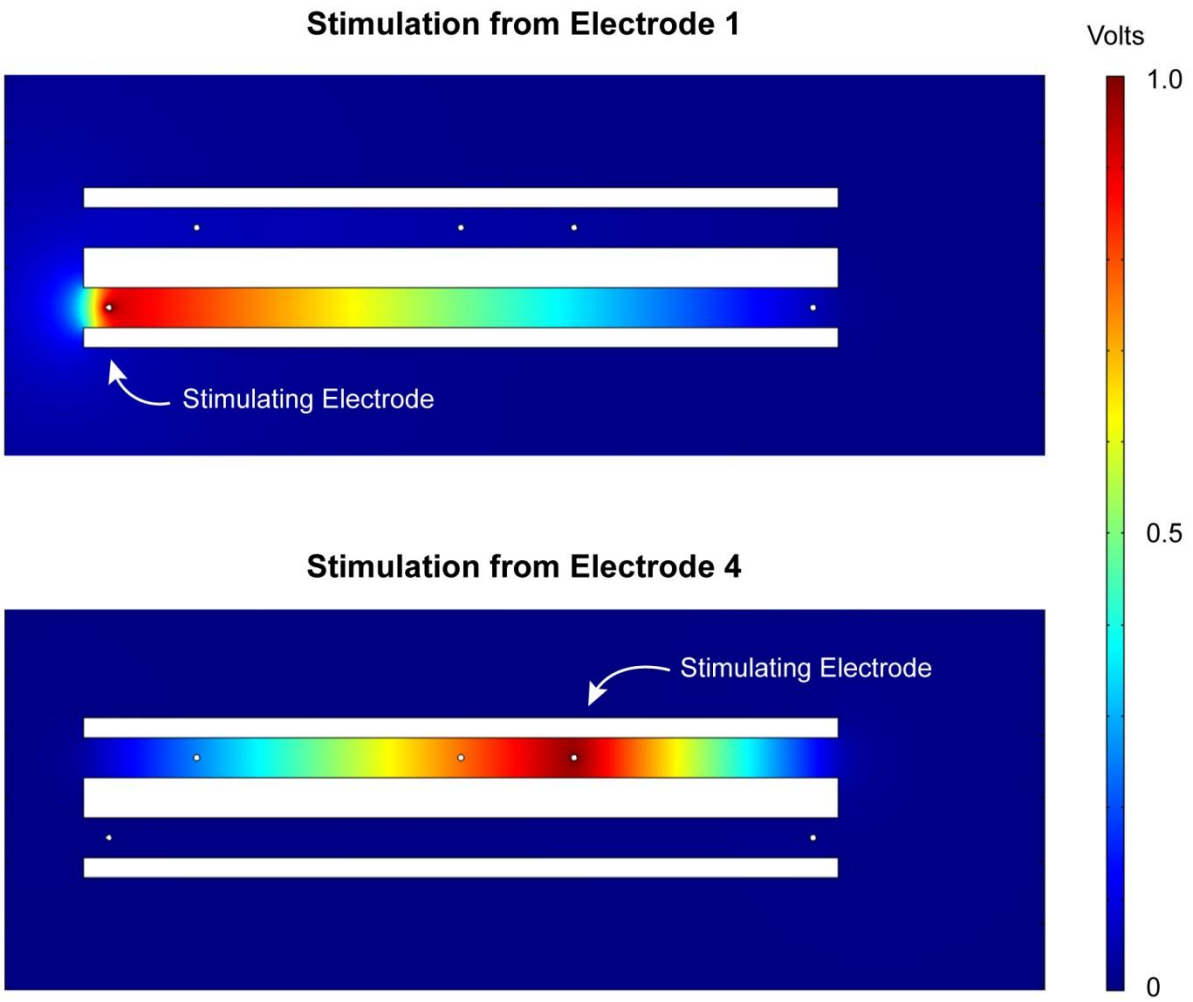

Figure 5-5. Electrical potential at the vertical center of the channels for stimulation at two different electrodes. White rectangular regions are the channel walls while the small white circles are the electrodes. The stimulation artifact in the adjacent channel is nearly imperceptible.

5.2.2 Measured Results

The impedance of each electrode was measured prior to other measurements (Metrohm Autolab, Model PGSTAT128N, The Netherlands). The impedance curves (Figure 5-6), measured with 25 mV applied to the working electrode are as expected, indicating no major construction issues or obstructed electrodes.

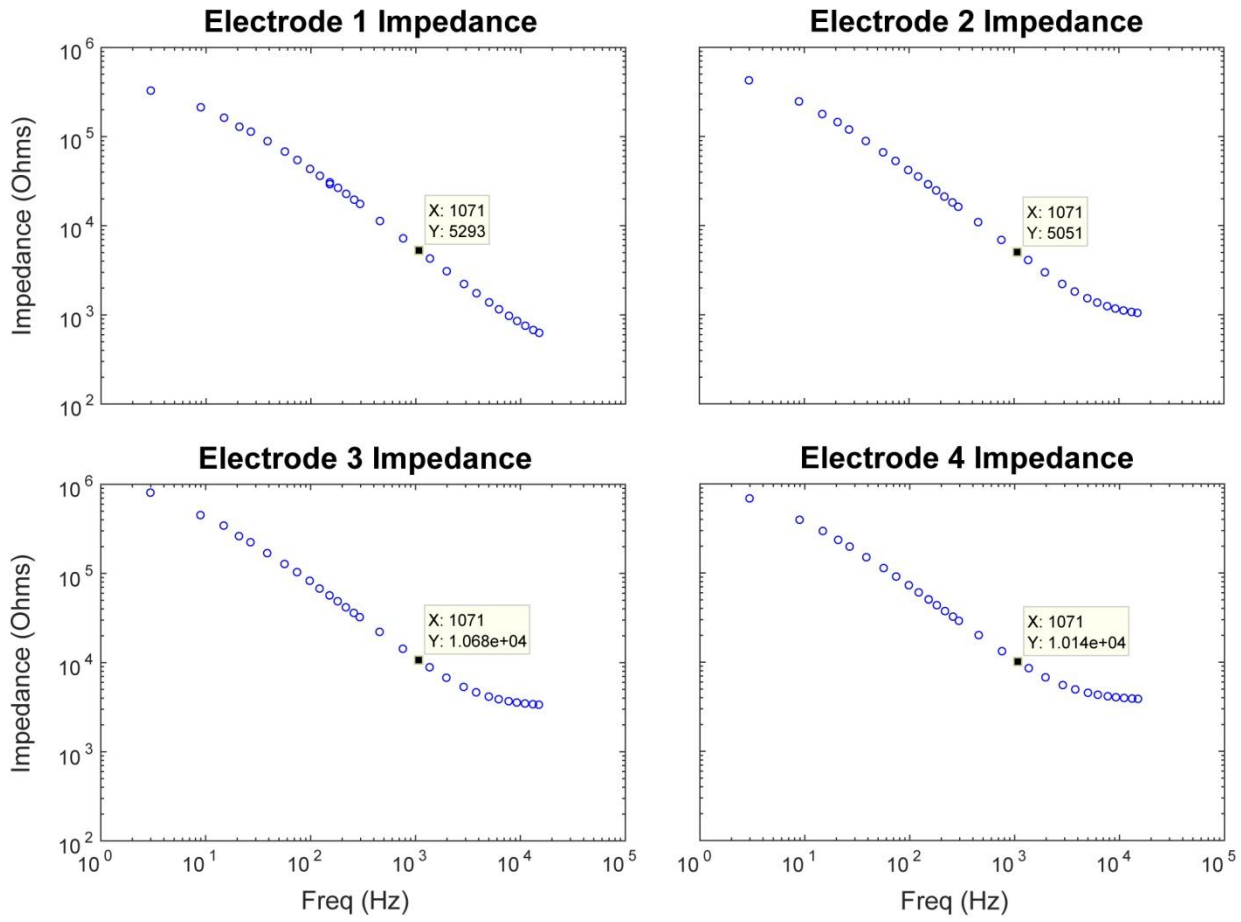

Figure 5-6. Impedance of electrodes in 2 channel model. Impedance at 1 kHz (1071 Hz) is shown.

At this amplitude of stimulation, there is a considerable difference in the impedance at 384 Hz compared to 1536 Hz, the low and high end of stimulations. Further, the electrode impedance is much larger than the impedance to ground through the saline (Table 5-1). To estimate the current density during the impedance measurement, the surface area of the electrode is approximately is roughly 3 mm^2 (or 0.03 cm^2) for a 3mm length of 28 AWG wire while the current would between 2.5 and 5 µA for a range of impedances of 5k - 10k Ohms. This results in a current density of 0.083 - 0.17 mA/cm^2. This is within the flat region of the capacitance and resistance curves of Figures 5-1 and 5-2.

After confirming via the impedance measurement that all electrodes were properly conducting, each electrode successively had a voltage source applied to it via an electrophysiology stimulation and recording system (RZ5, Tucker Davis Technologies, Alachua, FL). The frequency of the source voltage was increased in octaves from 48 Hz to 3072 Hz at a constant amplitude of 1V, a reasonable voltage given the modeled voltage in the micro-channels to induce neural stimulation. While one electrode was stimulated, the potential at the remaining electrodes was recorded by the front panel inputs after being buffered by a custom multi-channel amplifier (Gain = 5, 3 dB cutoff = 9500 Hz).

The data was high-pass filtered to remove interference from 60 Hz and the magnitude of the signals recorded at 384, 768 and 1536 Hz for each electrode was determined. Since the stimulation voltage was 40 times greater than when measuring the impedance, the current density would also be expected to be 40 times greater or 3.4 - 6.7 mA/cm^2. This, of course, neglects the non-linear effect that increasing the current density has in decreasing the electrode-electrolyte impedance which results in the current increase being super-linear. Regardless, the impedance curve as a function of frequency flattens considerably in this range (see Figure 5-3) with the result that there was only a modest difference in the voltage levels recorded at the 3 different frequencies and, thus, all three frequencies were averaged to create one potential level at each recording site for each stimulating site.

The electrode-electrolyte interface impedance causes a voltage drop across the interface which has to be accounted for to compare the predicted and measured results. For example, if the impedance of the path to ground from a given electrode was the same as the electrode-electrolyte impedance for that electrode, the Comsol generated curve would need to be multiplied by 1/2 since half the voltage would be dropped across the electrode-electrolyte interface. The

impedance of the recording electrodes can be ignored because the input impedance of the buffer amplifier is greater than 100 times the electrode impedance. Thus, no current and no associated voltage drop occurs across the recording interface. A least squares fit was used to determine the ratio by which Comsol curve should be multiplied to account for the voltage divider effect of the electrode-electrolyte interface with results shown in Table 5-2.

As the model predicted, stimulation in one channel results in only a very small signal in the adjacent channel. However, stimulation within a channel results in a large electrical potential throughout much of the channel as a result of the stimulation current being trapped within the channel (Figure 5-7). From the predicted voltage traces (blue), it can be observed that channel acts analogous to a linear taper electrical potentiometer with the two outside connectors grounded and a voltage applied to the wiper. For the channel, the resistance to ground at both ends is low. Further, the channel constrains ionic current flow to a single dimension in a homogenous material. As a result, the resistance of a section of channel is proportional to its length, i.e. a linear function of the length. This is why the channel has the same amount of voltage drop across either side of the stimulating electrode, why that drop is linear across the length of the channel until the channel edge, and the reason the slope of the potential depends on the distance from the stimulating electrode to the channel edge. The results match remarkably well when stimulation occurs within the same channel. The results in the adjacent channel are much smaller, as predicted, but do not seem to be as close to the predicted value. This is explained by two things. First, the actual error is quite small and looks large only because the adjacent channel expected values are so much smaller than the same channel values. Second, since the measurements are much smaller, any measurement error is a bigger fraction of the signal being measured. Regardless, the results are quite close.

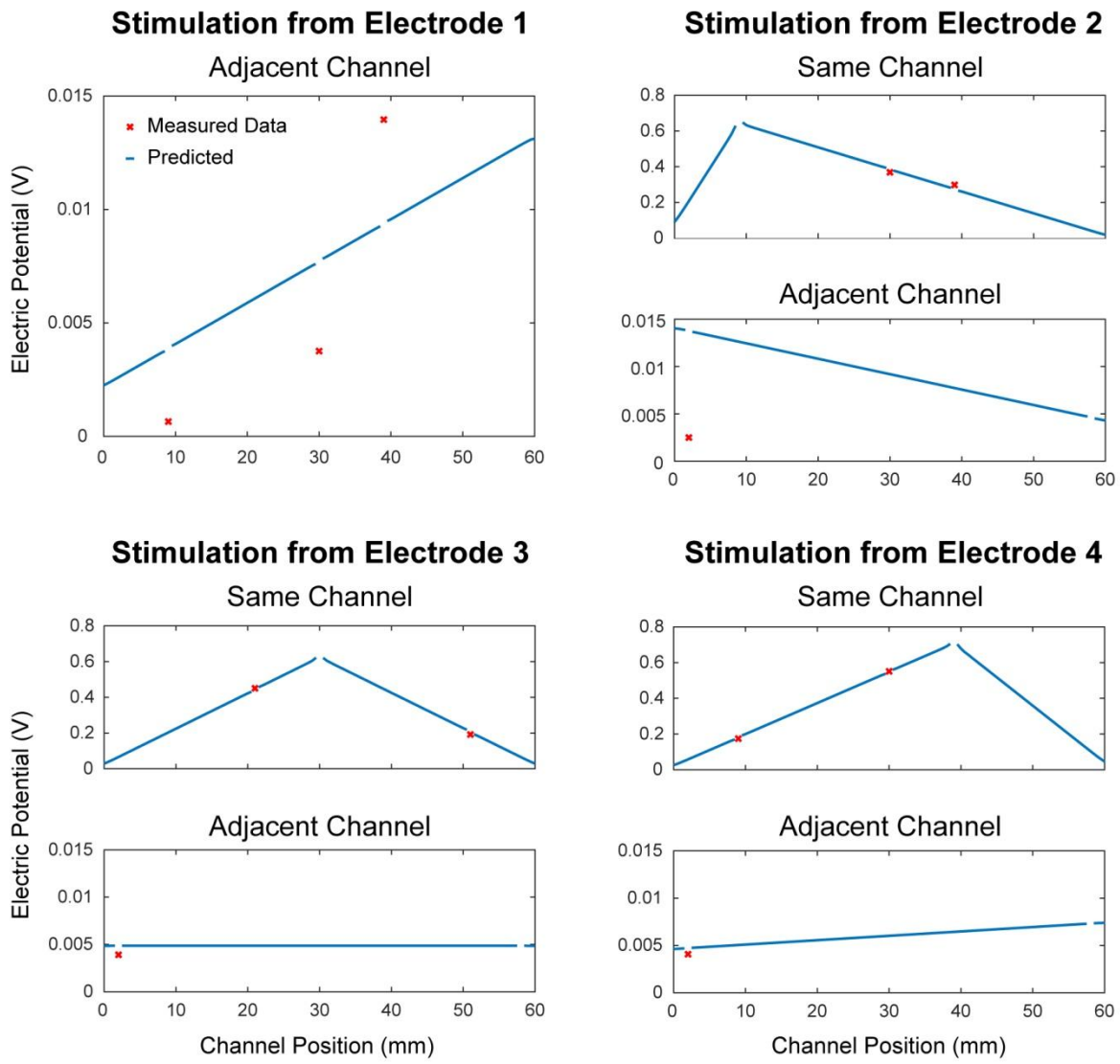

Figure 5-7. Two channel model - comparison of recorded voltage vs Comsol model after correcting for electrode-electrolyte voltage drop.

Table 5-2. Scale factor for stimulating electrodes (2 channel model)

Electrode	Scale Factor
1	0.209
2	0.660
3	0.632
4	0.717

5.3 Sealed End Geometry

The second physical model used to test the electrostatic model was a single channel with one end sealed. A single plastic tube (9 cm long, 1/4" outer diameter, 1/8" inner diameter) was secured to a glass slide and one end was sealed with silicone. Holes were made in the tubing at 4 locations between the center and the sealed end of the channel. As before, magnet wire was inserted in the holes and silicone was used to hold the wire in place and electrically seal the hole.

While the 2 channel physical device is a large-scale model of the micro-channel device, the second model should be viewed more as a control. Intuitively, there is only one path out of the channel and the open end will be nearly grounded. The voltage should drop linearly from the stimulating electrode to the open end of the channel, but should be relatively constant in the region between the stimulating electrode and the sealed end since there is no current flow to result in a voltage drop. This provides the opportunity to confirm that the approach of the 2 channel device can consistently be applied.

5.3.1 Comsol Model

The 2 Adjacent Channel Comsol model was reduced to a single 9 cm channel to match the physical geometry of the channel and electrode configuration. Further, instead of grounding the complete outer perimeter of the modeled area, a large distant plane was grounded to more accurately depict the physical model (Figure 5-8), though it made no discernible difference in the results. As seen in the previous section, an isotropic conductivity of 1.5 S/m was used. Each electrode in turn was set to 1V and the voltage along the center of the channel was computed.

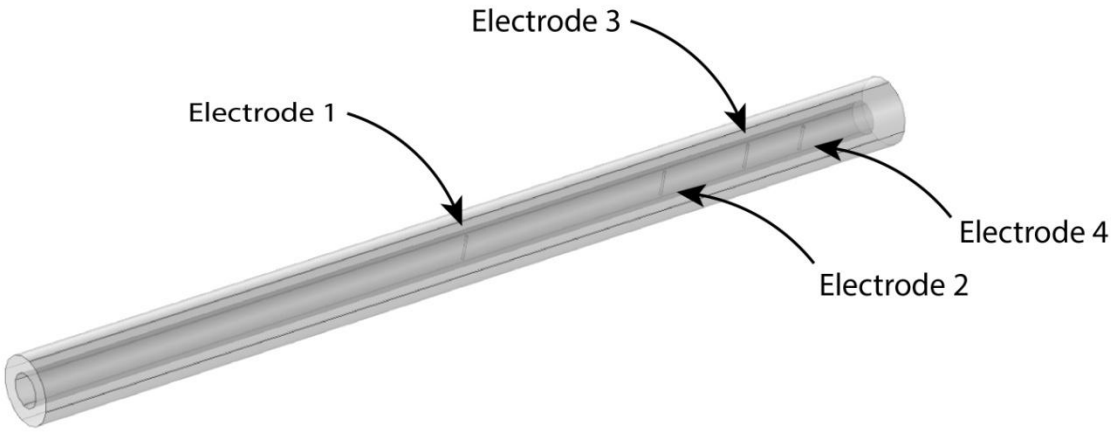

Figure 5-8. Comsol model of single channel with one end sealed

Table 5-3. Resistance from electrode to distant ground (single channel model)

Electrode	Current (mA)	Resistance (Ohms)
1	0.184	5450
2	0.127	7860
3	0.111	9050
4	0.109	9171

As before, the 2D contour map provides a qualitative sense of the voltage distribution (Figure 5-9), the voltage axially along the center of the channels was exported, and the impedance to ground was determined from integrating the current density from the surface of the electrodes (Table 5-3).

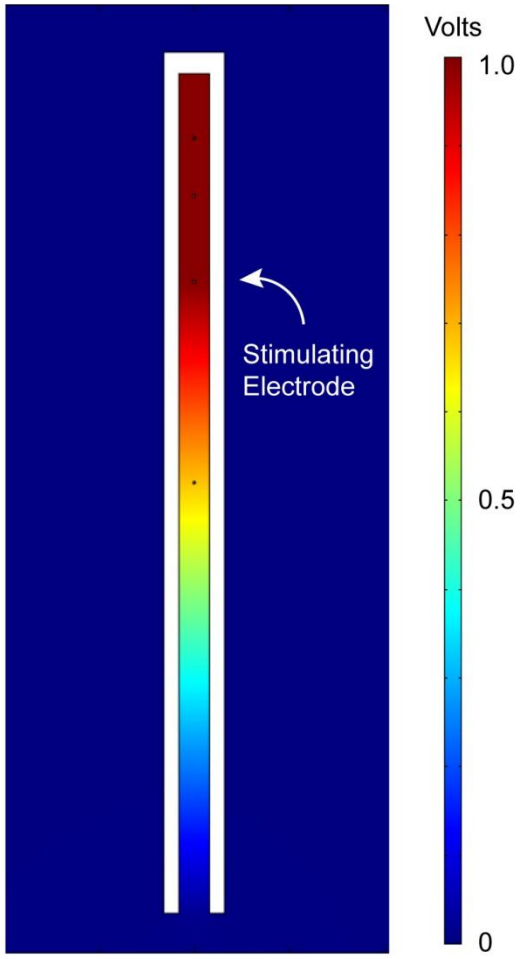

Figure 5-9. Electrical potential at the vertical center of the channel from stimulating at electrode 2

5.3.2 Measured Results

The impedance of each electrode was measured prior to other measurements as described in the 2 channel device. The impedance curves (Figure 5-10) indicated no major construction issues or obstructed electrodes. Even at lower current densities, the impedance is relatively constant across the ~400 - 3000 Hz range.

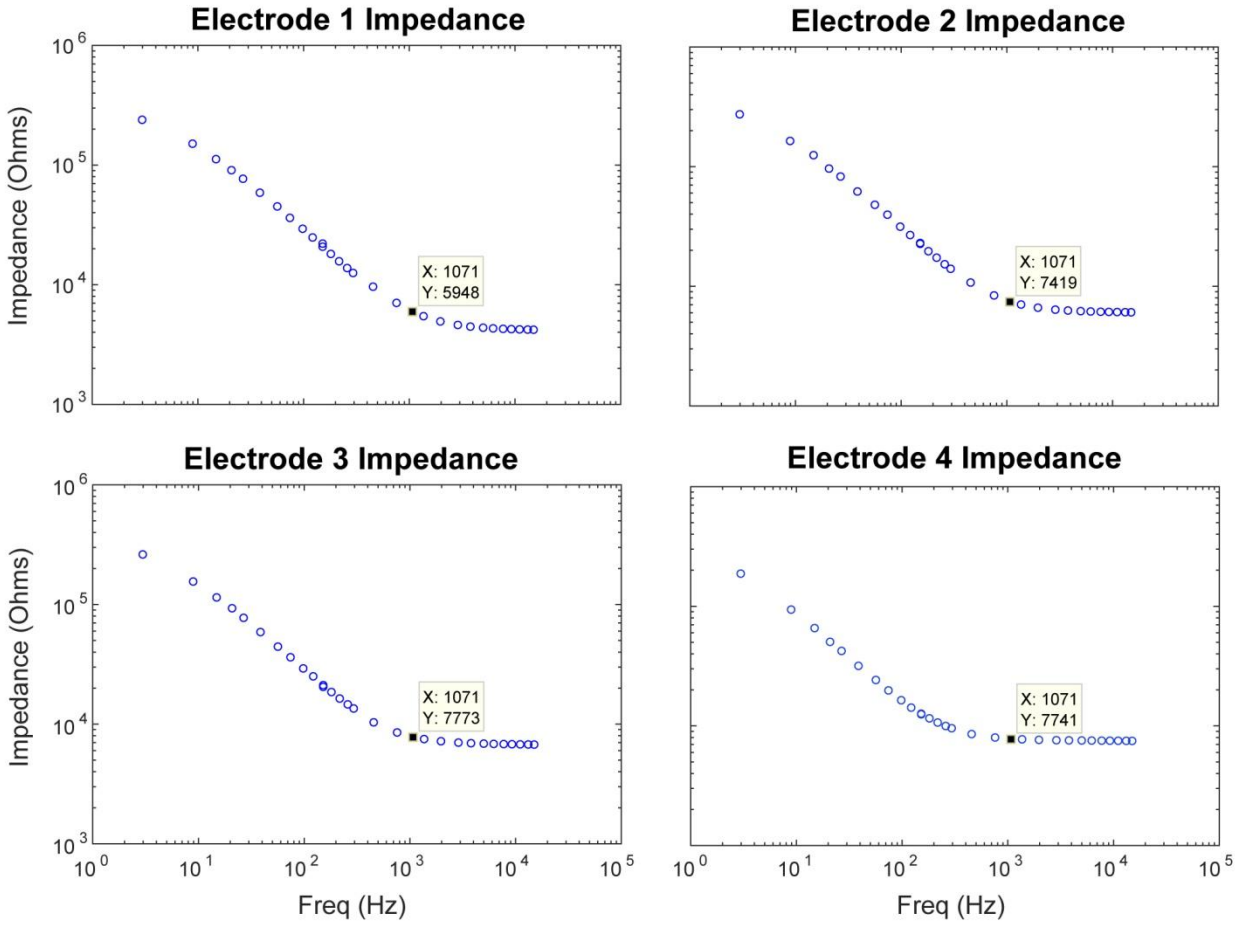

Figure 5-10. Impedance of electrodes in single channel model. Impedance at 1 kHz (1071 Hz) is shown.

The same stimulation pattern, recording technique, and data analysis was used as in the 2 channel device. The results (Figure 5-11, Table 6-4) show excellent correspondence to the Comsol model.

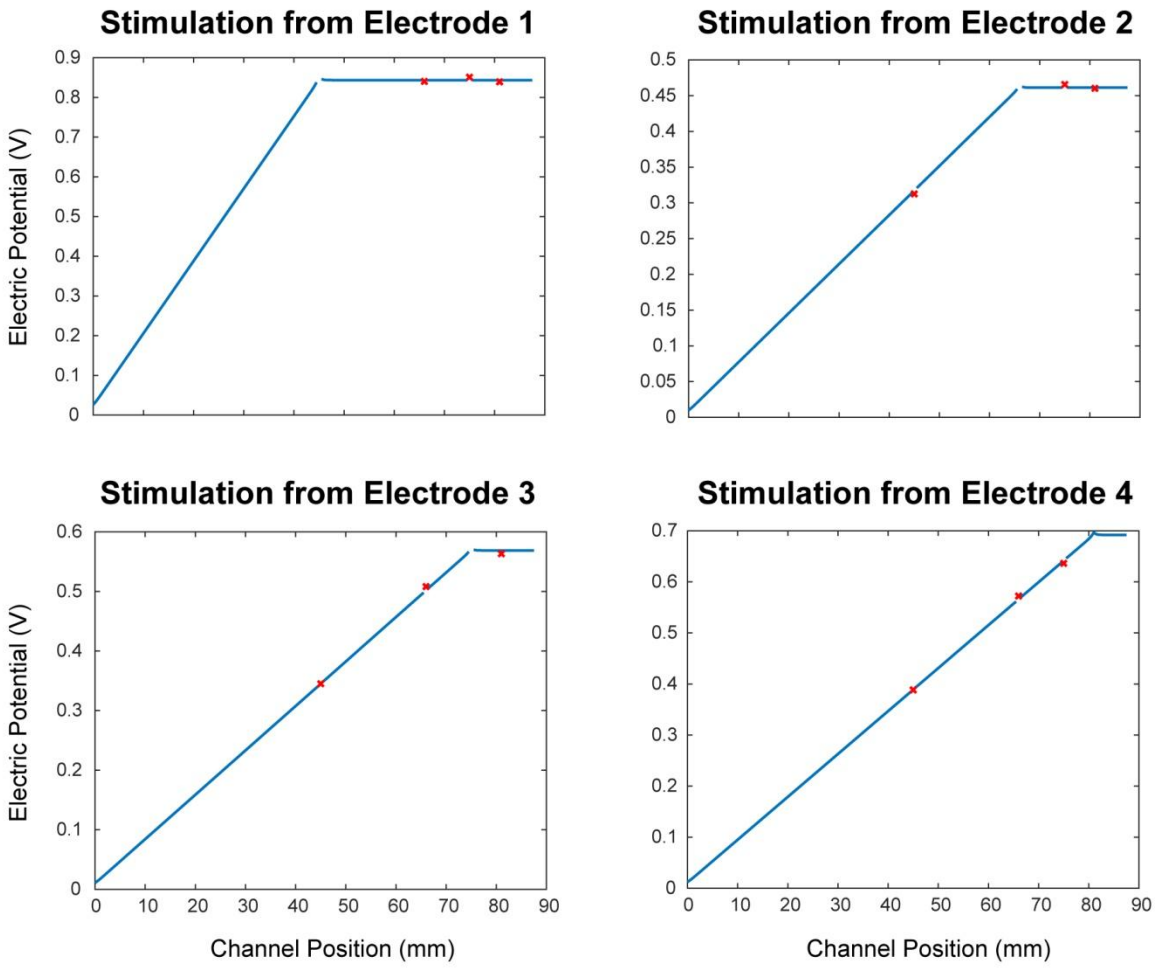

Figure 5-11. Single, closed-end channel model - comparison of recorded voltage vs Comsol model after correcting for electrode-electrolyte voltage drop.

Table 5-4. Scale factor for stimulating electrodes (2 channel model)

Electrode	Scale Factor
1	0.853
2	0.465
3	0.573
4	0.697

5.4 Results Summary

The goal of creating and measuring physical models was to confirm that the electrostatic modeling performed in Comsol accurately described the electrical characteristics of the devices. Two different geometries, one quite similar to the micro-channel model and the other a control, were used. After correcting for the voltage drop across the electrode-electrolyte interface which has the overall effect of multiplying the predicted voltage curves by a scale factor, measured results matched predicted values very closely. Further, the stimulating electrodes were found to have an impedance that was relatively constant across the frequency band of interest. In one case this was true even when measuring impedance at low signal levels. In both cases, the current density used to collect recordings was much greater than that used when measuring impedance which has been reported by Geddes to causing a decrease in the frequency dependence. This works confirms the Comsol model used in prior chapters.

5.5 References

Geddes LA, Electrodes and the Measurement of Bioelectric Events, New York: Wiley-Interscience, 1972.

Chapter 6: Conclusion and Future Work

To summarize the work that has been accomplished herein, Micro-channel Sieve Electrodes have been shown through computational modeling to outperform a prominent alternative Peripheral Neural Interface (PNI), the tfTIME, in both recording amplitude and stimulation artifact. In fact, the performance, particularly with multi-polar stimulation, is adequate that no special care needs to be taken in the electronics or signal processing chain for the micro-channel device type. The electrostatic modeling of the micro-channel device was verified experimentally in a large-scale model. The tfTIME electrostatic model should be non-controversial since it is approximately a conductor in free space in all directions except for one.

One could argue that the neural response to stimulation has not been validated, but that is not the case. The axonal models and overall computational modeling process used herein are the same used by Zellmer *et al.* with a macro sieve regenerative electrode to model stimulating efferent axons. The recruitment thresholds were shown to match measured data in a rat sciatic model (Zellmer *et al.* 2017). Thus, this aspect of the model already has significant validation.

Another concern not addressed herein is the biological feasibility of the device. This has been tested already by other research teams. Lacour *et al.* tested smaller hole sizes than typically used herein with the best regeneration occurring in 100 µm by 100 µm, 5mm long channels (Lacour *et al.* 2009). Srinivasan *et al.* also did a biological feasibility study with size ranges that went somewhat larger than Lacour and also had successful regeneration (Srinivasan *et al.* 2015). These studies specifically investigated regenerative success while several others used the devices for recording (Fitzgerald *et al.* 2012; Minev *et al.* 2012; Kim *et al.* 2015; Gore *et al.* 2015) for which regeneration is a prerequisite.

6.1 Future Work

Future research in micro-channel devices should proceed on a few different lines. One of these is testing the ability to create detectable and discriminable percepts as feedback to a prosthetic limb user. Animal behavioral models could be used to test the ability to detect neural stimulation in one or more channels of the device as well as the ability to differentiate between different channels being stimulated, different frequencies and/or different magnitudes of stimulation current. This form of testing could be comparative, *i.e*. the number of different stimulation paradigms an animal could discriminate for micro-channels compared to tfTIMEs or macro-sieves.

A second line of research relates to the ability to record motor intention. In this case, an animal performs a behavioral task, preferably requiring different levels of force to be exerted, while recording from the micro-channel device. Recorded data could be used to train and test a decoder. Of course, sophistication could be added to this by testing multiple muscles and recording EMG levels. This is analogous to the work of Badia *et al.* with the tfTIME device (Badia et al. 2016).

Finally, both recording and stimulation could be combined to confirm the simultaneous bi-directional capability of the device. This could be done simply by recording in a given channel and stimulating in another to confirm that the recording channel does not receive problematic stimulation artifact. However, the more desirable experiment is to show that both directions of communication can function at the same time (*i.e*. concurrently). The ideal goal would be to perform a behavioral experiment in which the animal has to control a cursor (or similar) and modulate the control based on sensory feedback. This, after all, is the goal the user of the prosthetic limb wants to be able to accomplish!

6.2 References

Badia, Jordi, Stanisa Raspopovic, Jacopo Carpaneto, Silvestro Micera, and Xavier Navarro. 2016. “Spatial and Functional Selectivity of Peripheral Nerve Signal Recording With the Transversal Intrafascicular Multichannel Electrode (TIME).” *IEEE Transactions on Neural Systems and Rehabilitation Engineering* 24 (1):20–27.

Fitzgerald, James J, Natalia Lago, Samia Benmerah, Jordi Serra, Christopher P Watling, Ruth E Cameron, Edward Tarte, Stéphanie P Lacour, Stephen McMahon, and James W Fawcett. 2012. “A Regenerative Microchannel Neural Interface for Recording from and Stimulating Peripheral Axons in Vivo.” *Journal of Neural Engineering* 9 (1).

Gore, Russell K, Yoonsu Choi, Ravi V Bellamkonda, and Arthur W English. 2015. “Functional Recordings from Awake, Behaving Rodents through a Microchannel Based Regenerative Neural Interface.” *Journal of Neural Engineering* 12 (1):016017.

Kim, Bongkyun, Alejandro Reyes, Bernardo Garza, and Yoonsu Choi. 2015. “A Microchannel Neural Interface with Embedded Microwires Targeting the Peripheral Nervous System.” *Microsystem Technologies* 21 (7):1551–57.

Lacour, Stephanie P., J.J. Fitzgerald, N. Lago, E. Tarte, S. McMahon, and J. Fawcett. 2009. “Long Micro-Channel Electrode Arrays: A Novel Type of Regenerative Peripheral Nerve Interface.” *IEEE Transactions on Neural Systems and Rehabilitation Engineering* 17 (5):454–60. https://doi.org/10.1109/TNSRE.2009.2031241.

Minev, Ivan R, Daniel J Chew, Evangelos Delivopoulos, James Fawcett, and Stéphanie P Lacour. 2012. “High Sensitivity Recording of Afferent Nerve Activity Using Ultra-Compliant Microchannel Electrodes: An Acute in Vivo Validation.” *Journal of Neural Engineering* 9 (2).

Srinivasan, Akhil, Mayank Tahilramani, John T Bentley, Russell K Gore, Daniel C Millard, Vivek J Mukhatyar, Anish Joseph, et al. 2015. “Microchannel-Based Regenerative Scaffold for Chronic Peripheral Nerve Interfacing in Amputees.” *Biomaterials* 41 (February):151–65.

Zellmer, Erik, Matthew MacEwan, and Daniel Moran. 2017. “Modelling the Impact of Altered Axonal Morphometry on the Response of Regenerative Nervous Tissue to Electrical Stimulation through Macro-Sieve Electrodes.” *Journal of Neural Engineering*.